

REVIEW

Topological phases in two-dimensional materials: a review

To cite this article: Yafei Ren *et al* 2016 *Rep. Prog. Phys.* **79** 066501

View the [article online](#) for updates and enhancements.

Related content

- [Quantum anomalous Hall effect in time-reversal-symmetry breaking topological insulators](#)
Cui-Zu Chang and Mingda Li
- [Quantum anomalous Hall effect in real materials](#)
Jiayong Zhang, Bao Zhao, Tong Zhou et al.
- [A theoretical review on electronic, magnetic and optical properties of silicene](#)
Suman Chowdhury and Debnarayan Jana

Recent citations

- [Asymmetric Modulation on Exchange Field in a Graphene-BiFeO₃ Heterostructure by External Magnetic Field](#)
Huading Song *et al*
- [Formation of a large gap quantum spin Hall phase in a 2D trigonal lattice with three p-orbitals](#)
Chong Li *et al*
- [Interaction-driven spin-orbit effects and Chern insulating phases in corundum-based 4 d and 5 d oxide honeycomb lattices](#)
Okan Köksal and Rossitza Pentcheva

Review

Topological phases in two-dimensional materials: a review

Yafei Ren^{1,2}, Zhenhua Qiao^{1,2} and Qian Niu³

¹ ICQD, Hefei National Laboratory for Physical Sciences at Microscale, and Synergetic Innovation Center of Quantum Information and Quantum Physics, University of Science and Technology of China, Hefei, Anhui 230026, People's Republic of China

² CAS Key Laboratory of Strongly-Coupled Quantum Matter Physics and Department of Physics, University of Science and Technology of China, Hefei, Anhui 230026, People's Republic of China

³ Department of Physics, The University of Texas at Austin, Austin, TX 78712, USA

E-mail: qiao@ustc.edu.cn and niu@physics.utexas.edu

Received 24 July 2015, revised 2 December 2015

Accepted for publication 2 February 2016

Published 13 May 2016



Invited by Mei-Yin Chou

Abstract

Topological phases with insulating bulk and gapless surface or edge modes have attracted intensive attention because of their fundamental physics implications and potential applications in dissipationless electronics and spintronics. In this review, we mainly focus on recent progress in the engineering of topologically nontrivial phases (such as \mathbb{Z}_2 topological insulators, quantum anomalous Hall effects, quantum valley Hall effects etc) in two-dimensional systems, including quantum wells, atomic crystal layers of elements from group III to group VII, and the transition metal compounds.

Keywords: topological phase, Hall effects, electron transport

(Some figures may appear in colour only in the online journal)

1. Introduction

Topological phases of condensed matter have attracted immense attention ever since the first proposal in the 1980s [1] to use this concept to explain the properties of the quantum Hall effect in two-dimensional (2D) electronic systems under a strong external magnetic field [2]. The quantum Hall effect is manifested by a vanishing longitudinal conductance but nonzero quantized Hall conductance in a six-terminal Hall-bar measurement [2, 3]. The vanishing longitudinal conductance originates from the insulating bulk while the quantized Hall conductance arises intrinsically from the Berry curvatures of the filled magnetic Bloch bands, as reported by Thouless *et al* [1]. The Berry-curvature integration over the filled bands in the magnetic Brillouin-zone gives rise to an integer named as Thouless–Kohmoto–Nightingale–Nijs (TKNN) number.

Later, this expression was recognized as the first Chern class of a $U(1)$ principal fiber bundle on a torus, where the fibers and torus correspond respectively to the magnetic Bloch waves and the magnetic Brillouin zone [4, 5]. Therefore, the TKNN number is also known as the Chern number, which is a topological invariant in the sense that the integer will not change as long as the bulk band gap, wherein the Fermi level lies, is not closed by the external perturbations [6]. The Chern number is closely related to the amplitude of the quantized Hall conductance in units of e^2/h , reflecting the topological nature of quantum Hall effect, i.e. the Hall conductance is quantized as an integer as long as the bulk band gap remains open.

For an experimental sample with a finite size, the topology of the filled bands is reflected by the one-dimensional (1D) gapless chiral edge states according to the principle of the *bulk-edge* correspondence, where the Chern number counts

the number of edge states localized at each boundary between the quantum Hall effect and the vacuum [7]. Due to the topological protection of the one-way propagating characteristic at each boundary, the edge modes are robust against weak disorders in any form. The high-precision of the quantized Hall resistance plateau has let the quantum Hall effect become a new method to determine the fine structure constant, a fundamental physical constant [3]. Moreover, the robustness feature together with the vanishing longitudinal resistance has attractive practical potential in design of dissipationless or low-power electronic devices.

However, to realize the quantum Hall effect, the most crucial requirement is to apply a strong magnetic field. Unfortunately, it is beyond the current state of technology to generate such a huge magnetic field outside the laboratory. Therefore, the question naturally arises: is it possible to achieve the quantum Hall effect in the absence of a strong magnetic field? It is known that the necessary condition to induce a Hall effect is to break the time-reversal invariance, which can be achieved by either an external magnetic field or the intrinsic ferromagnetism [8]. The former results in the ordinary Hall effect, while the latter produces the anomalous Hall effect. Both effects actually exhibit the same transport characteristics. In the 2D limit, the strong magnetic field can lead to Landau-level quantization, hence the quantum Hall effect [2, 3]. Therefore, the anomalous Hall effect is also expected to become quantized in 2D systems with ferromagnetism by some means. Hereinbelow, we refer to the quantum Hall effect in the absence of the external magnetic field as the quantum *anomalous* Hall effect (QAHE). In 1988, Haldane [9] theoretically achieved this expectation by an exquisite toy model in a 2D honeycomb-lattice system by considering alternating magnetic fields with zero net flux. However, since the host material of the 2D honeycomb-lattice was believed to be unrealistic up until 2004 and the experimental realization of alternative magnetic fluxes is also extremely difficult, the further progress towards the realization of the QAHE was seriously hampered. Only two alternative proposals in Kagomé lattice and disordered 2D ferromagnetic metals were reported [10, 11]. Nevertheless, such a theoretical proposal not only raised the hope of achieving QAHE for dissipationless applications, but also immediately inspired great interest when the era of 2D materials finally comes.

On the other hand, during that period investigations of the dynamics of the magnetic Bloch electrons within the partially occupied magnetic Bloch bands revealed the underlying importance of the Berry curvature in the dynamical processes [12, 13]. The further generalization to ordinary Bloch electrons in crystals without a strong magnetic field opened up new grounds in the study of the topological properties of 2D electron gases [14]. Especially, this inspired a revisit to the old issues of the anomalous Hall effect including the spin-Hall effect [8]. Apart from the fundamental interest of the anomalous/spin-Hall effect, potential applications in spintronics to generate dissipationless spin current further stimulated research, which led to the discovery of the topological contribution to the spin-Hall effect [15–19]. However, it is shown that the longitudinal charge current in the spin-Hall effect is nonzero

hence dissipative. To overcome this difficulty, a spin-Hall insulator was proposed by Murakami *et al* in 2004, wherein a finite spin-Hall conductance is expected in the bulk insulating/zero-gap materials [20]. These pioneering works established a solid foundation for future research on topological phases.

The era of 2D materials started from the year of 2004, when graphene, a single layer of carbon atoms arranged in a honeycomb-lattice structure, was first successfully exfoliated [21]. Its unique mechanical, electrical, and optical properties and its special linear-Dirac dispersion soon attracted great interest from various research fields, making it a *star* material [22]. However, its half-filled conduction bands with gapless Dirac dispersion limits its applications of graphene in semiconductor-based electronics. Different binary degrees of freedom (i.e. real spin, AB sublattices, KK' valleys, and top/bottom layers) have been adopted to engineer bulk band gaps that are able to harbour various topological phases. In particular, graphene provides a real 2D honeycomb-lattice platform to revive Haldane's proposal of the QAHE.

Soon after the experimental discovery of graphene, Kane and Mele pointed out that the intrinsic spin-orbit coupling from the next-nearest neighbor hopping plays the corresponding role of the alternative magnetic flux in Haldane's model [9, 23], which can open up a bulk band gap at the Dirac points to harbour two copies of QAHE that are respectively encoded with opposite spins and chiralities [23]. That is, opposite Chern numbers are present for spin-up and spin-down electrons, respectively. The resulting spin-helical gapless edge states counter-propagate along the same boundary with opposite spins, which results in a vanishing charge Hall conductance yet quantized spin-Hall conductance. This phase was therefore called the quantum spin Hall effect (QSHE) [23], and it is preserved even when the spin is no longer a good quantum number, indicating its topological nature that is characterized by the \mathbb{Z}_2 topological order [24]. The Karmers-degenerate spin-helical edge states are robust against weak disorders due to the topological protection from time-reversal symmetry. This insulating phase is therefore also called a topological insulator (TI), to embrace a broader connotation in addition to the QSHE [24]. Although the Kane-Mele model was theoretically shown to host a 2D \mathbb{Z}_2 TI phase, the extremely weak intrinsic spin-orbit coupling makes the TI unrealistic in pristine graphene by employing the current experimental techniques [25–29]. Yet, much effort has been put in enhancing the intrinsic-type spin-orbit coupling in graphene via some external means (e.g. by adsorbing 5d heavy atoms) [30] and in searching for new graphene-like materials (e.g. low-buckled honeycomb-lattice materials) that possess strong intrinsic spin-orbit coupling [31, 32].

Almost parallel to the proposal of Kane and Mele, Bernevig *et al* suggested another route, i.e. band inversion by spin-orbit coupling, to realize QSHE in strained zinc-blende semiconductors [33] and HgTe quantum wells [34]. In 2007, one year after these theoretical proposals, QSHE was indeed experimentally observed in inverted HgTe quantum wells [35]. These pioneering studies laid the foundations for the field of the \mathbb{Z}_2 TI, which was subsequently extended to three-dimensional (3D) materials [36–39].

Both the theoretical and experimental advances of 2D and 3D TIs have also inspired the exploration of the QAHE by breaking time-reversal symmetry. In 2010, it was theoretically predicted that the QAHE can be achieved after a band inversion that originates from the ferromagnetism in the 3D TI thin films [40]. Following this theoretical recipe, in 2013 after three years of continuous effort, the QAHE was finally experimentally observed in Cr-doped $(\text{Bi}, \text{Sb})_2\text{Te}_3$ thin films [41]. Since then, there have been several follow-up observations of the QAHE in the same host materials of $(\text{Bi}, \text{Sb})_2\text{Te}_3$ doped with Cr [42, 43] or V [44] atoms. However, all the experimental observations were achieved at extremely low temperatures (i.e. 30–100 mK). Therefore, how to raise the temperature of the QAHE is a critical challenge for the communities of both condensed matter physics and materials science, from both the theoretical and experimental sides.

Engineering band gaps at the Dirac points of graphene is another rewarding route to realize the QAHE, which, in general, requires both spin-orbit coupling and intrinsic ferromagnetism [40]. Although the intrinsic spin-orbit coupling in graphene is extremely weak, there exists another extrinsically tunable spin-orbit coupling, i.e. Rashba spin-orbit coupling [45], which arises from the mirror-symmetry breaking about the graphene plane, e.g. by applying a perpendicular electric field [46]. In 2010, it was proposed that the QAHE can occur in graphene by simultaneously considering the Rashba spin-orbit coupling and out-of-plane exchange field (or Zeeman field), which can be introduced via the proximity effect through doping magnetic atoms or utilizing ferromagnetic insulating substrates [47–49]. Although the QAHE has not been experimentally realized in graphene yet, there has already been striking progress towards the ultimate realization of the QAHE. Recently, a sizable anomalous Hall conductance of $\sigma_{xy} \approx 0.2e^2/h$ has been experimentally observed in graphene proximity-coupled with a magnetic thin film YIG [50]. To expedite the definitive observation of QAHE in graphene, a crucial issue is to enlarge the Rashba spin-orbit coupling that is strongly dependent on the strength of the van der Waals interaction between the graphene sheet and the magnetic substrate.

In graphene, the binary KK' valley degree of freedom can also be adopted to design topological *valleytronics* similar to spintronics by leveraging the valley-pseudospin in the manner of electron spin [51]. The analogy between valley-pseudospin and electron spin also inspired the prediction of the quantum valley-Hall effect (QVHE), for which the K and K' valleys carry nonzero Chern numbers but with opposite signs [52]. Therefore, this phase is well-defined only when KK' valleys are decoupled in the absence of short-range scattering. This new phase can be realized by breaking the inversion symmetry, e.g. introducing the staggered AB sublattice potentials in monolayer graphene or applying a perpendicular electric field in the Bernal-stacked multilayer graphene [52–54]. It is noteworthy that, different from the QSHE, the bulk-edge correspondence is absent in monolayer graphene but present in multilayer graphene.

Interestingly, when the QVHE coexists with the QAHE or TI, the resulting edge modes can even be robust against weak short-range scattering since the QVHE originates from

the inversion symmetry breaking that is compatible with the preservation or breaking of the time-reversal invariance. In addition to the edge states, gapless interface modes can also be generated along the interface between two QVHEs with opposite valley topologies (except for the exact armchair case that exhibits an unavoidable band gap). These interface states are also known as topological confinement states, kink states, zero modes, or zero-line modes (ZLMs) in the literature. In order to manifest the formation along the line of zero electric field, for clarity, we shall refer to this as ZLMs. This kind of ZLMs have been shown to exist naturally at the interfaces between different topological phases [55].

In addition to those topological phases mentioned above, the topological-phase family also includes the Floquet topological insulator driven by the time-dependent periodic potential with gapless edge states in the quasi-energy spectrum [56, 57], and the topological crystalline insulators that are topologically protected by mirror-reflection symmetry [58–60]. Apart from these topological phases in non-interacting systems where spin-orbit couplings play essential roles, the topologically nontrivial phases are also predicted in systems with strong correlations. Although the theoretically predicted topological Mott insulator [61] of half-filling honeycomb lattice is later proved to be unlikely [62, 63], the strong Coulomb-interaction driven topologically nontrivial phases have been widely investigated in Kondo insulators [64, 65], Kagomé-lattice systems [10], and bilayer graphene [66–69]. Moreover, in fractionally-filled flat bands of some lattices, the strong electron-electron interaction could also induce fractional topological nontrivial phases in the absence of magnetic field [70–74]. When the strong interaction is invoked, these 2D systems are difficult to study in an analytical manner. However, the artificial lattice composed of weakly coupled one-dimensional wires [75–77], which can be treated as 1D Luttinger liquid by bosonization [75, 76], provides an alternative platform to investigate various integer and fractional topological phases, e.g. QHE [75–79], QAHE [80], TI [81, 82], and topological superconductor [83]. Although these works are interesting, they are beyond the scope of the present review since we focus on the non-interacting particles in 2D systems without time dependent potentials.

There are several excellent reviews related to the topics mentioned above, such as the anomalous Hall effect [8, 84], the Berry-phase effect [85], 2D/3D TIs [36–38, 86, 87], and topological crystalline insulator [60]. In this review, we shall focus on the recent theoretical progress in studies of the 2D topological phases (including \mathbb{Z}_2 TI, QAHE and QVHE) of the noninteracting particles in atomic crystal layers and quasi-2D quantum wells in the absence of strong magnetic field. In section 2, we review the recent work on TIs built from atomic layers of the group-IV and -V elements, and quasi-2D quantum wells. In section 3, the QAHE is reviewed, beginning with its theoretical prediction and experimental realization in magnetic TIs, followed by the honeycomb-lattice based QAHE. In section 4, we review the QVHE in graphene and related systems. The electronic structure and transport properties of ZLMs at the interfaces between two QVHE with different Chern numbers at each valley are also described.

In section 5 we give a short discussion and summary. One should note that the discussions in below refer to the theoretical progresses unless otherwise noted.

2. 2D topological insulators (TIs)

To realize the 2D \mathbb{Z}_2 TI, two typical proposals are raised independently. One, Kane–Mele model in graphene, was to open a bulk band gap at the two inequivalent Dirac points [23] as a generalization of Haldane’s model to spinful system with time reversal symmetry [9]. The other was the Bernevig–Hughes–Zhang (BHZ) proposal to induce a band inversion in a 2D semiconductor [34]. These two models not only pioneer the investigation of TIs, but also represent two general routes for realizing 2D TIs, i.e. by opening up a band gap in the 2D Dirac semi-metals or by inducing a band inversion in narrow-gap semiconductors.

In the following, we briefly describe the basic physical origins of these two models and survey recent theoretical suggestions of possible materials that would have large topologically nontrivial band gaps and would be experimentally feasible with potential practical applications. In sections 2.1 and 2.2, the basic physics of the Kane–Mele model is reviewed, and then extended to the atomic-crystal layers of group-IV elements and organic honeycomb-lattice structures. The band inversion in the BHZ model is introduced in section 2.3. Based on these two basic formations, the theoretical proposals to create TIs within various 2D materials, such as graphene, atomic crystal layers of group-V elements, group III–V and IV–VI compounds, and transition metal dichalcogenides are reviewed in sections 2.4–2.7. The topological Anderson insulator as well as the time-reversal symmetry breaking QSHE are discussed in sections 2.8 and 2.9. All the possible systems to realize 2D TI are listed in table 1.

2.1. The honeycomb lattice and the Haldane model

As mentioned above, the single layer honeycomb-lattice structure plays an important role in both 2D TI and QAHE systems [9, 23, 24, 46]. Let us first briefly describe the π -band electronic structure of a spinless particle in the planar honeycomb lattice as displayed in figure 1(a), where two sets of inequivalent triangular lattices are present, namely the AB sublattices labelled by the empty and solid circles, respectively. Sublattice symmetry, also known as chiral symmetry, occurs when the nearest neighbor hopping t_1 between these two sublattices is present [89]. Therefore, only the off-diagonal terms that couple the AB sublattices are nonzero in the tight-binding momentum-space Hamiltonian [22]. When the coupling between the sublattices A and B vanishes, accidental degeneracy occurs with doubly degenerate zero-energy eigenstates that appear at the K and K' points, as shown in figure 1(b), where linear Dirac dispersions appear [90]. In the long wavelength limit, the low-energy continuum model Hamiltonian of the Dirac dispersions can be expressed as

$$H(\mathbf{k}) = v(\tau_z k_x \sigma_x + k_y \sigma_y), \quad (1)$$

where $v = 3t_1/2$ is the Fermi-velocity, and σ and τ are the Pauli matrices for the sublattice and valley pseudospins, respectively. For a single valley, the effective Hamiltonian can be written as $H(\mathbf{k}) = \sum_i d_i \sigma_i$ ($i = x, y, z$) with $\mathbf{d} = (d_x, d_y, d_z)$ being the pseudospin texture. The chiral symmetry guarantees the vanishing of d_z hence the pseudospin texture is in-plane as displayed in figure 1(c). Such a gapless linear dispersion can only become gapped by introducing a diagonal mass term, which breaks the sublattice symmetry.

The simplest way to break the sublattice symmetry is to consider a staggered sublattice potential $M\sigma_z$ that is momentum independent and opens bulk band gaps at K and K' points, as can be seen in figure 1(d). The out-of-plane pseudospin textures near the gapped points, i.e. nonvanishing $d_z = M$, leads to two merons (see the inset of figure 1(d)), which carry half Chern numbers [38, 91–93] that can be calculated by

$$\mathcal{C} = -\frac{1}{8\pi^2} \int d^2k \hat{\mathbf{d}} \cdot \partial_{\mathbf{k}} \hat{\mathbf{d}} \times \partial_{\mathbf{k}} \hat{\mathbf{d}}. \quad (2)$$

These two merons carry opposite topological charges, i.e. $\mathcal{C}_K = -\mathcal{C}_{K'} = 0.5 \operatorname{sgn}(M)$, since these two valleys are related to each other by the time-reversal symmetry, which guarantees the vanishing total Chern number. Alternatively, the Chern number carried by different valleys can also be obtained by integrating the Berry curvatures in the momentum space around the two Dirac points with a more generalized definition:

$$\mathcal{C} = \frac{1}{2\pi} \sum_n \int d^2k \Omega_n(\mathbf{k}), \quad (3)$$

where Ω_n is the z -component Berry curvature of the n -th occupied band. As a counterpart of the magnetic field in real space, the Berry curvature in momentum space is defined as $\Omega_n = (\nabla \times \mathbf{A}_n)_z$, where the Berry connection $\mathbf{A}_n(\mathbf{k}) = i\langle u_n(\mathbf{k}) | \nabla_{\mathbf{k}} | u_n(\mathbf{k}) \rangle$ corresponds to the vector potential with $|u_n(\mathbf{k})\rangle$ denoting the periodic part of the Bloch function of the n -th band. More explicitly, the Berry curvature can be further expressed as

$$\Omega_n(\mathbf{k}) = - \sum_{n' \neq n} \frac{2i\operatorname{Im}\langle u_n | v_x | u_{n'} \rangle \langle u_{n'} | v_y | u_n \rangle}{(\omega_{n'} - \omega_n)^2}, \quad (4)$$

where the summation is over all the occupied valence bands below the gap, $\omega_n \equiv E_n/\hbar$, and $v_{x(y)}$ is the velocity operator. In figure 1(d), the profile of the Berry curvature for the gapped Dirac cones is plotted in red solid lines. The time-reversal symmetry that relates valley K to K' requires that the two valleys have opposite Berry curvatures, leading to a vanishing Chern number. Although the total Chern number is zero, the difference between the Chern numbers that stem from the Berry curvature localized around K/K' valleys is quantized, which gives rise to the QVHE as will be discussed in section 4.

On the other hand, a nonzero total Chern number can only be obtained if the mass terms at valleys K and K' have opposite signs, which breaks the time-reversal symmetry. Such a mechanism has been proposed by Haldane in an elegant model by applying alternating out-of-plane magnetic fields through a honeycomb-lattice structure [9]. As displayed in figure 1(a),

Table 1. Possible materials for realizing TIs. 1st column, possible materials for realizing TIs based on theoretical proposals. 2nd column, the corresponding topological nontrivial band gaps. Here, the phrases ‘dep. strain’ or ‘dep. E’ indicates that the band gap is dependent on the external strain or electric field since some materials are not intrinsic TIs but a phase transition to TI is possible by applying strain or an electric field. 3rd column: some remarks. 4th column: corresponding references. Last column: the current state of experiments; ‘Y’ indicates experimental confirmation, ‘Q’ indicates some experimental discrepancy.

Material	Gap	Remark	Reference	Exp.
G	$\sim \mu\text{eV}$		[23, 29]	
In(TI)/G	~ 7 (21) meV	4×4 supercell	[30]	
5d atom/G	>0.2 eV		[135]	
G/Re/SiC(0 0 0 1)	~ 100 meV		[136]	
Ru/G	~ 10 meV	only 2×2 supercell	[137]	
Bi ₂ Se ₃ /G/Bi ₂ Se ₃	30 meV		[139]	
Bi ₂ Se ₃ /BLG/Bi ₂ Se ₃	44 meV		[115]	
G/BiTeX	70–80 meV	Pressure enhancement	[140]	
Sb ₂ Te ₃ /G/Sb ₂ Te ₃	1.5 meV		[138]	
MoTe ₂ /G/MoTe ₂	3.5 meV		[138]	
2D triphenyl-Bi	43 meV	Intrinsic TI	[146]	
2D triphenyl-Pb	8.6 meV	Organic materials		
Ni ₃ C ₁₂ S ₁₂	22.7 and 9.5 meV	Organic materials, Kagomé lattice,	[149]	Fabricated
Ni ₃ (C ₁₈ H ₁₂ N ₆) ₂	16.6 and 22.4 meV	two TI gaps both away from E_f	[150]	Fabricated
s-triazines	5.50 and 8.27 meV	Honeycomb lattice with $p_{x,y}$ orbitals	[151]	
δ -graphyne	0.59 meV	sp-sp ² hybridization enlarges SOC	[152]	
LaAuO ₃ (TMO)	0.15 eV		[159]	
1T' TMD	10–100 meV	Dirac materials	[161]	
ZrTe ₅ /HfTe ₅	0.1 eV	in the absence of SOC	[163]	
Bi(1 1 0) BL	0.1 eV		[162]	Y
Silicene	1.55 meV	External tunability	[106]	
Germanene	23.9 meV		[106]	
Stanene	73.5 meV		[31]	
Dumbbell stanene	40 meV	Strain engineering	[205]	
MLG	dep. Rashba and electric field	Valley polarized TI	[53, 54]	
HgTe QW	\sim meV		[34, 35, 127]	Y [35]
InAs/GaSb/AlSb QW			[124]	Y [125]
GaN/InN/GaN QW	~ 10 meV		[130]	
GaAs/Ge/GaAs QW	~ 15 meV		[131]	
4-layer BP	~ 5 meV, dep. E	Electric field driven TI	[164]	
multilayer of BP or Sb (1 1 1)	dep. strain/E	Extrinsically driven TI	[164, 190, 191]	
Bi (1 1 1) BL	~ 0.2 –0.6 eV		[170, 173, 174]	Q [179, 189]
Bi on Si(1 1 1)	0.8 eV	Artificial	[180]	
Bi/Pb on H-Si(1 1 1) surface	>0.5 eV	Honeycomb lattice	[181]	
Fun. germanene	dep. strain	-H, -F, -Cl, -Br, -CH ₃	[112, 203]	
	0.3 eV	-I	[203]	
Fun. stanene	~ 0.3 eV	-F, -Cl, -Br, -I, -OH	[32]	
Fun. BL or TL stanene	~ 0.244 eV, dep. strain	-H, strain driven TI	[202]	
Fun. Pb BL	~ 1 eV	-H, -F, -Cl, -Br, -I	[203]	
	0.964 eV	CH ₃	[210]	
Fun. Sb (1 1 1) BL	0.41 eV	-H	[212]	
	0.32–1.08 eV	-H, -F, -Cl, -Br	[207–209]	
	0.386 eV	-CH ₃	[210]	
Fun. Bi (1 1 1) BL	~ 1.03 eV	-H	[206, 212]	
	0.32–1.08 eV	-H, -F, -Cl, -Br	[207–209]	
	0.934 eV	-CH ₃	[210]	
Fun. GaBi	650 meV	-Cl	[196]	
GaAs, BBi, AlBi monolayer	dep. strain	Extrinsically driven TI	[195]	
TlBi	560 meV		[195]	
TlAs and TlSb	131 and 268 meV		[197]	
Bi ₄ Br ₄	0.18 eV	Square lattice	[198, 199]	
Bi ₄ F ₄	0.69 eV		[200]	

Note: The term ‘fabricated’ indicates that the hosting materials have been fabricated but the TI phases has yet been experimentally observed since the intrinsic Fermi energies do not lie inside the topologically nontrivial band gaps. Abbreviations used: G: graphene; BP: black phosphorene; BL: bilayer; TL: trilayer; Exp.: experiment realization; dep.: dependent on; BLG: bilayer graphene; MLG: multilayer graphene; Fun.: functionalized; QW: quantum wells.

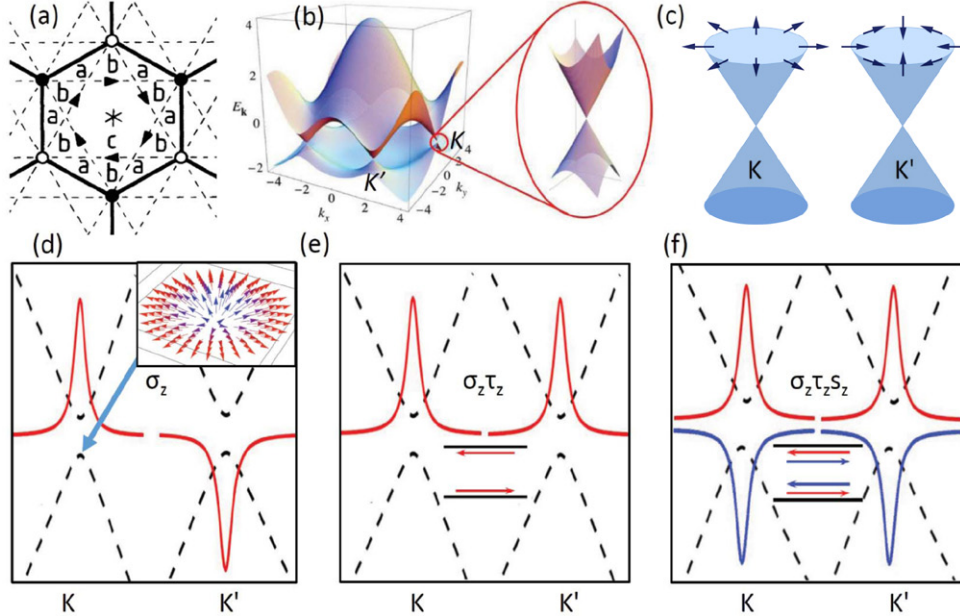


Figure 1. (a)–(c) show the real-space lattice structure, electronic structure and pseudospin texture of pristine graphene, respectively. (d) Black dashed lines show the band structure of spinless particles in a honeycomb lattice with the staggered sublattice potential denoted by σ_z . The mass term opens a band gap at the K/K' points. Inset: pseudospin texture of valence band at K valley, corresponding to a meron. Red solid lines denote the Berry curvature profile, which has opposite signs at the K/K' valleys. (e) Band structure of Haldane's model in the absence of staggered sublattice potential where the Berry curvatures at the K/K' valleys have the same sign. The band gap is topologically nontrivial and shows the QAHE with a Chern number $C = 1$; the corresponding edge state is plotted in the inset. In this model, an alternating magnetic flux is applied to the honeycomb lattice. As shown in (a), the whole 2D plane is divided into three regions labeled by a, b, and c where the magnetic flux through a and b are of the same magnitude but opposite sign while region c has no magnetic flux. (f) Kane–Mele model: The intrinsic spin–orbit coupling of graphene $\sigma_z\tau_z\sigma_z$ gives rise to two copies of Haldane's model with spin-up and -down bands of opposite Berry curvature as shown by red and blue solid lines, respectively. The corresponding Chern numbers of 1 and -1 lead to counter-propagating helical edge states shown in the inset. Figure (a) reprinted with permission from [9], copyright 1988 by the American Physical Society. Figure (b) reprinted with permission from [22], copyright 2010 by the American Physical Society. Inset of figure (d) reprinted with permission from [88], copyright Springer 2012.

the magnetic fields of opposite direction are applied in the ‘a’ and ‘b’ regions, i.e. $\phi_a = -\phi_b$. The zero net magnetic flux in a closed path surrounding the unit cell does not affect the nearest-neighbor hopping amplitude t_1 . However, for the next-nearest-neighbor hopping amplitude t_2 , the net flux is nonzero, and is given by $\phi = 2\pi(2\phi_a + \phi_b)/\phi_0$ with $\phi_0 = h/e$. Thus, t_2 acquires a phase factor to become $t_2 e^{i\phi}$ [9]. Because this factor is position-independent, the system also possesses translational symmetry. The corresponding low-energy continuum spinless Hamiltonian can be expressed as [37]:

$$H(\mathbf{k}) = v(\tau_z k_x \sigma_x + k_y \sigma_y) + M \sigma_z + m \tau_z \sigma_z \\ = v \begin{bmatrix} M + m & \pi^\dagger \\ \pi & -(M + m) \\ M - m & -\pi \\ -\pi^\dagger & -(M - m) \end{bmatrix}, \quad (5)$$

where the second and third terms originate from the staggered sublattice potentials and next-nearest-neighbor hopping terms, respectively, with $m = -3\sqrt{3}t_2 \sin \phi$ and $\pi(\pi^\dagger) = k_x \pm ik_y$. The mass terms at K and K' points are modified to be $(M + m)$ and $(M - m)$. As a consequence, the Chern numbers for valleys KK' are changed to $C_K = 0.5 \operatorname{sgn}(M + m)$ and $C_{K'} = 0.5 \operatorname{sgn}(m - M)$. When $|m| > |M|$, the signs of the Merons at valleys K and K' are identical and thus $C_K = C_{K'}$,

giving rise to the QAHE characterized by a nonzero Chern number $C = C_K + C_{K'} = \operatorname{sgn}(m)$. This corresponds to a pair of chirally propagating edge states along the boundaries as displayed in figure 1(e), exhibiting exactly the same transport properties as those of the magnetic field induced quantum Hall effect, for example, robustness against any kind of weak disorder [9, 23].

2.2. Honeycomb lattices of group-IV elements

2.2.1. Graphene: Kane–Mele model. The Haldane model has proved to be a great success in advancing the design of dissipationless electronics in the absence of a magnetic field. However, in the 1980s it was unimaginable that such an ideal toy model could be realized in practice. The primary reasons were that (i) the 2D materials were believed to be unstable in nature [94], and (ii) the alternating magnetic fluxes were extremely difficult to impose in experiment. Therefore, for a rather long time, very little progress was made following Haldane's proposal until the graphene was successful exfoliated. Graphene is a 2D atomic crystal layer composed of carbon atoms arranged on a honeycomb lattice, making it an excellent test platform. Based on the earlier work of DiVincenzo and Mele on the spin–orbit coupling of graphite [95], in 2005 Kane and Mele in a seminal paper proposed that, in the long wavelength limit,

the intrinsic spin-orbit coupling of graphene due to the next-nearest-neighbor hopping can be written as two copies of the Haldane model with the mass terms of the spin-up and spin-down electrons having opposite signs:

$$H(\mathbf{k}) = v(\tau_z k_x \sigma_x + k_y \sigma_y) + m \tau_z \sigma_z s_z, \quad (6)$$

where $\mathbf{s} = (s_x, s_y, s_z)$ are the spin-Pauli matrices. For each single spin, the time-reversal symmetry is effectively broken and the mass term gives rise to a nonzero Chern number according to the Haldane model. Specifically, for the spin-up and -down bands, the mass terms are respectively m and $-m$, leading to the Chern numbers $C_\uparrow = \text{sgn}(m)$ and $C_\downarrow = -\text{sgn}(m)$ corresponding to the counter-propagating edge states of opposite spins (see inset of figure 1(f)). This leads to a vanishing charge Hall conductance but quantized spin-Hall conductance when s_z is a good quantum number. Thus, this is called the QSHE. The two copies of edge modes with opposite spins are related to each other by the Kramers degeneracy theorem since time-reversal invariance is retrieved by the combination of $\tau_z \sigma_z$ with a Zeeman term s_z .

Compared with the quantum Hall effect, where the spatial separation of counter-propagating edge states protects them from any weak disorder induced backscattering, the counter-propagating edge modes of opposite spins are spatially overlapped and thus the backscattering is possible. However, by studying the four-terminal transport properties of this system, Sheng *et al* found that the spin-related transport properties are rather robust/insensitive to the sample boundary conditions (such as zigzag or armchair-type boundaries) and exhibit a quantized spin-Hall conductance in the presence of relatively large disorder strengths [96]. Moreover, the robust time-reversal symmetry protected edge states are also present even when s_z is no longer a good quantum number, as with Rashba spin-orbit coupling [24].

This robustness reveals a most important feature of the QSHE, i.e. the elastic backscattering between the two states within a Kramers degenerate pair is forbidden due to the protection from time-reversal symmetry [39]. However, back-scattering between states in different Kramers degenerate pairs is allowed, making them annihilate together. Therefore, the system will become a trivial insulator if there is an even number of Kramers degenerate pairs at each boundary and the topologically nontrivial phase occurs only when the number of Kramers degenerate pair is odd, hence the name ‘topological insulator’ coined by Kane and Mele [24]. Such a property intrinsically classifies the time-reversal symmetric insulators into two classes, characterized by the \mathbb{Z}_2 topological invariant [24]:

$$\mathbb{Z}_2 = \frac{1}{2\pi} \left[\oint_{\partial \text{HBZ}} d\mathbf{k} \cdot \mathbf{A}(\mathbf{k}) - \int_{\text{HBZ}} d^2k \Omega_z(\mathbf{k}) \right] \text{mod}(2). \quad (7)$$

The presence of the mod(2) term makes the topological invariant can only take two values ‘0’ and ‘1’ indicating topologically trivial and nontrivial respectively, which reflects the binary classification of insulator with even or odd numbers of Kramers pairs. In addition, there are other definitions of the \mathbb{Z}_2 topological indices, which have been well described in

[97] and [98]. For clarity and correctness of the definitions, hereinbelow, we refer to the QSHE as a ‘2D \mathbb{Z}_2 topological insulator (2D \mathbb{Z}_2 TI)’ no matter whether the spin is a good quantum number or not.

Although the Kane-Mele model was shown to be able to open up a topologically nontrivial gap that can host a 2D \mathbb{Z}_2 TI phase, the intrinsic spin-orbit coupling is extremely weak that makes the realization of 2D \mathbb{Z}_2 TI in the pristine graphene impossible [25–29]. Nevertheless, intensive studies have shown that the intrinsic spin-orbit coupling of graphene can be greatly enhanced via external means, e.g. by adsorbing some heavy atoms, and a variety of graphene-like materials (e.g. low-buckled honeycomb lattice systems) can naturally possess stronger intrinsic spin-orbit couplings as reviewed in the following sections.

2.2.2. Low-buckled honeycomb lattice. The Kane-Mele model can also be applied to the low-buckled honeycomb-lattice structures of other group-IV element based 2D atomic crystal layers, e.g. silicene [99–102], germanene [99, 103], and stanene [32], which are the respective counterparts of silicone, germanium, and tin. Similar structures exist in the 2D alloys of these elements [99, 104, 105]. The low-buckled honeycomb structure originates from the larger interatomic distances in these systems [31, 106] and makes the atomic orbitals mix the sp^3 hybridization with the sp^2 one, which results in a first-order contribution of the atomic spin-orbit coupling to the intrinsic spin-orbit coupling of the Bloch electrons (see figure 7(c)). Because of the higher atomic numbers of Si, Ge, and Sn, their larger intrinsic spin-orbit coupling induced bulk gaps can reach the orders of 1, 10, and 100 meV, respectively, making the \mathbb{Z}_2 TIs measurable under experimentally achievable temperatures [31, 32, 103]. In addition, although the low-buckled structure naturally breaks the mirror symmetry about the plane leading to an intrinsic Rashba-type spin-orbit coupling, this is not detrimental to the 2D \mathbb{Z}_2 TIs since the intrinsic Rashba spin-orbit coupling is momentum-dependent and vanishes at the Dirac K/K' points [31]. Another striking property of the low-buckled structure is the external tunability when an electric field [107–110] or strain [111, 112] is applied.

2.2.3. Multilayer graphene. Although the Bernal-stacked multilayer graphene is also a zero-gap semi-metal, the inter-layer coupling modifies the linear Dirac dispersion at valleys KK' of the monolayer graphene to become non-linear in the multilayer case [113]. We begin with bilayer graphene as an example that has quadratic bands touching at K and K' points as displayed in figure 2(a), which gives rise to a different pseudospin texture from that of the monolayer graphene of figure 2(b) [114]. In the presence of intrinsic spin-orbit coupling, even though either top or bottom layer can form a separate TI, the interlayer coupling induced combination of these two TIs gives rise to a trivial insulator [67, 115]. However, it is found that the extrinsic Rashba spin-orbit coupling due to the breaking of the mirror reflection symmetry $z \rightarrow -z$ by, e.g. applying a perpendicular electric field [45], adsorbing atoms [116], or placing on top of a metallic substrate [116–118], can

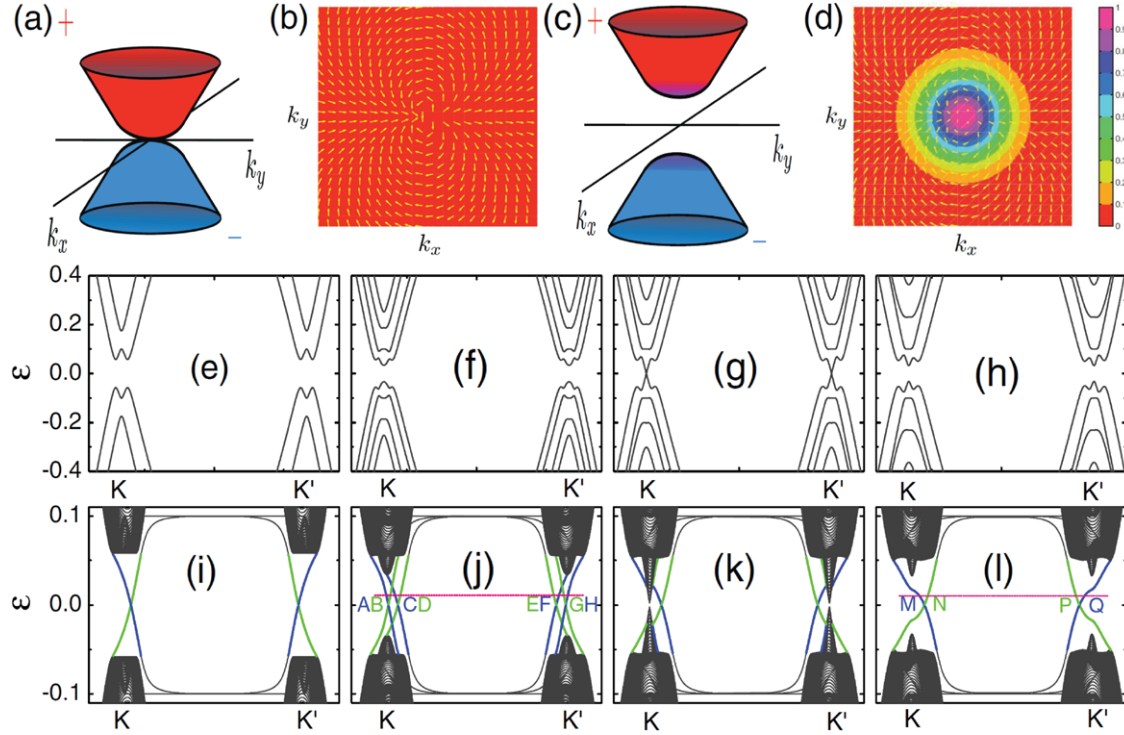


Figure 2. (a) and (c): Electronic structure of Bernal stacked bilayer graphene without and with different layer potentials. (b) and (d): Pseudospin texture of bilayer graphene corresponding to (a) and (c). (e)–(h): Bulk band structures along high-symmetry lines for different strengths of Rashba spin–orbit coupling. (i)–(l): Band structure of zigzag bilayer graphene nanoribbon corresponding to figures (e)–(h). Figures (a)–(d) reprinted with permission from [114]. Figures (e)–(l) reprinted figure with permission from [53], copyright 2011 by the American Physical Society.

induce a \mathbb{Z}_2 TI assisted by the interlayer potential difference [53, 119]. Such a TI phase can be understood in two limits as described in the following.

When the Rashba spin–orbit coupling λ_R is much larger than the interlayer potential difference U , the low-energy continuum model Hamiltonian can be expressed as

$$H_K^{\text{eff}} = \frac{1}{\lambda_R} \begin{bmatrix} U\lambda_R & iv^2(\pi^\dagger)^2 & 0 & 2it_\perp v\pi^\dagger \\ -iv^2\pi^2 & U\lambda_R & 0 & 0 \\ 0 & 0 & -U\lambda_R & iv^2(\pi^\dagger)^2 \\ -2it_\perp v\pi & 0 & -iv^2\pi^2 & -U\lambda_R \end{bmatrix}, \quad (8)$$

where the basis functions are mainly decided by $\{A_{1\uparrow}, B_{1\downarrow}, A_{2\uparrow}, B_{2\downarrow}\}$ [119]. In the absence of a perpendicular electric field, the strong Rashba spin–orbit coupling lifts the spin degeneracy of the bands in the K and K' valleys by mixing the upward and downward spins as well as the layer pseudospin. However, the gapless character is preserved leading to both linear and quadratic band touching, which can be lifted by either a Zeeman term or an inequivalent layer potential resulting in a QAHE (see section 3) or TI [119]. The weak inequivalent layer potential lifts both linear and quadratic band touching and gives rise to a Chern number at valley K $C_K = \text{sgn}(U)$, mainly attributed to the gapped linear dispersion. The symmetric time-reversal counterpart lies in K' valley with $C_{K'} = -\text{sgn}(U)$. As a result, the two copies of QAHE possess opposite spin-orientations and valley indices, i.e. opposite momenta, corresponding to a TI with helical edge states. Different from the TI in monolayer graphene where the inversion symmetry and time-reversal

symmetry guarantee the spin degeneracy of edge states, which have dispersion curves crossing the Brillouin zone and hence do not have a well-defined valley index, spin degeneracy is absent in bilayer graphene due to the breaking of inversion symmetry and edge states have a well-defined valley index, as can be seen in figure 2(l). As a consequence, these edge states are protected not only by the time-reversal symmetry but also by their large momentum separation, displaying both TI and QVHE characteristics (see also section 4).

On the other hand, in bilayer graphene, chiral symmetry also appears with the sublattices separately coming from the top and bottom layers. The separate contributions of sublattices from different layers makes it possible to induce staggered sublattice potentials by applying an external perpendicular electric field that can open a band gap, as shown in figure 2(c). Different from monolayer graphene where the pseudospin texture at each valley gives a half Chern number per spin by forming a meron, the quadratic coupling between these two sublattices leads to different pseudospin textures for gapped bilayer graphene as displayed in figure 2(d), that leads to a unit Chern number per spin and hence QVHE with gapless edge modes for zigzag nanoribbon (see also section 4). Nevertheless, even numbers of Kramers pairs at each boundary from both the spin and valley degeneracies makes this phase topologically trivial with $\mathbb{Z}_2 = 0$ [53]. When the Rashba spin–orbit coupling is included, the spin-up and -down states are mixed to lift the spin degeneracy of the energy bands. The increase of λ_R induces an inversion between the lowest conduction and highest valence bands by closing and reopening

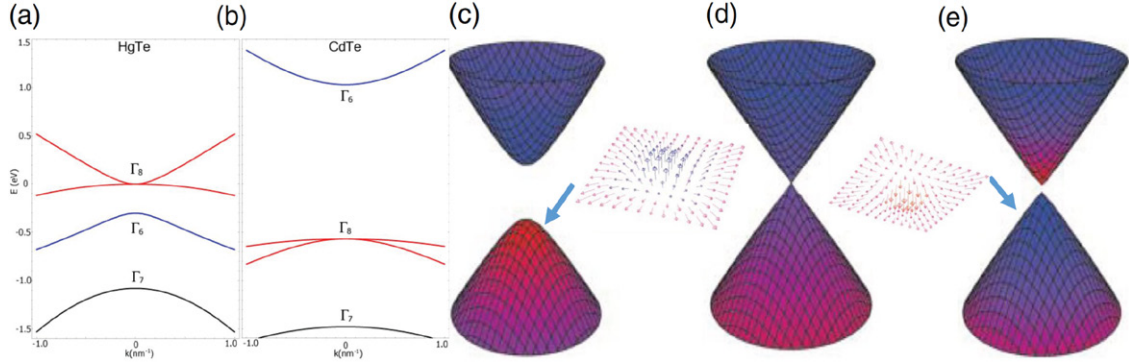


Figure 3. (a) and (b): Bulk energy bands of HgTe and CdTe near the Γ point. (c)–(e) Low energy band structure of CdTe/HgTe/CdTe quantum well in the normal regime, critical point, and inverted regime, respectively. Each band is double degenerate due to inversion symmetry and time reversal symmetry. The inset figures between (c)–(e) show the pseudospin texture of the valence band corresponding to the upper panel. Left and right inset figures show two merons of opposite sign indicating the change of Chern number by 1. Figures (a)–(e) reprinted figure with permission from [34].

the band gap at the Dirac points, as shown in figures 2(e)–(h). During the phase transition, the two-fold spin degenerate edge states at each boundary become coupled and split by the Rashba spin-orbit coupling. This eliminates two edges states at each boundary and keeps only one Kramers degenerate pair that is topologically protected by the time-reversal symmetry as displayed in figures 2(i)–(l). Such a topological phase transition from a trivial insulator to a \mathbb{Z}_2 TI can be well interpreted by the two-band BHZ model, as will be reviewed in the following section [119, 120].

Similar results can be reached for the ABC-stacked trilayer graphene [54]. However, different from the bilayer case with one pair of states at each valley, there is an unbalanced number of edge states at the two boundaries of a zigzag-terminated nanoribbon. Specifically, there are five pairs of spin-helical edge states located at one boundary with three pairs at the other boundary. When inter-valley scattering is introduced in the armchair ribbon, scattering destroys extra Kramers degenerate pairs and leaves only one pair of spin-helical edge states in both boundaries. Note that the number of spin-helical pairs at any boundary is strictly consistent with the requirement of odd pairs of spin-helical edge modes in \mathbb{Z}_2 TIs [54].

2.3. Band-inversion in quantum wells

Parallel to the idea of TI based on the Dirac semi-metal in graphene-like materials with half-filled π -bands, another route to realize 2D \mathbb{Z}_2 TIs is to utilize a semiconductor with fully-filled valence bands [34, 35, 121–125]. Following the realization of the 4D generalization of the quantum Hall effect and spurred by the requirement of dissipationless spin current [15–19], it was suggested to look for the QSHE in zinc-blende semiconductors [33]. Soon after, a quantum-well based \mathbb{Z}_2 TI was theoretically proposed in a CdTe/HgTe/CdTe heterostructure with proper tuning of the quantum-well thickness [34] that has been successfully observed experimentally [35, 126].

For conventional semiconductors composed of light elements, the filled valence bands are gapped from the conduction bands as shown in figure 3(b) for CdTe. By contrast, for HgTe, an inversion between Γ_6 and Γ_8 bands makes this

material a zero-gap semiconductor as displayed in figure 3(a). In the symmetric quantum well of CdTe/HgTe/CdTe, a topologically trivial insulating phase occurs for the thin HgTe layer because of the dominating contribution from CdTe. When the thickness of HgTe increases, a band inversion occurs with increasing contribution from HgTe. At the critical point, the low-energy continuum model Hamiltonian can be written as

$$H_{\text{eff}}(\mathbf{k}) = \epsilon(k) + \begin{bmatrix} m(k) & A\pi^\dagger \\ A^*\pi & -m(k) \\ m(-k) & -A^*\pi \\ -A\pi^\dagger & -m(-k) \end{bmatrix}, \quad (9)$$

where the symmetric mass term is $\epsilon(k) = C - D(k_x^2 + k_y^2)$ while the asymmetric mass term is $m(k) = M - B(k_x^2 + k_y^2)$. The two decoupled blocks are related by the time-reversal operation and hence we only consider the upper-block in our following discussion. The 2×2 effective Hamiltonian be regarded as the kinetic energy of a massive Dirac fermion expressed in the pseudospin Hilbert space. However, different from the previously introduced mass term in graphene, the mass term $m(k)$ has a momentum dependence that gives rise to different pseudospin textures, depending on the sign of M and B . For a positive B , when M is also positive, the mass term $m(k)$ is positive around $\mathbf{k} = 0$ but negative for a large momentum. The corresponding pseudospin texture is schematically plotted in the inset of figure 3(c), representing two merons with opposite signs corresponding to a trivial insulator. When M decrease to zero, the gapless Dirac dispersion appears as displayed in figure 3(d). When M is negative, the band gap reopens and the mass term is negative for both the zero and large momenta, corresponding to a skyrmion that is composed of two merons with the same sign, as displayed in figure 3(e), and carries a unit Chern number $C = 1$. The time-reversal counterpart of this block possesses a Chern number of $C = -1$. The two decoupled blocks therefore result in a vanishing total Chern number but counter-propagating edge states, forming a Kramers degenerate pair corresponding to a \mathbb{Z}_2 TI [34, 127].

In the symmetric quantum well of CdTe/HgTe/CdTe, by neglecting the bulk inversion asymmetry whose effect is small

for HgTe based structure [128], the inversion symmetry is preserved, allowing the eigenstates to possess well-defined parity. In the trivial insulating regime, the conduction band edge has odd parity while the valence edge has even parity [34]. The inversion symmetry guarantees the occurrence of band inversion for the time-reversal symmetric momentum, which induces a parity exchange, leading to a TI [34, 98]. For the structural inversion asymmetric quantum wells of AlSb/InAs/GaSb/AlSb, the band inversion can also occur and induce a \mathbb{Z}_2 TI phase, as theoretically predicted in [124], and later experimentally realized [121, 122, 125]. However, at the critical point of the band inversion, two non-degenerate Dirac cones occur at the momenta of \mathbf{k}_0 and $-\mathbf{k}_0$ [129], which is different from that in the inversion symmetric system, where the doubly degenerate Dirac cones exist around the time-reversal symmetric momentum. The case of bilayer graphene is similar to the asymmetric quantum well with \mathbf{k}_0 and $-\mathbf{k}_0$ corresponding to the K and K' points, respectively [53, 119].

In addition to materials with inverted band structure, e.g. HgTe and InAs/GaSb heterostructure, band inversion induced TIs can also appear in conventional semiconductor composed quantum wells, like GaN/InN/GaN and GaAs/Ge/GaAs quantum wells [130, 131]. Due to the sizable band gap of the conventional semiconductors, large enough electric field is required to reduce the band gap and induce band inversion. This large electric field is difficult to achieve via gate technology but may be realized by fabricating high-quality semiconductor heterostructure. For example, in GaN/InN/GaN quantum wells, the large strain due to the lattice mismatch between InN and GaN can induce sizable electric field via the strong piezoelectric effect [130]. Alternatively, in GaAs/Ge/GaAs quantum wells, the strong electric field appears since the charge transfer at As-Ge interface is different from that at Ge-Ga interface [131]. Simultaneously, the large electric field also enhance the spin-orbit coupling and hence the nontrivial band gap of TIs originating from the band inversion.

2.4. Graphene-based experimental prototypes

Although the 2D \mathbb{Z}_2 TI was first predicted in monolayer graphene, it is regarded as extremely unrealistic since the intrinsic spin-orbit coupling in graphene is very minute due to the small atomic number of carbon and the distinctive planar honeycomb lattice [25–29]. Specifically, in ideal planar graphene, the spin-orbit coupling of the π -band is only about 1 μeV due to the second-order contribution via the virtual transitions to the σ -orbit [26, 29]. Even though this value can be further enhanced to about 24 μeV through virtual transitions to d -orbital, the intrinsic spin-orbit coupling is still too weak to open an experimentally observable band gap [29]. Therefore, one has to turn to external means to tune the intrinsic-type spin-orbit coupling. For example, Weeks *et al* reported that the adsorption of indium (In) or thallium (Tl) atoms is able to significantly increase the intrinsic spin-orbit coupling [30]. To achieve this, several necessary conditions must be satisfied: First, the impurity bands should be farther away from the Fermi level; Second, the magnetization must not be allowed to

preserve the time-reversal symmetry; Third, the Rashba spin-orbit coupling due to the breaking of the mirror reflection about the graphene plane from adsorption should be much smaller than the enhanced intrinsic-type spin-orbit coupling. Although the Rashba term plays a detrimental role, the intrinsic spin-orbit coupling induced TI phase can be stabilized as long as the Rashba term is not dominant.

As concrete examples for the In and Tl adsorption, the energy of the outer p -shell electrons is far away from the Dirac point, and their coupling with the graphene's π -band electrons can transmit their strong spin-orbit coupling to graphene via the second-order perturbation. The resulting sizable intrinsic spin-orbit coupling opens a bulk band gap of about 7 (21) meV in the In (Tl) adsorption case [30]. Although this numerical calculation is based on a periodic adsorption that is beyond current experimental capabilities, it is shown that even when the adatoms are randomly distributed, the enhanced spin-orbit coupling from the adsorption is rather stable while the inter-valley scattering that is unfavorable for TIs is effectively suppressed [132]. Therefore, these findings indicate a high possibility of realizing \mathbb{Z}_2 TIs in graphene. Yet, experimentally, it has been found that the adatoms are inclined to form clusters rather than to distribute individually [133]. But surprisingly, Cresti *et al* reported that even when the adsorbed heavy atoms (e.g. Tl) form islands or clusters on top of graphene, a nearly quantized plateau of spin-Hall conductance can still be formed [134].

In contrast to the In and Tl with outer p shell, the outer d -orbitals of the 5d-transition metal adatoms are not far away from the Dirac point of graphene, such as Os, Ir and Re. These outer d -orbitals can strongly couple and hybridize with graphene π bands, and thus greatly alter the linear Dirac dispersion in the high adsorption case [135, 136]. The dominate contribution from d -orbitals at the Fermi energy leads to large spin-orbit coupling and hence large topologically nontrivial band gap [135, 136]. Similar effect can also be found in graphene with Ru adatom in 2×2 supercell, which is a 4d-transition metal [137]. For these adatoms with outer d -orbital, the spontaneous magnetism may be formed due to the strong electron-electron correlation, which yet can be suppressed by external electric field [135].

Apart from the adsorption of heavy atoms, the proximity effect of thin-film insulators with strong spin-orbit couplings is another effective method to enhance the spin-orbit coupling in graphene [115, 138–143]. The *ab initio* calculation shows that the spin-orbit coupling of graphene can be increased up to the order of meV through sandwiching with Sb_2Te_3 or MoTe_2 slabs, where the two Dirac cones of graphene are folded into Γ point due to the $\sqrt{3} \times \sqrt{3}$ superlattice and the inter-valley scattering induces a topologically trivial band gap. However, the folded Dirac cones are located inside the bulk band gap of the neighbor insulators, which can introduce strong spin-orbit coupling in graphene to overcomes the trivial band gap and results in a topologically nontrivial phase [138]. When the top of the valence bands or the bottom of the conduction bands of the sandwiching materials is close to the Dirac points of graphene, for example Bi_2Se_3 , the inversion between the bands of

sandwiching materials and graphene's π bands can also result in a \mathbb{Z}_2 TI [139]. Similar effect can be found in bilayer graphene sandwiched by Bi_2Se_3 [115]. In addition, the van der Waals heterostructure between graphene and BiTeX ($X = \text{Cl}, \text{Br}, \text{and I}$) chalcogenides can form another family of \mathbb{Z}_2 TIs with a bulk band gap of around 70–80 meV [140].

2.5. Other Dirac materials: organic and artificial lattices, and transition-metal compounds

The low-energy physics dominated by linear Dirac dispersion is not limited to graphene or other atomic crystal layers of group-IV elements [144, 145]. In analogy to silicene, the 2D organometallic lattices composed of triphenyl and lead (Pb) or bismuth (Bi) naturally form a low-buckled honeycomb lattice [146]. For the triphenyl-lead honeycomb lattice, its electronic structure proximity to the Fermi energy shows linear Dirac dispersion similar to that in silicene. When the spin-orbit coupling is considered, the intrinsic Kane-Mele type spin-orbit coupling emerges, opening a bulk band gap and harbouring a \mathbb{Z}_2 TI phase. For the triphenyl-bismuth honeycomb lattice, however, although a topologically nontrivial band gap is also opened at the Dirac points, the Fermi-level is above the band gap since the bismuth atom has one more valence electron than the lead atom. Although these materials are theoretically shown to be TIs, they still await experimental synthesis. On the other hand, recent experimental progress has seen the synthesis of Kagomé organometallic lattices, such as lattices of $\text{Ni}_3\text{C}_{12}\text{S}_{12}$ [147] and $\text{Ni}_3(\text{C}_{18}\text{H}_{12}\text{N}_6)_2$ [148]. These two lattices also exhibit linear Dirac dispersion at K/K' points, which can give rise to a TI phase in the presence of spin-orbit coupling. However, the topologically nontrivial band gap is much higher than the Fermi energy level, making the experimental observation of TI difficult [149, 150]. In addition to these organometallic lattices, \mathbb{Z}_2 TI has also been reported in metal-atom free systems, e.g. honeycomb lattices of s-triazines [151] and δ -graphyne [152], where the linear Dirac dispersions appear at the K/K' valleys close to the Fermi level.

In addition to the organic honeycomb lattice structures, various artificial honeycomb lattices can also provide good platforms for Dirac-cone related physics [153]. For example, Dirac cones have been theoretically proposed in honeycomb lattices of semiconductor nanocrystal [154]. In HgTe nanocrystal, the combination of Dirac cones and strong spin-orbit coupling leads to a large gap \mathbb{Z}_2 TI [155]. In recent experiment, Dirac-dispersion has been reported in honeycomb optical lattices with ultracold atoms [156] wherein the Haldane's model for QAHE has been experimentally observed (see section 3.2.6) by introducing appropriate Berry curvatures [157]. Through combining two copies of QAHE with opposite Chern numbers, the formation of the \mathbb{Z}_2 TI should be possible in such kind of systems.

Moreover, the recent experimental progress in fabricating heterostructures of transition-metal oxides (TMOs) [158] also inspires the investigation of their topological properties [159, 160]. In the (1 1 1) bilayer structure of perovskite TMOs, two triangular lattices of the transition-metal ions at the neighboring (1 1 1) surfaces form a buckled honeycomb lattice. In these

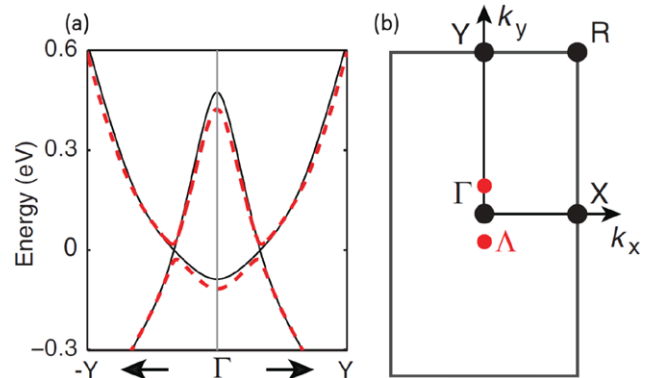


Figure 4. (a) Band structure and (b) Brillouin zone of 1T'-MoS₂. (a) Band structures with (red dashed line) and without (black solid line) spin-orbit coupling. (B) Four time-reversal invariant momenta are marked by black dots and labeled as Γ , X , Y , and R . Red dots: the two Dirac points labelled as Λ . Reprinted figure with permission from [161].

structures, the trigonal crystalline field further splits the e_g or t_{2g} orbitals induced by the octahedral crystal field. These split orbitals can then form linear-dispersed Dirac cones, which can be gapped by further including the spin-orbit coupling to harbour \mathbb{Z}_2 TIs. Based on the first-principles calculations, the LaAuO_3 bilayer was predicted to be a \mathbb{Z}_2 TI with a band gap of ~ 0.15 eV [159, 160]. Apart from the lattices with hexagonal first Brillouin zone, Dirac dispersions have also been reported in systems with a rectangular first Brillouin zone where the Dirac points lie on the high symmetric line along Γ -X or Γ -Y [161–164]. In 2D transition metal dichalcogenides (TMD) with a 1T' structure [161], two Dirac cones are present at Λ points near the Γ point in the absence of spin-orbit coupling, as denoted by the black solid lines in figure 4(a) and the Λ points labelled by solid red circles in figure 4(b). The introduction of the spin-orbit coupling lifts the degeneracy at Dirac points and gives rise to a \mathbb{Z}_2 TI. For the other cases, like in $\text{Bi}(110)$ bilayer [162], transition-metal pentatelluride [163], and 4-layer black phosphorene under an electric field [164], although the physical origins of the Dirac cones in the absence of spin-orbit coupling are different, the band gaps opened by the spin-orbit coupling can host a \mathbb{Z}_2 TI. The resulting edge states of a Bi (1 1 0) bilayer has already been observed experimentally at a temperature of up to 77 K [162].

2.6. Buckled honeycomb lattice of group-V elements

2.6.1. Bismuth bilayer. In addition to the semiconductor quantum well, real 2D semiconductors with fully filled valence bands have also been theoretically reported in the atomic crystal layer structure of group-V elements such as black and blue phosphorene [165], arsenene [166], and antimony (Sb) and bismuth (Bi) bilayers in the (1 1 1) orientation [167–170]. Among these 2D layer structures, black phosphorene has a puckered structure while the others have a stable buckled honeycomb-lattice structure [165–170]. However, in contrast to the honeycomb lattices composed of group-IV elements where the π -band from the p_z orbital is half-filled to form a semi-metallic phase with the Fermi-level lying at

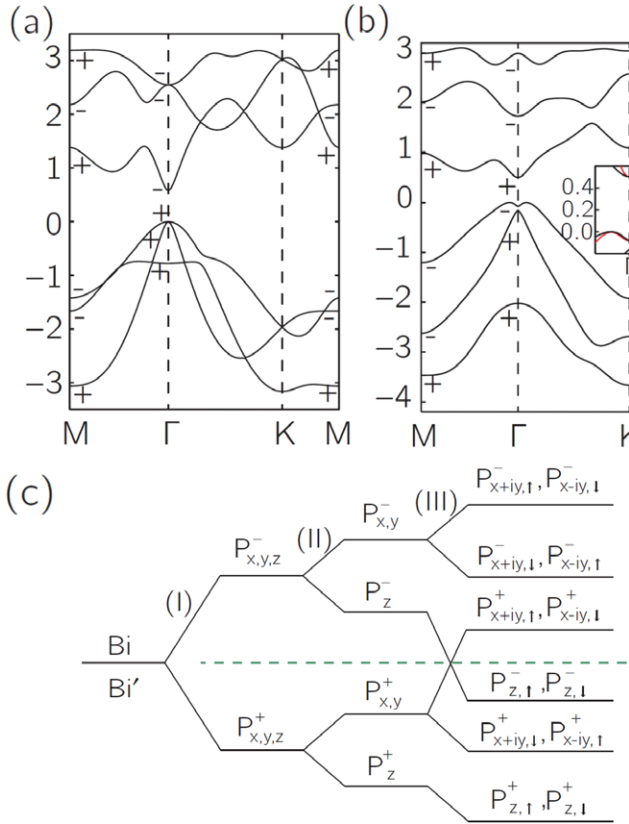


Figure 5. Band structure and corresponding wavefunction parity eigenvalues of a single Bi(1 1 1) bilayer (a) without and (b) with spin–orbit coupling. Inset of (b): zoom in on two inverted bands at Γ . The highest occupied energy level is set to zero. (c) Schematic of the evolution from the atomic $p_{x,y,z}$ orbitals of atoms into the conduction and valence bands of single Bi(1 1 1) bilayer at the Γ point. Three stages (I), (II) and (III) take into account the effects from chemical bonding, crystal-field splitting and spin–orbit coupling, respectively. The green dashed line represents the chemical potential. Note that the p_z orbitals slightly hybridize with the $p_{x,y}$ orbitals at stage (III). Reprinted with permission from [172], copyright 2014 by the American Physical Society.

the Dirac points, the group-V elements have five valence electrons that fill all the valence bands from the molecular orbitals, which leads to the insulating band structure. For these group-V element based structures, the increase in atomic number also decreases the electronegativity that weakens the valence bonds, which shrinks the band gap. Moreover, as the atomic number increases, the indirect band gaps for blue phosphorene [165] and arsenene [166] become the direct gap at the Γ point for the Sb and Bi bilayer [169–171]. For example, as shown in figure 5(a), the band gap for Bi bilayer is opened up at Γ where the valence bands are dominated by $p_{x,y}$ orbitals with even parity, whereas the conductance bands are dominated by a p_z orbital with odd parity [172].

Another result of increasing the atomic number is to enhance the spin–orbit coupling of the Bloch electrons [45]. As a result, in the Bi bilayer composed of the heaviest group-V element, the spin–orbit coupling is so strong to induce a band inversion between the conduction and valence bands and the formation of a TI phase (see figures 5(b) and (c)) [170, 172–178]. As the layer thickness increases, the corresponding

band gap decreases due to the inter-layer coupling and the 2D \mathbb{Z}_2 TI phase preserves for systems with layer number $N < 5$ [173].

In the above theoretical studies, all the large-gap 2D \mathbb{Z}_2 TIs were predicted for free-standing systems. However, in reality, substrates are a necessity in most situations, which will influence the intrinsic topological properties of certain materials due to interfacial and proximity effects such as the small variation of lattice constant, unexpected charge transfer and the resultant Rashba spin–orbit coupling [179]. Therefore, suitable substrates to support room-temperature TIs are important for potential device applications [180–184]. The influence of several traditional substrates, e.g. hexagonal boron-nitride (h-BN) and silicon-carbide [184], has been intensively studied. It has been shown that h-BN is an ideal substrate for stabilizing the topologically nontrivial phase of a freestanding Bi bilayer.

In experiment, the time-reversal symmetry-protected edge states have been observed recently in an exfoliated Bi (1 1 1) bilayer [185], and in a Bi bilayer on a substrate, e.g. Bi_2Te_3 [186, 187] and $\text{Bi}_2\text{Te}_2\text{Se}$ [188]. However, for the Bi bilayer on a Bi substrate, Takayama *et al* recently reported their ARPES observations seemed to indicate that their one-dimensional edge states of a Bi bilayer on a Bi substrate were of a non-topological nature [179], which is inconsistent with the conclusion from the scanning tunneling microscopy measurements by Drozdov *et al* [189].

2.6.2. Other group-V elements. Similar to the Bi(1 1 1) bilayer, a Sb(1 1 1) bilayer also possesses a buckled honeycomb lattice but it is a robust trivial band insulator in the monolayer case due to its weaker spin–orbit coupling. However, stacking of the Sb(1 1 1) bilayers reduces the band gap and a TI phase occurs when the stacking reaches four layers [190, 191]. In addition to the buckled structure, as the atomic number decreases, a stable puckered structure can also be formed due to enhancement of the buckling via reduced atom size, for example in black phosphorus [164] and arsenene [166]. However, both the buckled and puckered structures of monolayer arsenide and phosphorus are found to be topologically trivial insulators. Nevertheless, in the stacked black phosphorus with three to four layers, the external perpendicular electric field can drive a topological phase transition from a trivial insulator into a TI via a band inversion near the Γ point [164]. Similar results may be expected for arsenide thin films, which to our knowledge has not been reported yet.

2.6.3. III–V, VII–V, and IV–VI compounds. Another direct analogy to the low-buckled honeycomb structure of group-IV elements is the binary III–V compounds based on the B-In and N-Sb elements [192, 193]. However, different from the honeycomb lattice of group-IV elements, the inversion-symmetry breaking in these compounds opens a large local band gap at the K and K' valleys. On the other hand, the conductance and valence band edges, which determine the low-energy physics, are mainly influenced by the s and $p_{x,y}$ orbitals respectively for some materials and are located at the Γ point. Although the spin–orbit coupling is not strong enough to induce band

inversion for some materials composed of light elements, the buckled honeycomb lattice provides the possibility to tuning the topological phase via external means, like strain and electric field. As an example of As-based III–V compounds, the GaAs monolayer has been shown to be a \mathbb{Z}_2 TI with a band gap as wide as 257 meV under certain strain conditions. Different from Kane–Mele’s model, the topologically non-trivial phase is induced by the s - p band inversion via an external strain at the Γ point [194].

Later, the binary III–V compound systems were extended to the Bi-based family [195]. The Bi based compounds with low-buckled structures, i.e. XBi ($X = Ga, In, Tl$), are natural \mathbb{Z}_2 TIs due to the strong spin–orbit coupling. In particular, the bulk band gap of $TIBi$ can be as large as 560 meV, which is possible for room-temperature measurement of the topological phase. For $X = B$ and Al , although the intrinsic systems are topologically trivial insulators, an externally applied strain can drive the systems to be \mathbb{Z}_2 TIs. Functionalization of the binary group III–V systems can further increase the bulk band gaps, for instance, chloridization of $GaBi$ can enlarge the topological band gap to 650 meV [196]. Very recently, the III–V family has been theoretically extended to include the Tl-based compounds g - TIX with $X = N$ – Sb , which are found to be thermally stable under room-temperature [197]. Topologically nontrivial phases due to the band inversion at the Γ point are found in $TIAs$ and $TISb$ [197]. This kind of s - p band inversion can also be applied to the group-V based compounds alloyed with the group-VII elements, e.g. Bi_4Br_4 [198, 199] and Bi_4F_4 [200], which, however, possess a quasi-cubic lattice structure rather than the honeycomb-lattice structure.

2.7. Functionalized honeycomb lattices of group-IV and -V elements

2.7.1. Functionalized honeycomb lattices of group-IV elements. In order to open up a larger bulk band gap and increase the tunability of the \mathbb{Z}_2 topological insulating phase in group-IV element based planar or low-buckled honeycomb systems, various schemes have been suggested. In addition to the heavy-atom adsorption scheme [30], functionalization is one of the most efficient approaches to enlarge the bulk band gap [32, 103]. This method was first reported by Ma *et al* by considering halogenated germanene [103] and then was generalized to stanene (i.e. the tin monolayer) and other honeycomb lattices [32, 196]. Here, we take the stanene (monolayer tin) as an example, which is intrinsically a Kane–Mele type TI with a topologically nontrivial band gap at the K/K' points, as shown in figure 6(a). The chemical function groups, such as $-F$, $-Cl$, $-Br$, $-I$, and $-OH$, are strongly coupled with the p_z orbitals of the stannum atoms and lift the Dirac cones at the K/K' points by a huge gap, which is the so-called ‘orbital filtering effect’.

In contrast, a band inversion can be induced between a small gapped s and $p_{x,y}$ bands leading to a parity exchange between the occupied and unoccupied bands at the time-reversal point Γ , where a large nontrivial bulk gap of about 300 meV is opened due to the strong spin–orbit coupling [32], as displayed in the lower panel of figure 6(b). Moreover,

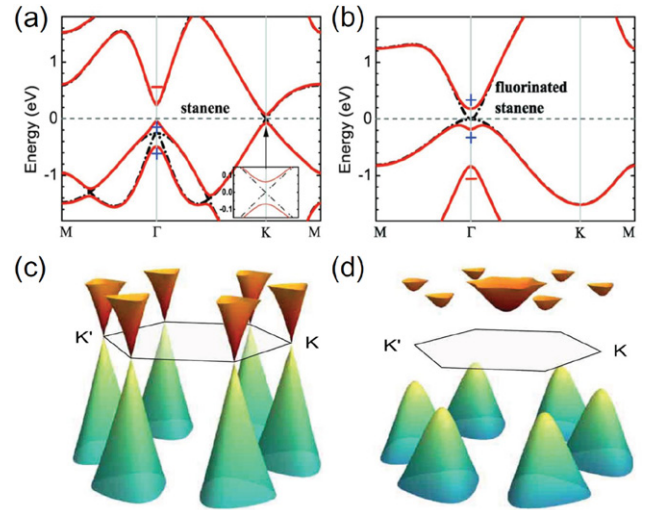


Figure 6. (a) and (b): Electronic structures of stanene and functionalized stanene. (c) and (d): Band structure of functionalized Bi bilayer without and with spin–orbit coupling, respectively. Figures (a)–(b) reprinted with permission from [32], copyright 2013 by the American Physical Society. Figures (c)–(d) reprinted with permission from [209], copyright 2015 Nature Publishing Group.

although stanene [201], i.e. the hydrogenized monolayer stanene, is a topologically trivial insulator, the hydrogenized bilayer and trilayer stanenes are found to be \mathbb{Z}_2 TIs [202]. This kind of functionalization can not only enlarge the bulk band gap but also provide extra means to control the edge modes between two topologically distinct phases of stanene, e.g. the states between fluorinated stanene and stanane. Similar results have also been reported for germanene and the 2D counterpart of lead [112, 203, 204] as well as the dumbbell stanene [205].

2.7.2. Functionalized honeycomb lattices of group-V elements.

Similar to the case of group-IV elements, functionalization of honeycomb lattice composed of group-V elements is also an effective method to induce TIs with large band gaps where the orbital-filtering effect also plays a key role. For example, the functionalized Bi-bilayers have been intensively studied with reports of large nontrivial band gaps for various functional groups (such as $-H$, $-F$, $-Cl$, $-Br$, $-I$ [180, 206–210], and $-CH_3$ [210]). However, filtering of the p_z -orbital has given different results. For the group-IV elements the functional groups lift the p_z -orbital around the KK' valleys and induce a band inversion at the Γ point, whereas for the group-V elements the functional groups couple strongly with the p_z -orbital to induce a large local gap at the Γ point, and then further flatten the buckled honeycomb-lattice structures [209] to give rise to Dirac cones at the KK' valleys, which are dominated by the $p_{x,y}$ -orbitals in the absence of spin–orbit coupling as displayed in figure 6(c) [207, 211]. Due to the non-vanishing orbital angular momentum of the states at the KK' points, the intrinsic on-site spin–orbit coupling dominates and produces an effective Kane–Mele-type spin–orbit coupling, with a strength of the same order as that of the atoms as displayed in figure 6(d). As a consequence, the topological band gap of the functionalized group-V elements is very large, for instance, the gap for the functionalized Bi bilayer can be as large as

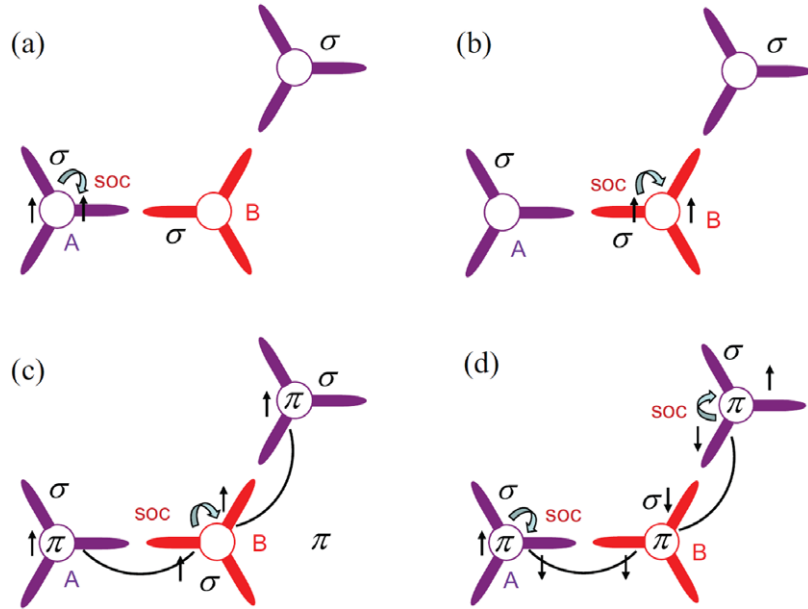


Figure 7. Origin of the Kane–Mele type spin orbit coupling. For functionalized Bi bilayer, the on-site spin orbit coupling $|A \uparrow\rangle \rightarrow |A \uparrow\rangle$ is nonzero since the orbitals are due to $p_x \pm ip_y$, which has a unit z -direction angular momentum with a sign opposite to that of the B sublattice, as shown in (a) and (b). For graphene with a p_z dominated orbital, the term is zero since the z -direction angular momentum $m = 0$, as shown in (d), where the on-site spin mixing mediated intrinsic spin–orbit coupling intensity is on the second order of atomic spin–orbit coupling. However, for a low buckled structure, the sp^3 -like hybridization induces coupling between the p_z orbital of the A sublattice with the $p_{x,y}$ orbital of B sublattice, which mediates the intrinsic spin–orbit coupling on the first order intensity of atomic spin–orbit coupling. Reprinted with permission from [207], copyright 2014 by the American Physical Society.

1 eV. Figure 7 provides a clear comparison of the different origins of the Kane–Mele-type intrinsic spin–orbit coupling for the planar honeycomb-lattice structure with the p_z -orbital (e.g. graphene), the low-buckled honeycomb-lattice structure dominated by the p_z -orbital (e.g. silicene), and the planar honeycomb lattice with $p_{x,y}$ -orbitals (e.g. functionalized Bi bilayer). Furthermore, the effect of the functional groups -H and -F has been extended from a single Bi bilayer film to 1–5 bilayers of Bi and Sb thin films, where various topological phase transitions have been demonstrated [212].

Such an orbital-filtering effect can also find application when the Bi atoms are fabricated on some suitable substrate such as a Si(1 1 1) surface covered with halogen or hydrogen atoms, where the Bi atoms can self-assemble to form a honeycomb-lattice structure with high-kinetic and high-thermodynamic stability. Similar to the effect of the functionalization on Bi bilayers, the coupling between Bi p_z -orbital and the substrate can also lift the p_z -orbital away from the Fermi level and generate the linear Dirac cones at the KK' points, where a topologically nontrivial gap can open when the spin–orbit coupling is further considered. This is known as the ‘substrate-orbital-filtering-effect’ [180–184].

2.8. Topological Anderson insulator

It is known that, for normal 2D metals, the metallic phase is unstable and becomes an Anderson insulator under any weak disorder. Interestingly, an anomalous finding appears that, in HgTe quantum wells, the disorder can drive a topological phase transition from a trivial insulator to a topologically nontrivial insulator with a quantized spin-Hall conductance

plateau [213], as illustrated in figures 8(d)–(f). Numerical calculation has shown that the quantized conducting plateau arises from the dissipationless edge states in a disordered ribbon [214]. Although the transport properties of this phase share the same characteristics as those in the \mathbb{Z}_2 TI, their disconnected regions in the phase diagram of figure 8(f) imply that this may be a new topological phase different from the \mathbb{Z}_2 TI, and so has been given the name ‘topological Anderson insulator’ [213]. Later, this insulating phase was proved to be topologically equivalent to the \mathbb{Z}_2 TI phase of HgTe/CdTe in the inverted regime since it can be obtained by continuously varying the Dirac mass, Fermi energy, and disorder strength in the three dimensional parameter space [215].

The topological phase transition from a trivial insulator to a TI is induced by the renormalization of the mass term due to the disorder via the quadratic momentum term in the low energy continuum model Hamiltonian, which can convert the mass term from positive to negative [216–219]. The quantized conductance plateau appears when the renormalized chemical potential/Fermi level lies in the band edge [216]. Although the topological Anderson insulator shares the same topological properties as a TI, they are distinct in the bulk. Specifically, in a TI, the gapless edge modes live in the bulk band gap where no bulk states are present. However, in a topological Anderson insulator, localized bulk states may occur in the mobility gap where the localized bulk states appear [220, 221]. Moreover, it is noteworthy that, when the Fermi-level is located at the valence band rather than the conduction band, there is no topological phase transition from the metallic phase to the 2D TI phase in both topological trivial and nontrivial phases, as shown in figure 8. Such an asymmetry behavior for a Fermi

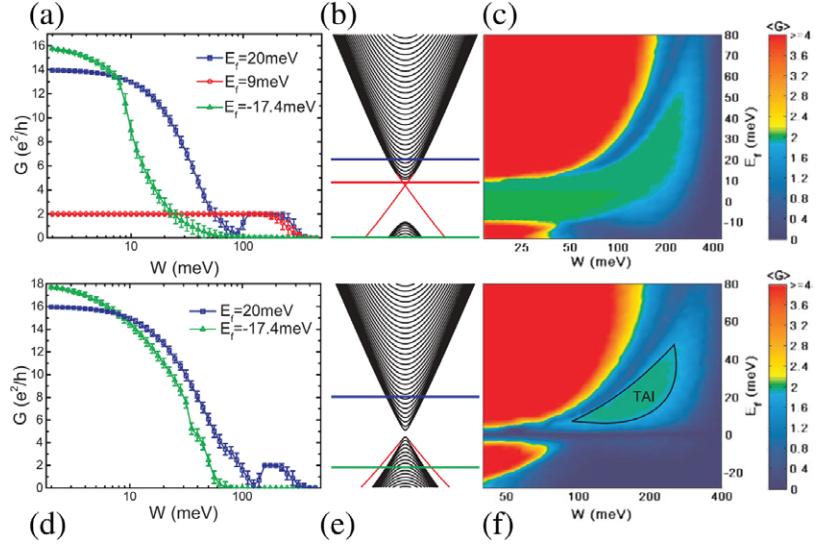


Figure 8. Conductance of disordered strips of HgTe/CdTe quantum wells for: (a)–(c) an inverted quantum well with $M = -10$ meV, and (d)–(f) a normal quantum well with $M = 1$ meV. (a) Conductance G as a function of disorder strength W at three Fermi energy values. The error bars show standard deviation of the conductance for 1000 samples. (b) Band structure calculated with the tight-binding model; its vertical scale (energy) is the same as in (c), and the horizontal lines correspond to the Fermi energy values of (a). (c) Phase diagram showing the conductance G as a function of both disorder strength W and Fermi energy E_f . Figures (d)–(f) are the same as (a)–(c), but for $M > 0$. The TAI phase regime is labeled. In all figures, the strip width L_y is set to 500 nm; the length L_x is 5000 nm in (a) and (d), and 2000 nm in (c) and (f). Reprinted with permission from [213], copyright 2009 by the American Physical Society.

level lying in the conductance and valence bands arises from the particle-hole asymmetry. In a system with particle-hole symmetry, the Anderson disorder can induce the localization of the bulk states as well as the coexisting edge states, while a conductance plateau appears only when the Fermi level lies inside the topologically nontrivial band gap [222]. Such an Anderson disorder induced topologically nontrivial phase can also be extended to a system with modified Dirac Hamiltonian by including the quadratic correction [223].

The effect of the hopping disorder has also been studied; it was found that the inter-cell hopping term can also lead to a topological Anderson insulator [224] while the intra-cell hopping cannot [225]. In the presence of Rashba spin-orbit coupling, a mediated metallic phase between different topologically trivial and nontrivial insulating phases has been theoretically reported [219, 224, 226]. Moreover, it was found that the bulk states can be effectively localized by the long-range disorder, but the edge states are much more robust [222]. Furthermore, in contrast to the Anderson disorder without spatial correlation, the finite correlation length disorder was found to be detrimental to (or even totally suppress) the formation of the topological Anderson insulator [227]. The presence of several types of disorder, Rashba spin-orbit coupling, the finite-size effect [228, 229] as well as correlation make it challenging to observe topological Anderson insulator.

2.9. Time-reversal symmetry breaking quantum spin-Hall effect

As long as the time-reversal symmetry is preserved, \mathbb{Z}_2 is a well-defined topological invariant no matter whether the spin is a good quantum number or not. For 2D systems with preserved mirror symmetry about the plane, s_z is a good quantum

number, leading to well-defined Chern numbers for each spin (i.e. \mathcal{C}_\uparrow and \mathcal{C}_\downarrow), which are intimately related to each other by the time-reversal operation $\mathcal{C}_\uparrow = -\mathcal{C}_\downarrow$. Since the unit Chern number for a spin state corresponds to one gapless spin-polarized chiral edge state, the spin-Chern number defined as $\mathcal{C}_s = (\mathcal{C}_\uparrow - \mathcal{C}_\downarrow)/2$ is fundamentally equivalent to \mathbb{Z}_2 . The only difference between \mathbb{Z}_2 and \mathcal{C}_s is that the former can only take the value of 0 or 1 while the latter can be any integer. When the mirror symmetry about the 2D plane is broken, s_z is no longer a good quantum number and thus the above-mentioned spin-Chern number no longer has a valid definition and the resulting \mathcal{C}_s is no longer exactly quantized. Nevertheless, the spin-Chern number can still be meaningful through an alternative definition, which is shown to be equivalent to the \mathbb{Z}_2 topological order whenever the time-reversal symmetry is preserved [97].

However, when time-reversal symmetry breaks down, e.g. when the spontaneous anti-ferromagnetic order in a graphene nanoribbon is taken into account [230, 231], the QSHE may also exist with a well-defined spin-Chern number [232–234]. Strictly speaking, this is not a topological phase since the Kramers degeneracy of the chiral edge states is lifted, signifying that the edge modes are no longer topologically protected from the elastic back-scattering by time-reversal symmetry [232]. Although the backscattering is possible, the corresponding edge states can still give rise to a nearly quantized spin-Hall conductance and are quite robust against weak disorders due to the strong localization at their boundaries. Therefore, similar to \mathbb{Z}_2 TIs, they are still good candidates for practical applications [232]. Additionally, time-reversal symmetry breaking QSHE have also been reported in monolayer graphene [233, 234] and ferromagnetic metals in the presence of strong magnetic fields [235–237], but these are beyond the

scope of this review since we focus here on the topological phases without an applied external magnetic field.

3. Quantum anomalous Hall effect (QAHE)

In the presence of time-reversal symmetry, insulators can be classified into \mathbb{Z}_2 TIs and topologically trivial band insulators according to the \mathbb{Z}_2 topological invariant, as described above. In section 1 we saw that for insulators with broken time-reversal symmetry, their topological properties are usually characterized by the first Chern number C [4, 5], which indicates a topologically trivial insulator when $C = 0$, and topologically nontrivial quantum Hall effects [3] and QAHE for a nonzero integer C [9]. Here, the Chern number is closely related to the number of gapless chiral edge modes that emerge inside the bulk band gap of a finite-sized ribbon according to the ‘bulk-edge correspondence’ [7]. Due to their one-way chiral propagation characteristic, these edge modes are robust against nonmagnetic, magnetic, short-range, long-range or any other kind of weak disorder [223]. This is inherently superior to the spin-helical edge modes in \mathbb{Z}_2 TIs where backscattering is allowed by disorder that break time-reversal symmetry.

After the initial prediction of the QAHE, there was only little progress before the year 2004 [11]. However, interest has been revived by the successful experiments on TIs and 2D atomic crystal layers, and in particular by two independent theoretical proposals in 2010 to realize the effect based on magnetic 3D TI thin films [40] and graphene [46]. Even though these two schemes employ independent semiconductor and Dirac semi-metal materials, they are both based on the perpendicular ferromagnetic order and spin-orbit coupling that were the pioneer ideas involving semiconductor quantum wells and atomic crystal layers, as mentioned above in sections 3.1 and 3.2, respectively. The above proposals based on a perpendicular Zeeman field and spin-orbit coupling with small Chern numbers can be regarded as the dominating ‘conventional’ QAHE structure. Recently, two new groups have been introduced into the ‘conventional’ family, i.e. the heterostructure quantum well which will be reviewed in section 3.3 (heterostructures of ferromagnetic insulator films and other insulating thin films with strong spin-orbit coupling), and the transition metal oxide to be reviewed in section 3.4. In contrast, we shall also describe some ‘unconventional’ properties of the QAHE, e.g. a large Chern number corresponding to large anomalous Hall conductance (section 3.5), a system with in-plane ferromagnetism (section 3.6) or anti-ferromagnetic order (section 3.7), and quantized Hall conductance produced by edge-engineering of a finite size sample (section 3.8).

3.1. Magnetic doping in quantum well-based 2D-TIs and 3D-TI thin films

3.1.1. Quantum well-based 2D-TIs. The unique transport characteristic of 2D-TIs is the emergence of time-reversal symmetry protected spin-helical edge modes propagating along each boundary, which is actually a combination of two identical QAHE structures with exactly opposite spins. When

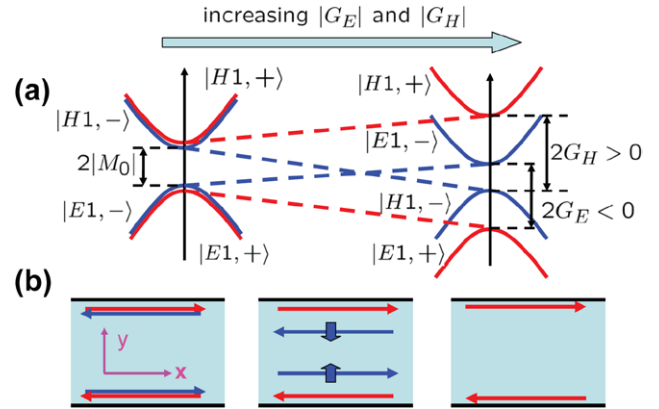


Figure 9. Evolution of band structure and edge states upon increasing the spin splitting. For (a) $G_E < 0$ and $G_H > 0$, the spin down states $|E1, -\rangle$ and $|H1, -\rangle$ in the same Hamiltonian block touch each other and then enter the normal regime. (b) Behaviour of the edge states during level crossing in the case of (a). Reprinted with permission from [238], copyright 2008 by the American Physical Society.

one of the structures is eliminated, the QAHE is obtained. The first example was the Mn-doped HgTe quantum well [35]. When ferromagnetism is introduced by doping magnetic atoms (e.g. Mn), the two-fold Kramers degeneracy of the conduction and valence bands is lifted. However, mixing of the spin angular momentum and orbital angular momentum makes the two QAHE structures respond differently to the Zeeman field from the magnetic order, i.e. the band gap of one model widens while that of the other closes and reopens to undergo a phase transition to become a trivial insulator [238]. As a consequence, the QAHE is formed as half of the TI, as displayed in figure 9(a). However, it has been shown that the ferromagnetic order is not favorable in such a system, making it unrealistic experimentally [239]. Within the same framework, it was later found that the ferromagnetism can be formed in magnetically doped InAs/GaSb quantum wells via enhanced Van Vleck paramagnetism from the strong interband coupling [239]; this has boosted hopes to realize the QAHE in quantum well-based 2D-TIs. Alternative methods have also been proposed for magnetically doped 2D-TIs within junction quantum wells [123].

3.1.2. 3D-TI thin films. The discovery of 3D \mathbb{Z}_2 TIs soon motivated the further exploration of QAHE in 3D-TI thin films through the establishment of stable ferromagnetism, e.g. by doping Cr/Fe-atoms in a Bi_2Se_3 thin film host material [40]. Inspired by this finding, Chang *et al* finally observed the effect for the first time in Cr-doped $(\text{Sb}, \text{Bi})_2\text{Te}_3$ in experiment [41]. Subsequently, several other experimental groups independently reported observation in the same host material of $(\text{Sb}, \text{Bi})_2\text{Te}_3$ but at an extremely low temperature (lower than 100 mK). Below, we shall briefly describe how the QAHE is formed in a magnetic 3D TI thin film.

Let us take Bi_2Se_3 as an example [36, 38, 40, 240–242]. Similar to the 1D gapless edge modes of 2D-TIs, 2D gapless surface modes can be generated on the surface of 3D-TI thin films, where the spins are locked with the momenta preserving

the time-reversal invariance [36, 38]. Due to this spin-momentum locking, the elastic backscattering is completely suppressed when the 3D-TI thin film is thick enough to avoid direct coupling between the top and bottom surface states. When the film thickness is decreased, the coupling between top and bottom surface states results in a band gap at the Dirac cone of the surface states, forming a 2D insulator [40] as shown in figure 10.

One intriguing property of this bulk 3D-TI is that the Bi_2Se_3 conduction and valence bands of arise from the bonding and anti-bonding p orbitals, which is different from ordinary semiconductors where the contributions to the conduction and valence bands come mainly from the s and p orbitals, respectively. This feature greatly enhances the spin susceptibility via the Van Vleck paramagnetism. Moreover, the strong spin-orbit coupling induced band inversion further strengthens the spin susceptibility in an anisotropic manner [40, 243]. As a result, the magnetic doping prefers to form a spontaneous ferromagnetic order, aligning along the off-plane direction [40]. Once the ferromagnetic order is established, the ferromagnetism splits the spin-degenerate and insulating bands from the coupled top and bottom surface states in the 3D-TI thin films. When band inversion occurs due to the spin splitting, the spin-orbit coupling reopens a band gap to induce a topological phase transition from a trivial insulator to quantum anomalous Hall insulator with a Chern number of $C = 1$ [40] (see figure 10). Such a delicate and precise theoretical prediction was later experimentally realized in Cr-doped $(\text{Bi},\text{Sb})_2\text{Te}_3$ [41–43, 244–246] and V-doped $(\text{Bi},\text{Sb})_2\text{Te}_3$ [44]. There are also similar proposals for other 3D-TI thin films, e.g. Cr-doped TlBiTe_2 and TlBiSe_2 films [247]. In addition, a similar band inversion can also be formed in magnetically-doped 2D topological crystalline insulator thin films [60], where the spin-orbit coupling induced band gap carries a Chern number of $C = 2$ rather than $C = 1$ [248–250].

Despite the fact that QAHE was experimentally observed in Cr- or V-doped $(\text{Bi},\text{Sb})_2\text{Te}_3$, all these experiments were performed only at extremely low temperatures, which would still prohibit potential applications of this fundamental quantum transport phenomenon. To realize the high-temperature QAHE, a charge compensated $n-p$ codoping method is theoretically proposed [251]. The first-principles' calculations show that the thin film band gap of V-I codoped Sb_2Te_3 can reach as large as 84 meV at very low codoping concentration. At the same time, the resulting ferromagnetic Curie temperature is estimated to be at a lower bound of 50 K, which is also the lower bound of the QAHE observation temperature. This is about three orders of magnitude higher than the typical temperatures experimentally reported so far.

3.2. Graphene and other honeycomb-lattice materials

3.2.1. Monolayer graphene. As mentioned in section 2.1 above, the band crossover of graphene, i.e. the linearly dispersed Dirac points K and K' shown in figure 11(a), originates from the sublattice/chiral symmetry. Therefore, in order to open a band gap at the Dirac points, this symmetry must be broken, for example by applying staggered AB sublattice potentials [52] or by incorporating the intrinsic spin-orbit

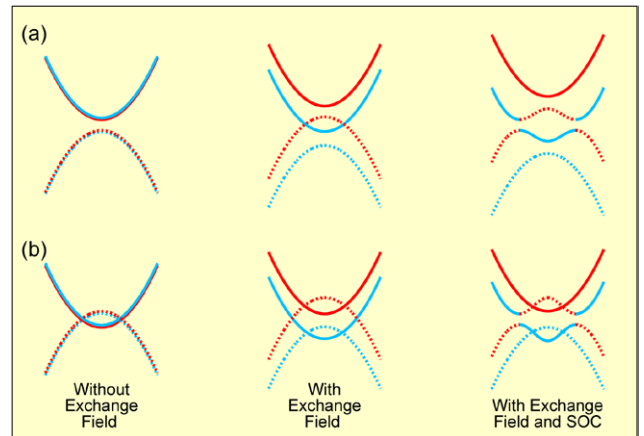


Figure 10. Evolution of the subband structure upon increasing the exchange field. Solid (dashed) lines denote the subbands that have even (odd) parity at the G point. The blue (red) color denotes the spin down (up) electrons. (A) The initial subbands are not inverted. When the exchange field is strong enough, a pair of inverted subbands appears (red dashed line and blue solid line). (B) The initial subbands are already inverted. The exchange field causes band inversion in one pair of subbands (red solid line and blue dashed line) and increases the inversion in the other pair (red dashed line and blue solid line). Reprinted with permission from [40].

coupling from spin-dependent next-nearest neighbor hopping [23]. However, the extrinsic Rashba spin-orbit coupling from spin-dependent nearest-neighbor hopping does not break the chiral symmetry but instead induces spin-mixing and lifts the four-fold degeneracy at the Dirac points. We see in figure 11(c) that the spin-degenerate linear dispersions around K and K' become quadratic band crossings where the up and down spins become mixed, which allows the band gap to open by applying a perpendicular Zeeman field, as shown in figure 11(d). Such a picture is closely related to the chirality of graphene's band structure. Various topologically nontrivial phases, such as \mathbb{Z}_2 TIs [23], QVHE [52] and QAHE [46], can be produced by breaking the sublattice/chiral symmetry.

On the other hand, graphene can also be regarded as a zero-gap semiconductor. When a perpendicular Zeeman field is applied, spin-splitting occurs to form crossing points between the spin-up and spin-down bands with the spin being a good quantum number (see figure 11(b)). The accidental degeneracy at the crossing points can be easily lifted by spin-mixing perturbation, e.g. Rashba spin-orbit coupling, as shown in figure 11(d) [46, 252]. Different from the understanding based on chiral symmetry, such a simple physical picture can be generally extended to other (quasi)-2D zero-gap or narrow-gap semiconductors, where a sufficiently large Zeeman field is required to induce crossing between the spin-up and -down bands by overcoming the bulk band gap. Moreover, the spin-mixing spin-orbit coupling is not merely limited to the Rashba type, for example, spin-orbit coupling in Bi_2Se_3 thin film may also result from bulk inversion-asymmetry [40].

In brief, the above explanation of graphene-based QA Hall effects from two distinct viewpoints can be regarded as two different limits since the effect is a joint consequence of the Rashba spin-orbit coupling and Zeeman field influence [253]. The first one corresponds to the large Rashba spin-orbit

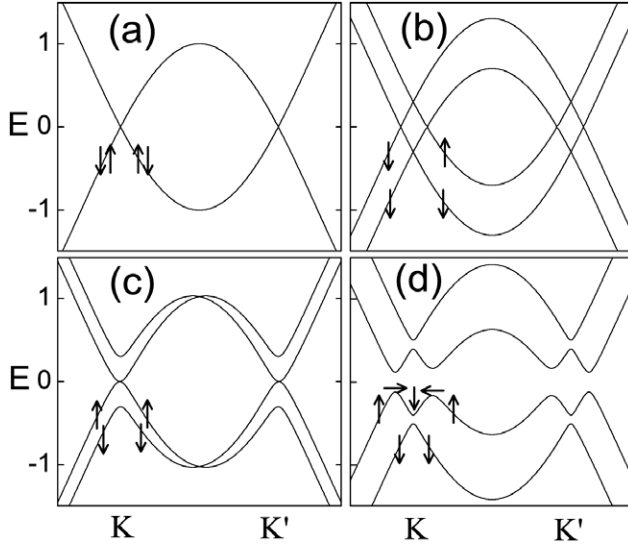


Figure 11. Evolution of band structures of bulk graphene along the profile of $k_y = 0$; arrows represent the spin directions. (a) Pristine graphene: spin-up and spin-down states are degenerate; (b) When only a Zeeman field is applied, the spin-up/spin-down bands are upward/downward lifted with the four bands crossing near the K and K' points; (c) When only Rashba spin–orbit coupling is present, the spin-up and -down states are mixed around the band crossing points; (d) When both Zeeman field and Rashba spin–orbit coupling are present, a bulk gap is opened and all four bands become non-degenerate. Reprinted with permission from [46], copyright 2010 by the American Physical Society.

coupling limit, where the four-band low-energy continuum model Hamiltonian at the K or K' valley is effectively reduced to a two-band extended Haldane model (the detailed formula are presented in [253]). The second corresponds to the large Zeeman field limit, where the QA Hall effect can be regarded as a consequence of the topological charges carried by skyrmions from the real-spin textures and merons from the AB sub-lattice pseudospin textures [253]. Since the merons from the lower two valence bands cancel each other, each valley carries a skyrmion and thus the total Chern number is $C = 2$, with equivalent contributions from both valleys, i.e. $C_K = C_{K'} = 1$. The equivalent contributions can be further understood from the Berry curvature, which is an analogy of the magnetic field in momentum space, as illustrated in figure 12 where the Berry curvatures are peaked at the corners of the first Brillouin zone and have the same signs at the inequivalent valleys with $\Omega(\mathbf{k}) = \Omega(-\mathbf{k})$. In analogy to the formation of the QAHE in graphene with Dirac dispersion, similar proposals employing the joint effect of the Zeeman field and Rashba spin–orbit coupling have also been presented for Kagomé [254], checkerboard [255], star [256], and square lattices [257].

3.2.2. Experimental graphene-based QAHE prototypes. It is noteworthy that both ferromagnetism and Rashba spin–orbit coupling do not exist in pristine graphene. Therefore, external means are required to induce these two effects. The most effective way is to adsorb magnetic $3d$ transition-metal atoms on one side of a graphene sheet [47, 258]. For example, due to the magnetic proximity effect, graphene can be easily magnetized by the magnetic adatoms. Moreover, the charge

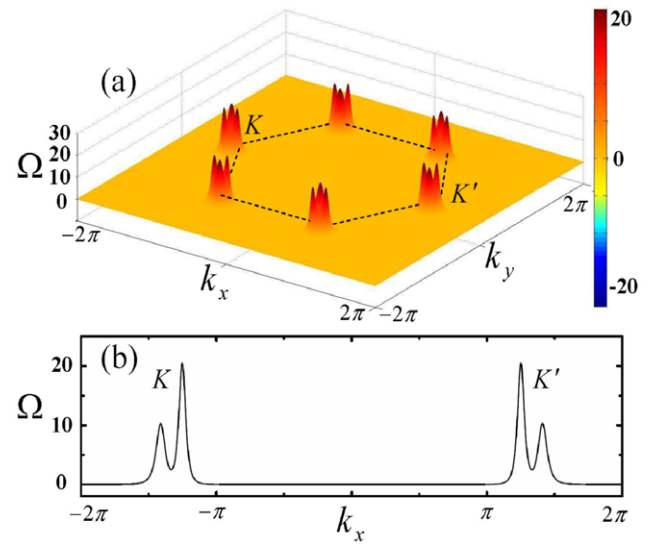


Figure 12. (a) Berry curvature distribution Ω (in units of e^2/h) of the valence bands in momentum space. The first Brillouin zone is outlined by the dashed lines, and two inequivalent valleys are labeled as K and K' . (b) Profile of Berry curvature distribution along $k_y = 0$. Reprinted with permission from [46], copyright 2010 by the American Physical Society.

transfer between graphene and the adatoms induces a charge redistribution in a very short distance (around 1.5 \AA), which can generate a considerable electric field and result in a sizeable Rashba spin–orbit coupling by breaking the mirror symmetry about the graphene plane. In addition to $3d$ -adatoms, it is found that some $4d$ - and $5d$ -transition metal adatoms can also form ferromagnetic orders in graphene superlattices, e.g. Ru and W adatoms [48, 137, 259]. In particular, for graphene with Ru adatoms, the QAHE with different Chern numbers can be obtained by adsorbing atoms in different supercells [137, 259].

One of the important factors that may negatively influence the realization of QAHE is the possible existence of inter-valley scattering in 3×3 or $\sqrt{3} \times \sqrt{3}$ graphene supercells that couple the K and K' valleys by folding them into the Γ point, which can open a sizeable trivial band gap in the hollow-adsorption case [253], or form a quadratic band crossover in the top-adsorption case [260]. In [132], Jiang *et al* employed a finite-size scaling method to show that the inter-valley coupling vanishes in a real sample with the adatoms being distributed in a completely random manner. Figure 13 displays the two-terminal averaged conductance as a function of the Fermi level in the presence of periodic-adsorption (i.e. one hollow-site adsorption in a 3×3 graphene supercell) and random adsorption with the same adsorption coverage, where the QAHE competes with the inter-valley scattering. We can see that in the periodic case there is an energy range with zero conductance $\langle G \rangle = 0$, which corresponds to a trivial band gap (see figure 13(a)), while when the adatoms become randomly distributed, a plateau of $\langle G \rangle = 2e^2/h$ without fluctuation appears, indicating the formation of a QAHE band gap (see figure 13(b)). This suggests that in a realistic sample with totally random distribution of the adatoms the inter-valley coupling will become vanishing but the real-spin

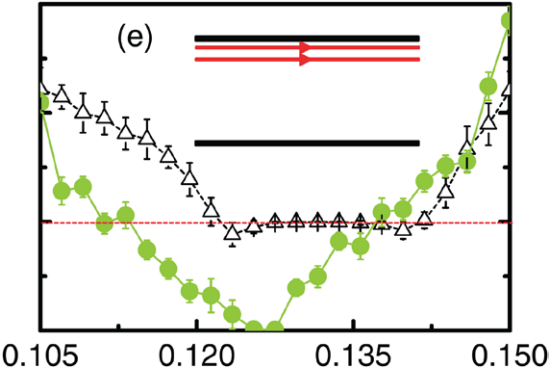


Figure 13. Conductances G of a two-terminal setup in the presence of periodically and randomly distributed adatoms as a function of Fermi level ε_F . Green solid line with solid circles: the case with periodic adsorption where an insulating regime occurs. Dashed black line with hollow triangles: the case of randomly distributed adatoms where the conductance shows a quantized plateau in some regime. Reprinted with permission from [132], copyright 2012 by the American Physical Society.

related effects (e.g. magnetism and spin–orbit coupling) are not affected [132].

It therefore seems that the QAHE should be easily realizable in graphene by randomly adsorbing some magnetic atoms. However, both later experiments and theories found that the adatoms in graphene cannot stabilize a dilute distribution but prefer to form clusters [258, 261], which is detrimental for QAHE generation. Within the same physical scheme, another promising method is to consider proximity-coupling with a ferromagnetic insulating substrate. For example, in [49], graphene is coupled with the (1 1 1)-ferromagnetic plane of the anti-ferromagnetic insulator BiFeO_3 , which is shown to be able to open a band gap larger than 1 meV. Such a limited band gap originates from the extremely weak Rashba spin–orbit coupling since the van der Waals interaction between graphene and the substrate is weak due to their large separation of about 3 Å. Thus the band gap can be further enlarged by applying an external stress to a certain degree. Another similar theoretical proposal is to place graphene on top of the (0 0 1) surface of RbMnCl_3 , with a band gap in the order of 1–10 meV [262]. It is noticeable that, although so far the QAHE has not yet been experimentally observed in graphene, considerable progress has been made, i.e. intrinsic ferromagnetism has been measured in graphene placed on top of LaMnO_3 , and a large anomalous Hall conductance of $\sigma_{xy} \sim 0.2e^2/h$ has been reported in a ferromagnetic insulating YIG thin film [50], which is rather close to the final quantization observation because a finite Hall conductance only exists in a much narrower energy range [49].

From the above analysis, it is reasonable to expect that, to realize the QAHE in graphene at a higher temperature (e.g. by engineering a large band gap), the most effective approach is still to dope magnetic atoms but not to use magnetic insulators. Fortunately, it has been shown that compensated $n-p$ codoping can be used to form long-range ferromagnetism in graphene by simultaneously codoping Ni and B atoms [263]. This provides a valuable and practical route via magnetic doping. Moreover, ferromagnetic order can also be induced in

nano-meshed graphene, where the p_{xy} orbitals dominate the conducting electrons [264].

3.2.3. Low-buckled honeycomb-lattice systems of group-IV elements. The formation mechanism of the QAHE from the Zeeman field and Rashba spin–orbit coupling in graphene can also be applied to low-buckled honeycomb lattice systems, for example silicene, which is a single layer of silicon. The major difference between low-buckled systems and planar graphene is the generation of an intrinsic Rashba-type spin–orbit coupling which makes the extrinsic Rashba unnecessary for generating the QAHE. Since the intrinsic Rashba spin–orbit coupling is momentum-dependent and vanishes at the Dirac points K and K' , compared with the linearly dispersed edge states in graphene the nearly flat-band edge states are present in the absence of any extrinsic Rashba effect [265].

Although both the intrinsic and the extrinsic Rashba spin–orbit couplings can give rise to the QAHE with a Chern number of $C = 2$ in the presence of a Zeeman field, their competition results in a new topological phase, i.e. a valley-polarized QAHE phase with a Chern number of $C = 1$ that originates from only one valley [266]. This can be understood as an intermediate topological phase that occurs between the transition from the intrinsic to the extrinsic Rashba spin–orbit coupling induced QAHE phases [266, 267]. Similar effects have also been proposed for bilayer silicene [267]. It is notable that the low-buckled structure or the top-bottom degree of freedom makes it possible to tune the band structure through applying an external electric field to induce a rich range of topological phases [265, 267]. Although the Rashba spin–orbit coupling intrinsically exists in low-buckled systems, the Zeeman field has to be induced by some external means, such as $3d$ and $4d$ magnetic atom decoration [268–271]. Another most interesting topological phase is the QSHE-QAHE, wherein the chiral edge states are present in one valley while the spin-helical edge states appear in another valley through introduction of the sublattice-dependent Zeeman field [348].

3.2.4. Buckled honeycomb-lattice system of group-V elements. Different from the Dirac semi-metal honeycomb lattices composed of group IV elements where the low-energy physics is determined by the half-filled π band Dirac dispersions, in a honeycomb lattice $\text{Bi}(1 1 1)$ bilayer the fully filled valence bands create an insulator where the p_z -dominated conduction band and the p_{xy} -dominated valence band edges possess odd and even parities, respectively, at the Γ point [172]. The strong spin–orbit coupling can then induce inversion between the bands of opposite parities, and so generate a \mathbb{Z}_2 TI. When a small Zeeman field is introduced, a time-reversal symmetry breaking QS Hall effect results, characterized by a quantized spin-Chern number and spin-polarized edge states. Moreover, the presence of the Zeeman field also lifts the spin degeneracy of both the conduction and valence bands, shrinking the topological band gap.

When the Zeeman field is further increased, the band gap gradually closes and reopens, leading to a topological phase transition from a time-reversal symmetry breaking QSHE to one with a Chern number of $C = -2$, where M is the Zeeman

field [272, 273]. This is different from the band inversion induced effect with a Chern number of $C = \text{sgn}(M)$ from an ordinary insulator [40, 273]. The strong spin-orbit coupling plays a crucial role in driving the topological phase transition, i.e. the system evolves from a QAHE phase with a Chern number of $C = 1$ to one with $C = -2$ mediated by a metallic phase with the lowest filled bands contributing a Chern number of $C = 2$ [273]. So far, although the density-functional calculation has confirmed the existence of such a topological phase transition, the underlying reason why a single band inversion can induce various Chern numbers is still an open issue.

3.2.5. Half-functionalized honeycomb-lattice systems of group-IV and -V elements. In addition to doping magnetic atoms, spontaneous ferromagnetic order can also be induced by functionalization [274, 275]. Let us first take stanene as an example. Different from the full functionalization that can result in a large gap TI in stanene, the half-I-passivated stanene can establish a spontaneous ferromagnetic order due to the dangling bonds at one side [275]. Interestingly, because of the coupling between the functional group and the p_z -orbital of the tin atoms, the graphene-like Dirac bands at the K and K' points are pushed to high energy, whereas the s - p -hybridized bands at the Γ point become low-energy bands. In the absence of spin-orbit coupling, the ferromagnetism leads to asymmetry between the spin-up and -down bands, where the s - p_{xy} band inversion for the spin-up bands disappears while that for the spin-down bands appears. Therefore, when the spin-orbit coupling is included, it only opens a gap between the spin-down bands at the Γ point, which forms a QAHE phase with a Chern number of $C = 1$. It has been reported that the strong spin-orbit coupling can open a large band gap of about 340 meV, which is a good candidate for the realization of a room-temperature QAHE structure [275]. Similar results have also been proposed for half-I-passivated germanene yet with a much smaller band gap of about 60 meV [275]. This kind of half functionalization at one side is geometrically equivalent to the case with stanene being placed on top of certain substrates, such as CdTe and InSb (1 1 1) surface [275]. In fractional functionalized silicene and germanene, QA Hall effects with a Chern number of $C = -1$ or 2 have also been predicted [274].

Similar to stanene, although the fully functionalized Bi(1 1 1) bilayer is shown to be a \mathbb{Z}_2 TI, the time-reversal symmetry is broken due to the formation of a spontaneous ferromagnetic order in the half-hydrogenated Bi(1 1 1) bilayer [206, 276] or Bi(HN) bilayer, with one side being hydrogenated and the other side decorated by nitrogen atoms [209]. The induced ferromagnetism together with the strong spin-orbit coupling gives rise to a large gap QAHE with a Chern number of $C = 1$, which originates from the inversion symmetry breaking, giving different responses at the K and K' valleys. As a consequence, band inversion occurs only at one valley to produce a valley-polarized QAHE [206, 209, 276].

3.2.6. Artificial honeycomb-lattice systems. The recent development of artificial lattices in optical lattice with ultracold atoms, photonic crystals, phononic crystals and so forth

provides alternative platforms to study topological phases in media besides condensed matter [153]. Through introducing Berry curvature that resembles the alternating magnetic field [277], Haldane's model is theoretically shown to be realizable in honeycomb optical lattices with s -orbital [278]. Alternative methods to realize QAHE have been theoretically proposed in honeycomb optical lattice of ultracold atoms with $p_{x,y}$ orbitals [279] and square lattices [280]. Experimentally, the honeycomb optical lattice has been created possessing tunable Dirac points. This provides an ideal platform to study various types of topological phases [156] as well as systems with strong interactions [281–283]. By introducing appropriate Berry curvature via applying a constant force to the atoms in such a honeycomb lattice, the QAHE based on Haldane's model has been experimentally realized in two years [157]. By combining two copies of QAHE, the realization of the \mathbb{Z}_2 TI is possible in the artificial honeycomb lattice systems constructed by cold atoms [284, 285].

In addition to the s - and p -orbital-dominated bands, a d -orbital based QAHE has been predicted in an artificial structure composed of heavy transition metal atoms, e.g. W grown in a 1/3 monolayer of halogen-Si(1 1 1) that constitute a honeycomb lattice structure. The splitting of the s - and d -orbitals of W atoms due to the crystal field results in a spontaneous ferromagnetic order. This ferromagnetism and the strong spin-orbit coupling of the heavy metal atoms combine together to open up a large band gap of about 100 meV to create a QAHE structure with a Chern number of $C = -1$. Such a complex structure is expected to be achievable based on current state-of-the-art technology [286].

In addition to the above inorganic materials, honeycomb lattices can also be artificially constructed by using organic molecules (e.g. triphenyl) and magnetic Mn atoms in a specific manner, which is theoretically shown to be able to realize the Kane-Mele QSHE when the time-reversal symmetry is preserved [287]. The magnetic Mn atoms can induce an extremely large intrinsic ferromagnetism, which can completely separate the spin-up and -down bands. In contrast to the Rashba spin-orbit coupling induced gap at the crossing points of the spin-up and spin-down bands, the intrinsic spin-orbit coupling of the planar artificial honeycomb lattice gives rise to a fully spin-polarized QAHE system (or ‘half’ Kane-Mele type TI).

3.3. Heterostructure quantum wells

Since the intrinsic ferromagnetism and spin-orbit coupling are two essential ingredients for realizing the QAHE, another possible route is to directly include these two factors in a heterostructure composed of a heavy atom insulator and a ferromagnetic insulator. For example, Garrity and Vanderbilt proposed doping heavy metal atoms in magnetically ordered MnTe, MnSe, or EuS surfaces [288]. When the bands of the heavy atomic layer exhibit a gap that is located inside the large band gap of the magnetic insulator, the QAHE can in principle appear. Following this recipe, they predicted several such systems with large band gaps or large Chern numbers up to $C = 3$ by employing first-principles calculations. However, in these

systems the requirement of periodic adsorption is currently beyond possibility of experimental realization.

Similarly, a heterostructure quantum well composed of CdO/EuO (both oxides have the rocksalt structure) provides another potential platform to realize QAHE. Here, EuO is a ferromagnetic semiconductor with a valence band mainly produced by the spin-polarized f -orbital of Eu while the conduction band is dominated by the s -orbital of Cd. In the presence of a suitable in-plane strain or an out-of-plane electric field, the strong spin-orbit coupling may lead to a band inversion between the conduction band of even parity and the valence band of odd parity, which can open up a bulk band gap to host the QAHE [289]. It is noteworthy that the time-reversal symmetry is broken by the spontaneous ferromagnetic order of EuO but not the magnetic doping that is used in InAs/GaSb quantum wells or 3D-TI thin films.

Comparable to the oxide heterostructure, a bilayer system composed of GdN and EuO (both topologically trivial ferromagnetic insulators) provides another possible scheme to realize the QAHE. The strong spin-orbit coupling of Gd and the spin-polarized conduction band minima from the d -orbital as well as the smaller lattice mismatch make this system a good candidate for the QAHE with a large band gap. Moreover, a bilayer of ferromagnetic insulators such as Cr-doped $(\text{Bi},\text{Sb})_2\text{Te}_3$ and GdI_2 has proved to be another possible candidate [290]. In addition to the magnetic doping, the ferromagnetism can also be engineered through the proximity effect with the magnetic substrates [291].

Additionally, another route is to start from the 3D Chern semi-metals, where the gapless dispersion at the Fermi point is determined by the band inversion from the spin-orbit coupling, as in CdO/EuO superlattices [289] and HgCr_2Se_4 [292]. In its corresponding thin film form, the characteristics of both the ferromagnetism and the spin-orbit coupling induced band inversion will still persist to harbour the QAHE. Interestingly, tuning the thickness may be an efficient way to produce a large Chern number (see section 3.5).

3.4. Transition metal oxides

So far, although the ferromagnetic order relies mainly on the presence of transition metal atoms, the host materials are based on the group-III, -IV, -V, and -VI elements or compounds with negligible electron-electron correlations. Recently, the search for topological materials, in part stimulated by experimental progress [293], has begun to target the transition metal oxides where the electron-electron correlation and strong spin-orbit coupling (especially the $5d$ transition metal atoms with large atomic number) have led to some interesting discoveries [294–296]. Based on iridium oxide, two theoretical predictions of the QAHE in $(\text{SrIr}/\text{TiO}_3)_n$ with $n = 1$ or 2 [295] and the monolayer $\text{La}_2\text{MnIrO}_6$ [296] have been reported. Different from the honeycomb lattices of graphene-like materials, these thin films possess square lattices, i.e. orthorhombic [295] or double perovskite [296] structures where the t_{2g} -orbitals dominate the low-energy physics around the Fermi level due to the crystal fields. In the orthorhombic case, the strong spin-orbit

coupling splits the t_{2g} -orbitals into $J_{\text{eff}} = 1/2$ and $J_{\text{eff}} = 3/2$, where the spin is already combined with the orbital motions. In the case of a single IO_2 layer with $n = 1$, the specific glide symmetry leads to the Dirac dispersion at the X and Y points in the Brillouin zone, which are the two time-reversal invariant momentum points. The TI phase can be formed when an external strain is applied to break the glide symmetry and open a band gap at the Dirac points. When the Zeeman field is further included to close and reopen the band gap at the X point without affecting the bands near the Y point, the QAHE with a Chern number of $\mathcal{C} = 1$ appears.

Interestingly, in stacked bilayers, the inter-layer coupling drives the glide symmetry-protected Dirac cones away from the X and Y points. In this case, any kind of magnetism can open a band gap to host the QAHE phase with a Chern number of $\mathcal{C} = 2$ [295]. Different from SrIrO_3 , the orbitals dominating the low-energy physics in the monolayer $\text{La}_2\text{MnIrO}_6$ come from the t_{2g} -orbitals of the $3d$ -Mn atoms, whose inter-site hopping induced strong spin-orbit coupling opens a gap of about 26 meV when the Mn atoms establish a ferromagnetic order [296]. Apart from the $5d$ -atom oxides, the QAHE has also been predicted in the oxidation of the $3d$ -Cr element, i.e. $\text{CrO}_2/\text{TiO}_2$, where a smaller band gap of about 3 meV is induced due to the weak on-site spin-orbit coupling [297].

3.5. Large-Chern-number QAHE

The Chern numbers of any QAHE systems described in the previous sections are mainly limited to $\mathcal{C} = \pm 1$ and $\mathcal{C} = \pm 2$. Since the conductance in the Landau-level induced quantum Hall effect can be modified to have various integer values by changing the magnetic field or varying the Fermi levels, the possibility to obtain large-tunable large-Chern numbers that could provide strong currents and thus strong signals is of great interest from both the theoretical and practical aspects [298, 299].

In Bernal-stacked bilayer graphene, a Chern number of $\mathcal{C} = 4$ is predicted in the presence of the Zeeman field and Rashba spin-orbit coupling [119, 300], where each valley contributes a Chern number of $\mathcal{C} = 2$. Therefore, larger Chern numbers can be expected in Bernal-stacked multi-layer graphene. A large-Chern-number QAHE phase has also been reported in the graphene-like system β -graphyne where the carbon atom triple bond is inserted into graphene [301]. In such a system, the competition between the intrinsic and extrinsic Rashba spin-orbit couplings in this specific lattice structure allows us to tune the number and position of the Dirac cones. When the time-reversal invariance is broken, the resulting band structure can exhibit various QAHE phases with different Chern numbers ranging from $\mathcal{C} = -3$ to $\mathcal{C} = 3$ [301].

Additionally, large Chern numbers have also been predicted in magnetic 3D-TI thin films beyond the 2D limit [298, 299]. Within the 2D limit, the QAHE arises from the direct coupling between the top and bottom surface states which gives rise to the lowest Chern number of $\mathcal{C} = 1$ [40]. When the films are thicker, the conduction and valence subbands

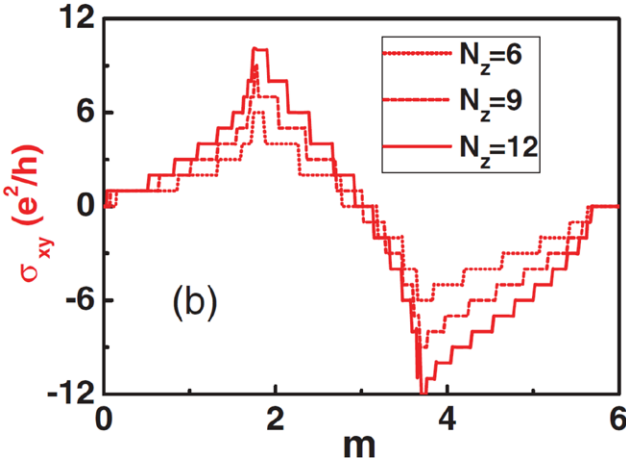


Figure 14. Hall conductance versus Zeeman field m , for sample thicknesses of $N_z = 6, 9$ and 12 . Reprinted with permission from [298], copyright 2012 by the American Physical Society.

due to the confinement along the z -direction become involved in the band inversion due to the Zeeman field and spin–orbit coupling. The Chern number is therefore strongly dependent on the relative magnitude of the Zeeman field to the sample thickness, which determines the separation between the subbands. As illustrated in figure 14, for different sample thicknesses, increasing the Zeeman field can increase the Chern number to a rather large integer, which is different from the ordinary quantum Hall effect where increasing the magnetic field decreases the Hall conductance [298, 299]. The recent experimental observation of the QAHE in $(\text{Cr}_{0.12}\text{Bi}_{0.26}\text{Sb}_{0.62})_2\text{Te}_3$ samples demonstrates the possibility of realizing such large Chern numbers [43]. In these systems, the nearly quantized Hall conductance was observed in a sample with a thickness of over 10 quintuple layers, which is beyond the 2D hybridization thickness [43].

3.6. In-plane magnetization induced QAHE

In addition to the out-of-plane Zeeman field, the in-plane field can also induce the QAHE [302–304]. In a 2D system, the presence of mirror reflection symmetry, i.e. symmetry under $M_x : (x, y) \rightarrow (-x, y)$, constrains the Hall conductance σ_{xy} to be zero since this symmetry requires the same current along both the x and $-x$ directions. Different from the out-of-plane Zeeman field which is a pseudoscalar, i.e. a scalar that changes sign under parity inversion and thus breaks any in-plane reflection symmetry, the in-plane Zeeman field is a pseudovector and does not break all the reflection symmetries; for example, the M_x reflection symmetry is preserved when the field is applied along the x -direction. Therefore, the in-plane field can only induce a QAHE when the remaining mirror-reflection symmetry is broken [304], as in a patterned 2D electron gas with both Rashba and Dresselhaus spin–orbit couplings [302], or in magnetically-doped Bi_2Te_3 thin films with further inclusion of trigonal warping [304].

Alternatively, the mirror reflection is partially broken in a honeycomb lattice and hence the QAHE is possible based on the symmetry analysis if the magnetic field does not orientate

along the six special directions that preserve the mirror reflection. However, detailed calculations show that the QAHE cannot be realized in the planar honeycomb lattice where only the Kane–Mele type intrinsic spin–orbit coupling exists. Further investigations reveal the importance of intrinsic Rashba spin–orbit coupling in low-buckled honeycomb lattice of, e.g. silicene, where the simultaneous presence of both types of spin–orbit couplings can open up a bulk band gap around M points that are saddle points with strong anisotropy rather than the conventionally focused Dirac points. This bulk band gap is topologically nontrivial and hosts QAHE when the spin-splitting from in-plane magnetization is strong enough to close the band splitting at M points [305]. The low-energy physics of this QAHE is theoretically different from the previous ones based on isotropic Dirac models [9, 40, 46]. Higher Chern number QAHEs are predicted in Bernal-stacked multi-layer systems where the out-of-plane electric field can decrease the lowest critical magnetization strength required to realize QAHE and even induce topological phase transition between topological phases with different Chern numbers [305].

On the other hand, in a buckled honeycomb lattice system, the in-plane magnetic field may be employed by considering only the magnetic flux induced orbital effect, in analogy to Haldane model [306]. As displayed in the upper left diagram of figure 15, the in-plane magnetic field can generate a finite magnetic flux in the three outer triangles around the hexagon. Although the detailed flux configuration is different from that in the Haldane model, as displayed in the lower panel of figure 15, the total magnetic flux is zero in the whole system and a Chern number of $C = 1$ is induced for the spinless fermion, which is the same as that in the Haldane model. In realistic materials with a spinful fermion, the Chern number will double if the Zeeman splitting and the spin–orbit coupling do not close the bulk band gap. Note that, the magnetic flux configuration is strongly dependent on the angle of the magnetic field, and a topologically trivial phase occurs when this angle is rotated through 90 degrees as illustrated in upper right panel of figure 15. Therefore, a topological phase transition is easily manipulated by changing the direction of the magnetic field, which is the second major difference from that in Haldane model.

3.7. QAHE with magnetic texture: antiferromagnetism and skyrmion

To engineer QAHE, the breaking of time-reversal invariance is crucial and can usually be achieved by introducing the ferromagnetic order [40, 46]. Alternatively, the QAHE has been theoretically proposed in the system with anti-ferromagnetism [231] and non-coplanar magnetism, i.e. the skyrmion [307–309]. With antiferromagnetic order, the QAHE was theoretically predicted in a $(1\ 1\ 1)$ perovskite material with low-buckled honeycomb lattice structure in the presence of a perpendicular electric field [310]. In the low-buckled honeycomb lattice system, the strong intra-atomic spin–orbit coupling is expected to generate a large Kane–Mele-type intrinsic spin–orbit coupling, giving rise to a QSHE. However, the presence of the anti-ferromagnetic order induces a spin-sublattice

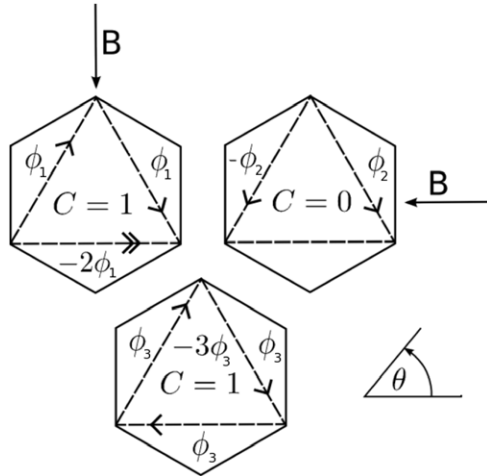


Figure 15. Hexagonal unit cells with zero net magnetic flux. The upper two unit cells are a buckled honeycomb lattice in an in-plane magnetic field. The lower figure is Haldane's unit cell. The direction of positive flux accumulation is indicated by the arrows along the bonds. For clarity, only the bonds along a single sublattice are shown. Reprinted with permission from [306].

dependent site potential and breaks the time-reversal symmetry to drive the QSHE into a band insulator. The further application of a perpendicular electric field triggers a single band inversion at one valley while keeping the gap open at the other valley, leading to a valley-polarized QAHE with a Chern number $C = 1$.

Alternative to the system with ferromagnetic or antiferromagnetic order, the real-space spin texture of non-coplanar magnetism makes the itinerate electrons coupled with the spin texture via exchange interaction, obtaining a phase accumulation during its hopping to induce a Berry curvature in the momentum space [307–309]. The QAHE has been proposed in a 2D electron system that strongly couples with the spin texture of a skyrmion crystal structure in the strong exchange interaction limit [308] and in graphene proximately coupled with a skyrmion lattice in the weak exchange interaction limit [309]. Different from the previous proposals of QAHE in graphene, the spin-orbit coupling is unnecessary in the latter case [309].

3.8. Edge-state engineering

Although the QAHE is a consequence of the bulk topology of band structure, its representative character that is required for application is the robust dissipationless chiral edge modes, which can also be engineered by simply manipulating a finite-sized ribbon [311–313]. The most effective approach to engineer the chiral edge modes at the boundaries is to destroy or remove half of the spin-helical edge modes of the QSHE, since their spin-up and -down states propagate in opposite directions so the Zeeman field is expected to lift the degeneracy between the Kramers pair. Li *et al* found that when applied at the boundary the field can drive states with one spin away from the boundary, but the remaining gapless edge states with opposite spin are also localized at the boundaries. Therefore, only the gapless chiral edge states with a specific spin are

present, which gives a quantized two-terminal conductance as well as the Hall conductance [311]. Such a Zeeman field appearing at the edges can be induced from the proximity effect with a ferromagnetic insulator. In addition, it is found that the hopping amplitude between the topological insulator and a normal insulator can also lead to a spatial separation between the two copies of the counter-propagating edge states carrying opposite spins [313].

4. Quantum valley-Hall effect (QVHE) and topological zero-line modes

In this section we review the QVHE and other valley-related topological phases in graphene and graphene-like honeycomb lattice systems. Here, we emphasize that although the robustness of the QVHE cannot compete with that of the QAHE, it is comparable with that of the \mathbb{Z}_2 TI. For example, the formation of the \mathbb{Z}_2 TI requires the time-reversal invariance, while the existence of QVHE requires the absence of inter-valley mixing. The chiral edge modes of the QAHE are robust against any kind of impurities, since they are protected from backscattering by the large spatial separation between two opposite sample boundaries. However, the spin-helical edge modes of the \mathbb{Z}_2 TI are only robust against elastic back-scattering from nonmagnetic impurities due to the topological protection from the time-reversal invariance, while the valley-helical edge modes of the QVHE are robust against smooth impurities due to the topological protection from the large-momentum separation [53, 54].

Nevertheless, different from the \mathbb{Z}_2 TIs and QAHE discussed above, the QVHE or topological 1D ZLMs do not rely on quantum manipulation of real-spin related effects such as spin-orbit coupling and ferromagnetism, but only require an external electric field, which is easily realizable in the lab. Therefore, superior to the QAHE that can only be experimentally observed at extremely low temperatures, multilayer graphene-based QVHE and topological 1D ZLMs should, in principle, be able to bring about a revolutionary development in room-temperature low-energy-consumption electronics or valleytronics.

4.1. Topological aspect of honeycomb lattice from inversion-symmetry breaking

In graphene and graphene-like honeycomb-lattice systems, one of the most important properties is the structurally-induced linear Dirac dispersions at two inequivalent valleys K and K' points, which are closely related to each other by the time-reversal symmetry. In the absence of short-range scattering, the valleys are decoupled and possess a long valley lifetime due to their large-separation in momentum space. Therefore, the electron in either specific valley (K or K') effectively breaks the time-reversal symmetry [314], and can give rise to a finite magnetic momentum as a consequence of the local intrinsic Berry curvature when a bulk band gap is opened by breaking the inversion symmetry (see figures 16(b₁) and (c₁)) [52]. The presence of the nontrivial Berry curvature

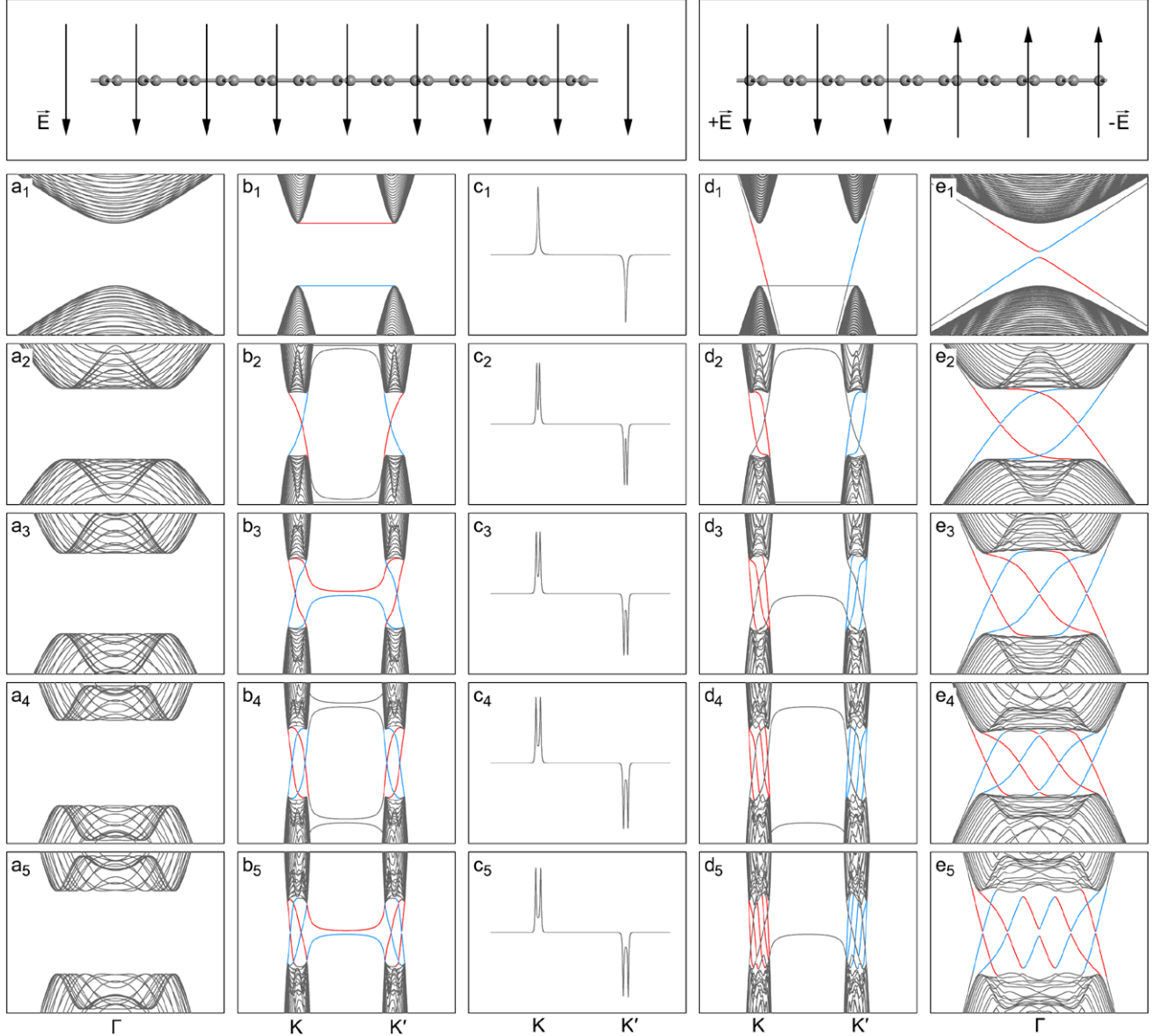


Figure 16. Left figure, upper panel (QVHE): the uniform staggered sublattice potential for a monolayer and perpendicular electric field for multilayer graphene; the corresponding Berry curvature profiles of the induced QVHE are plotted in the third column c_i , with $i = 1\text{--}5$ indicating the layer number. The Chern number for a single valley is $0.5i$ ($i = 1\text{--}5$) per spin as labeled by $C_{K,K'}$. The electronic structures of the armchair and zigzag ribbons are plotted in the first and second columns, labeled by a_i and b_i ($i = 1\text{--}5$), respectively. The edge states are absent in the armchair terminated nanoribbon due to inter-valley scattering. For the zigzag nanoribbon, the K and K' valleys are well separated and edge states are present, coloured red and blue on different sides of the boundary. We see that the pair of edge states at two boundaries are the same and equal to $N/2$ for each spin for even N layer graphene, while unbalanced edge state numbers occur for odd N -layer graphene. Right figure, upper panel (zero line modes): the varying site potentials for a monolayer or varying electric field direction changes sign, 1D topological ZLMs are present for both armchair and zigzag terminated interfaces, as shown in the fourth and fifth columns labelled by d_i and e_i ($i = 1\text{--}5$), respectively. The number of ZLMs propagating parallel or antiparallel to the interface is equal to i per spin (labelled in blue or red, respectively). Apart from the similarities, there are two differences between the band structures in the fourth and fifth column: (1) Gapless ZLMs are present in the zigzag terminated interface while a relatively small band gap occurs for ZLMs along an armchair terminated interface due to strong inter-valley scattering; (2) gapless edge states occur for a zigzag terminated ribbon at the outer boundary rather than at the interface, as plotted in the fourth column in gray. Reprinted with permission from [46], copyright 2010 American Physical Society.

concentrated at valleys K and K' has led to many fascinating transport properties, e.g. the valley Hall effect where a valley current flows along the direction transverse to the applied longitudinal charge current [52]. In the transition metal dichalcogenides materials, the inversion-symmetry breaking can also induce a large band gap at valleys K and K' where the strong spin-orbit coupling lifts the spin degeneracy of the bands [315]. However, the Kramers degeneracy is preserved due

to time-reversal symmetry, which relates the spin-up states at valley K to a energy-degenerate-spin-down state at valley K' . The locking of the spin and valley indices can not only result in a combined spin-valley Hall effect in the electron- or hole-doped region [315], which has been recently observed in experiment [316], but also gives rise to a valley-selective photo-excitation of carriers that provides the possibility of controlling spin and valley indices via an optical method. This

kind of spin-valley coupling physics can also be applied to the low-buckled honeycomb-lattice structures (e.g. silicene and germanene) by externally breaking the inversion symmetry [317, 318]. The analogy between valley and spin degrees of freedom as well as their interplay in a system with strong spin-orbit coupling provides superb properties and promising applications in the next generation of spintronics and valleytronics [51, 52, 314–330]. Several excellent reviews on the physics and possible applications based on the spin-valley locking have been published already, so they will not be mentioned further here [320–323]. Apart from these fascinating properties pertaining to the Fermi levels lying inside the valence or conduction bands, when the Fermi energy is located inside the bulk gap, the bulk band topology also leads to other striking transport properties, i.e. the QVHE in analogy to the QSHE as will be discussed below.

4.2. Quantum valley-Hall effect

Both the monolayer and Bernal-stacked multilayer graphene are zero-gap semiconductors with distinct dispersions at the Dirac points K and K' . A topologically nontrivial bulk gap can be opened to initiate the QVHE when the inversion-symmetry is broken, e.g. by introducing a staggered sublattice potential in monolayer graphene or by applying a perpendicular electric field in multilayer graphene. Distinct from the rigorous definition of the topological indices of the QAHE and the \mathbb{Z}_2 TIs, the QVHE is simply characterized by the valley Hall conductivity given by $\sigma_{xy}^v = (\sigma_{xy}^K - \sigma_{xy}^{K'})/2$ for the spinless case, where $\sigma_{xy}^{K,K'}$ is obtained by integrating the Berry curvatures near valleys K and K' by using the low-energy continuum model. When the bulk band gap is small, the finite Berry curvatures are mainly concentrated at the Dirac points, with the two valleys being well-separated. In the absence of the inter-valley scattering, the resulting valley Hall conductivity assumes an integer (half-integer) for even (odd) N-layer graphene.

Such a bulk quantization only has edge correspondence at specific system boundaries without strong inter-valley interaction. For example, zigzag ribbon geometries with a large momentum separation between valleys can support gapless edge modes, manifesting the quantized valley-Hall conductivity of the bulk (an exception is the monolayer case where there are only flat bands connecting two valleys in the same conduction or valence band). For even N, there are $N/2$ pairs of valley-helical edge modes located at both zigzag boundaries, in consistence with the quantization of the valley Hall conductivity. However, for odd N, a qualitatively distinct feature presents for the valley Hall edge modes that we shall discuss in detail later [54]. Since there must be no inter-valley-scattering, the quantum valley Hall effect can be considered as a ‘weak’ TI when compared with the topologically-protected quantum Hall effect. This scenario resembles the requirement of the time-reversal symmetry protection for the \mathbb{Z}_2 TI.

Nevertheless, the valleys binary degree of freedom is different from the electron spin and there is no rigid bulk-edge correspondence for the QVHE, which can be seen from the following facts: (1) there are no gapless valley Hall edge

modes for ribbons where valleys K and K' are strongly coupled, especially in the armchair case (see the left column of figure 16); (2) there are no gapless edge states for monolayer graphene even in zigzag nanoribbons, as shown in figure 16(b₁). Therefore, in the following, we centre on the topological properties of mono- and multilayer graphene and only discuss the edge states in zigzag nanoribbons.

For monolayer graphene, the inversion symmetry can be broken by using a substrate with inequivalent AB sublattice potentials, such as a hexagonal boron nitride (h-BN) monolayer [331–333], or by adsorbing top-site adatoms in a certain type of sublattice [47]. When the inversion symmetry is broken, the Berry curvature has opposite signs at the K and K' valleys due to the time-reversal invariance $\Omega(-\mathbf{k}) = -\Omega(\mathbf{k})$, as shown in figure 16(c₁), which gives rise to opposite Chern numbers $C_K = 0.5$ and $C_{K'} = -0.5$ at different valleys for each spin [52]. Therefore, when the spin degree of freedom is invoked, the Chern numbers for the K and K' valleys are, respectively, ± 1 , which resemble the Chern numbers for the spin-up and -down copies in the QSHE. However, there are no gapless edge states but flat bands connecting valleys K and K' in the zigzag nanoribbons with well-separated valleys, as illustrated in figure 16(b₁), in contrast to the gapless edge states in the QSHE. When the electron-electron interaction is included, the flat bands become dispersive and the spin-degeneracy is lifted, thus inducing spin-polarized edge modes with opposite spin-polarizations at opposite boundaries [334, 335]. This is also an approach to magnetize graphene for applications in spintronics.

In Bernal stacked multilayer graphene, the quasiparticles are chiral in the sublattice space. In the long wavelength limit, the *effective* AB sublattices degree of freedom in multilayer graphene is intimately related to the top/bottom layers degree of freedom, which is different from that in monolayer graphene with AB sublattices in the same plane. This makes it possible to break the inversion symmetry by applying a perpendicular electric field (equivalent to introducing different site potentials in the top/bottom layers), which can also open a bulk band gap at valleys K and K' , as displayed in the second column of figure 16. In bilayer graphene, contrary to the half-Chern number contribution in monolayer graphene, each valley contributes to a unit Chern number. This leads to the formation of gapless valley-helical edge states in the zigzag nanoribbons. For an even number of layers, the edge states are balanced at each edge. However, they are unbalanced for an odd number of layers, as shown in figure 16 where the red lines indicate the edge states within one boundary while states in blue are localized on the other side [53, 54]. Different from the QAHE chiral edge states, backscattering is possible due to the spatial overlapping of these counter-propagating edge states, as their large momentum separation protects them from the long-range scattering potential. If atomic short-range scattering does occur, e.g. through armchair termination of the graphene nanoribbon, then the valley-Hall conductance is no longer quantized and the edge states can even be destroyed, as in the case of time-reversal symmetry breaking scattering in \mathbb{Z}_2 TIs.

Similar results are expected in silicene [208, 270, 336], germanene, and other artificial honeycomb lattice systems such as photonic crystals and optical lattices [153]. This valley-related physics can also find application in square optical lattices, which have high tunability and hence the QVHE may be realized by applying valley-dependent gauge fields [337].

In addition to the breaking of sublattice symmetry, it is theoretically shown that the strain aligned along three main crystallographic directions of graphene can result in a valley-opposite gauge field, which corresponds to a strong uniform magnetic field and induces Landau quantization of the Dirac dispersion [338]. However, the valley-opposite character of the gauge field, constrained by the time-reversal symmetry, makes the Landau quantization exhibit opposite signs at valleys K and K' , which leads to the formation of the QVHE [338]. These pseudo-magnetic fields have been experimentally observed in highly strained graphene nanobubbles grown on Pt (1 1 1) with a magnitude of greater than 300 tesla [339] and in artificial honeycomb lattice of carbon monoxide molecules over a 2D electron gas at a Cu (1 1 1) surface [340]. Similar results have been generalized into bilayer graphene [341], twisted bilayer graphene [342, 343] and photonic crystal structures in honeycomb lattice [344–346] both theoretically and experimentally. Recently, by applying the external out-of-plane magnetic field, the valley polarized Landau levels have been experimentally observed in monolayer graphene [347].

4.3. Coexistence of the QVHE and other topological phases

Strictly speaking, an insulator without (with) time-reversal symmetry can be classified into several groups according to their different Chern numbers (\mathbb{Z}_2 index). In general, these topologically distinct phases cannot coexist simultaneously. For example, it is impossible to find a material that is both a QAHE structure and a \mathbb{Z}_2 TI, because the former requires breaking of time-reversal symmetry while the latter requires its preservation. However, the QVHE originates from the local Berry curvature around Dirac points that are well separated in momentum space. Therefore, in principle it does not conflict with the QAHE or a TI that originated from the global topology of the band structure, and should be compatible with either of them. This will now be discussed below.

4.3.1. Time-reversal invariant systems. In honeycomb lattice materials, there are two representative physical mechanisms that can give rise to a \mathbb{Z}_2 TI. One is to introduce intrinsic spin-orbit coupling into a monolayer graphene. It was shown that in Haldane model or Kane–Mele model, this intrinsic spin-orbit coupling competes with the inversion-symmetry breaking term, i.e. the staggered sublattice potential [9]. Therefore, this kind of TI based on intrinsic spin-orbit coupling cannot coexist with the QVHE. The other mechanism is to consider the Rashba spin-orbit coupling in gated Bernal stacked graphene multilayers [53, 54]. Contrary to the intrinsic spin-orbit

coupling induced TI phase where the spin degenerate gapless edge states connect the conduction and valence band edges of the K and K' valleys, respectively, in the Rashba spin-orbit coupling induced TI the gapless edge modes link the conduction and valence band edges in the same K or K' valley (see figure 2(l)), which gives rise to a well-defined valley Chern number. Therefore, the Kramers-degenerate pairs at the edge possess opposite spins as well as opposite valleys, as displayed in figure 17, thus the QVHE and \mathbb{Z}_2 TI can be realized simultaneously.

4.3.2. Time-reversal symmetry breaking systems. Although a well-defined valley index can also be given to the QAHE edge states in monolayer and Bernal-stacked multilayer graphene, the inversion symmetry relates the K and K' valleys and guarantees the equal contribution of these two valleys to the Chern number and hence the number of edge states. As a consequence, the edge modes from both valleys propagate along the same direction, exhibiting a chiral propagation nature and giving rise to a vanishing valley current [46, 253, 300], which is different from the case of a \mathbb{Z}_2 TI in multi-layer graphene where the edge states in different valleys are related via the time-reversal symmetry and hence propagate in opposite directions [53]. When the inversion symmetry is further broken, for example because of a low buckled structure [266, 267] or a staggered sublattice potential [206, 276], a band inversion is induced in one valley while the band gap in the other valley is preserved, then the unbalanced contribution to the Chern number from these two valleys leads to a new type of topological phase, i.e. the valley-polarized QAHE phase [206, 266, 267, 276].

This new phase has been reported in monolayer silicene [266, 267] and half-hydrogenated Bi bilayers [206, 276], which possess the characteristics of both QVHE and QAHE. In monolayer silicene, the joint influence of the Zeeman field and Rashba spin-orbit coupling leads to a QAHE with a Chern number of $C = 2$, equally contributed from valleys K and K' , similar to that in graphene. Unlike monolayer graphene, two types of Rashba spin orbit-coupling, intrinsic and extrinsic, can exist in silicene, either of which can induce the QAHE. However, their coexistence leads to competition, so that the contributions to the Chern number from valleys K and K' are, respectively, $C_K = 1$ and $C_{K'} = -2$, resulting in a Chern number of $C = C_K + C_{K'} = -1$ and a valley Chern number of $C_V = C_K - C_{K'} = 3$. As shown in figure 17(c), such a valley imbalance induces both a net valley current and a net charge current at each edge of the zigzag silicene nanoribbon [266]. For the half-hydrogenated Bi bilayer, however, due to the strong sublattice imbalance, the Chern number contributions from the two different valleys are, respectively, $C_K = 1$ and $C_{K'} = 0$, indicating a charge Chern number of $C = 1$ and a valley Chern number of $C_V = 1$ [266, 267]. It is noteworthy that, although the \mathbb{Z}_2 TI and the QAHE cannot exist simultaneously, the time-reversal symmetry breaking QSHE can coexist with the QAHE, in the same manner as reported in [348].

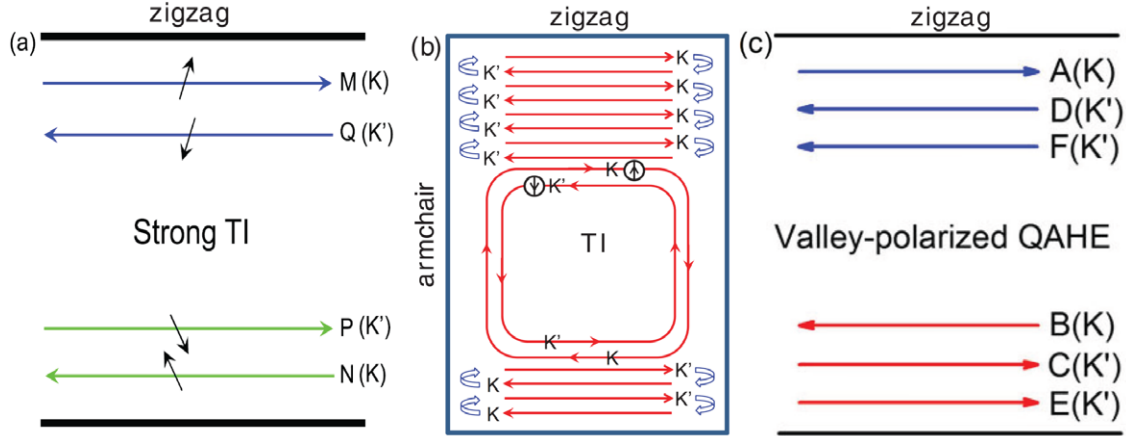


Figure 17. Schematic of edge state propagation in the zigzag edge geometry for a TI in (a) bilayer (b) trilayer graphene. The arrows on the edge channels represent in-plane spin directions (out-of-plane spin component is zero). For trilayer graphene, the major difference from the QVHE in figure 16 is that one more pair of time-reversal invariance protected spin-helical edge states emerges at each boundary of the zigzag or armchair trilayer graphene ribbon. Note that in the zigzag geometry, all the edge modes are associated with both spin and valley degrees of freedom. (c) Schematic of edge states of the valley polarized QAHE. Figure (a) reprinted with permission from [53], copyright 2011 by the American Physical Society. Figure (b) reprinted with permission from [54], copyright 2012 by the American Physical Society. Figure (c) reprinted with permission from [266], copyright 2014 by the American Physical Society.

4.4. Topological zero-line modes

4.4.1. Proposals and electronic structures. When the valley Hall topologies are varied spatially, e.g. by applying electric fields in different directions, a topological ZLM arises along the interface between the regions with opposite valley-Chern numbers. These ZLMs based on topological confinement were first proposed by Martin *et al* in a bilayer graphene continuum model, as illustrated in figure 18, where two electric fields opposite in sign are applied at two regions separated by a zero line [349]. Similar to the QVHE in multilayer graphene, chirally propagating gapless edge states are present in the zigzag terminated zero-line as displayed in figure 16(d₂), where an equal number of ZLMs are present in the K and K' valleys propagating along opposite directions.

However, in the armchair-terminated zero-line, the chirally propagating edge states are also present despite a relatively small, avoided crossing band gap at the crossing points between counter-propagating edge states, as shown in figure 16(e₂), which is different from the QVHE electronic structure in the armchair nanoribbon plotted in figure 16(a₂). Although in the QVHE there is no rigid bulk-edge correspondence at the boundary between the bulk and vacuum, the ZLMs are shown to be robust, with their number characterized by the difference in the valley Chern numbers across the interface [120, 350]. Very recently, according to the original proposal of Morpurgo [349], Li *et al* experimentally reported the evidence of the ZLMs at the line junction of two electrically biased bilayer graphene with opposite field polarities [351]. This method provides a more flexible and tunable way to realize ZLMs that strongly benefit their application in valleytronics comparing to the ZLMs experimentally observed at the interface of AB/BA stacked bilayer graphene as described below [352]. Similar results are present in Bernal-stacked multilayer graphene (see the 4th and 5th columns of figure 16), while ZLMs can even form at the interface between multilayer graphene structures with different layer numbers, and the resulting pairs of ZLMs

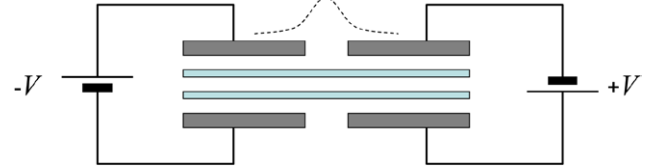


Figure 18. Side view of gated bilayer graphene configuration with a voltage kink. The region where the interlayer voltage changes sign (channel) supports bands of chiral zero-modes (dashed line). Conventional (non-topological) confinement would correspond to the same polarity of bias on both sides of the channel. Reprinted with permission from [349], copyright 2008 by the American Physical Society.

are determined by the difference in the Chern numbers of a single valley across the interface [353].

This scenario can also be extended to the monolayer graphene case [354], where the quantum valley Hall gap is opened by a staggered sublattice potential [333, 355] rather than a perpendicular electric field since the AB sublattices reside in the same plane. The ZLMs in monolayer graphene with different edges have been investigated by employing a tight-binding model rather than a long wavelength low-energy continuum model. It is found that although gapless ZLMs are present at the zigzag-type zero-line interface (see figure 16(d₁)), an avoided-crossing band gap is opened at the crossing points of ZLMs inside the bulk band gap in the armchair-type zero-line interface, as displayed in figure 16(e₁) [354]. These effects can also find application in silicene, where the low-buckled structure allows the realization of ZLMs via the application of a perpendicular electric field similar to that in bilayer graphene [356].

Additionally, ZLMs can also be generated at the interface between bilayer graphene structures with different stacking orders (e.g. AB or BA stacking) under a uniform electric field, as illustrated in figure 19(a) [352, 357, 358]. Since the valley Chern numbers that characterize valley topologies change sign across the interface between AB and BA stacking layers,

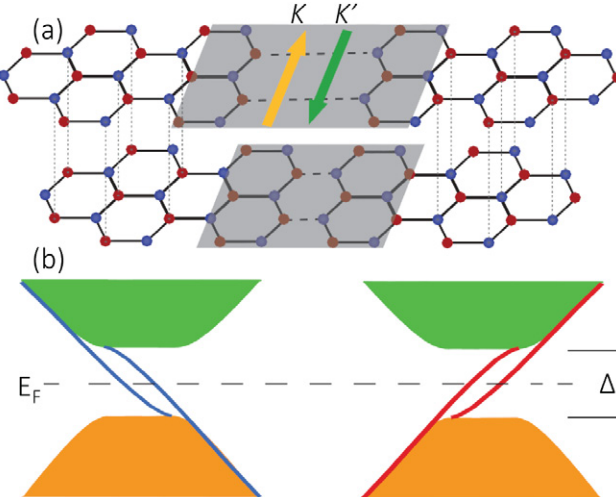


Figure 19. (a) Schematic of the zero line as an interface between AB and BA stacked bilayer graphene and (b) the corresponding band structure under electric field. Reprinted figure with permission from [352].

the same ZLMs arise along the interface (see figure 19(b)). Compared with the ZLMs induced by spatially manipulating the external electric fields, the different stacking order-induced ZLMs are rather easier to realize experimentally. Very recently, such a scheme was demonstrated in a suspended bilayer graphene system with a smoothly-varying interface that effectively suppressed the inter-valley scattering due to the absence of atomic scale disorders [352]. The uniform electric field induced ZLMs at the interface separating different stacking orders can also find application in low-buckled honeycomb structures, e.g. silicene, where the zero lines form at the interface between two regions with opposite buckling configurations [359]. Apart from the zero lines formed in some ribbons, the ZLMs have also been experimentally realized in superlattice structures, where periodic AB and BA stacking patterns are present [360]. Theoretically, similar to the superlattices with adjacent AB and BA stacking orders that may support ZLMs at the boundaries, ZLMs can also be realized in graphene on top of h-BN substrates as a result of lattice mismatch [361]. In addition to the line defect exhibited when the stacking order of bilayer graphene changes, 1D ZLMs can also appear along the line defect of monolayer graphene theoretically if a suitable staggered sublattice potential is present [362].

In the above, we have mainly described ZLMs based on the time-reversal symmetric QVHE, where the time-reversal counterpart of the ZLMs at one valley K is located at the other valley K' [358]. However, this scenario is not merely restricted to the interface between two such systems with different valley Chern numbers. In principle, it should exist at any interface separating two different topological orders, e.g. in QAHE systems with different Chern numbers (i.e. $+C_1 - C_2$, $+C_1 + C_2$, and $+C_1 - C_2$), in QSHE systems with different topologies, in hybrid systems composed of both effects (or \mathbb{Z}_2 TI [356]), and in hybrid systems composed of the QAHE and a \mathbb{Z}_2 TI. To be specific, in monolayer graphene, the contributions of the Chern numbers from valleys K and K' are identical for

the QAHE, but are opposite for the QVHE. Therefore, at the interface between the two, the difference between the Chern numbers is nonzero for the valley K while it vanishes for the other valley K' . As a result, the ZLMs at the interface carry only the information of valley K and propagate chirally only along one direction, which is similar to the QAHE chiral edge modes but is valley-polarized.

In fact, the interface is not required to be a ‘line’, but may be slightly broadened due to mediation from the finite-size effect. For example, it is found that 1D ZLMs can also be hosted in a narrow graphene nanoroad embedded in h-BN sheets, where the boron (or nitrogen) atoms belong to different sublattices in two separate h-BN sheets [363]. Due to the inversion-symmetry breaking from the unbalanced site-energies in h-BN, a bulk band gap is opened at the K and K' valleys, which each carry half a Chern number of opposite sign. The inverse of the sublattice topology across the graphene nanoroad changes the sign of the Chern number for each individual valley, leading to the formation of ZLMs throughout the graphene ribbon region.

4.4.2. Transport properties of topological zero-line modes. Based on either the low-energy continuum model in the long wavelength limit or the tight-binding model Hamiltonian, we have now established a fundamental understanding of the electronic structure of ZLMs. The gapless modes appear in the zigzag-type interfaces where the K and K' valleys are decoupled, while a relatively small but nonnegligible band gap opens in the armchair-type interfaces due to the atomic structure induced strong inter-valley scattering. For any type of zero lines, the resulting ZLMs are always spatially overlapped in real space, which suggests that these counter-propagating states should be easily backscattered, especially in the case where inter-valley scattering occurs. However, it is shown that the wide-spread wavefunctions mitigate the back-scattering [353, 364] and these ZLMs also play an important role in the subgap conductance even in the presence of short-range disorder scattering [365] as reviewed in below.

To further verify the robustness of the ZLMs, electronic transport calculations have been performed using the Green’s function technique implemented with the multi-terminal Landauer-Büttiker formalism [363, 366, 367]. It has been shown that the ZLMs exhibit a chiral propagation characteristic for any kinds of zero lines, i.e. periodic, or curved with inter-valley scattering. Such a robustness against any specific zero-line geometry indicates their striking transport property of zero bend-resistance, similar to the dissipationless transport property of the quantum Hall effect in some extent. In the presence of disorder, either short- or long-range, it is shown that the ZLMs are rather robust even under any variation of the path directions whenever the Fermi-level does not lie inside the avoided crossing band gap of the armchair-type zero lines. The corresponding mean free path under some weak disorder is estimated to be as large as several microns, which promises innumerable applications in low power electronics and valleytronics. The robustness against disorder or path directions can be attributed to the wide spread of the counter-propagating ZLMs carrying opposite valley degrees of freedom [366].

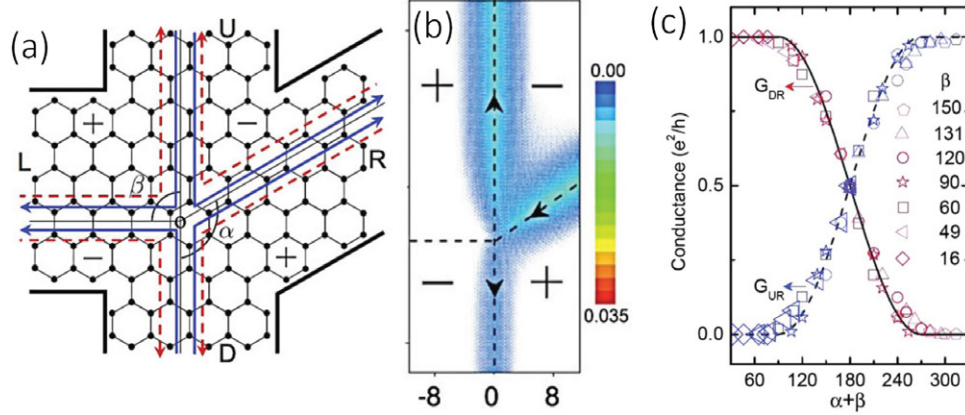


Figure 20. Current partition at the intersection of zero line modes. (a) Schematic of the zero line intersection. L, D, R, and U represent the left, down, right, and up leads, respectively. The angle between left and up leads is denoted by α , and that between right and down leads by β . The blue and red arrow lines indicate the chiral propagation of the ZLMs. (b) Partition of the current flowing from the right lead. (c) Conductance of the currents from the R zero line to the U and D zero lines as a function of $\alpha + \beta$ at the ZLM intersection in (a) for a series of β values. Reprinted with permission from [367], copyright 2014 by the American Physical Society.

According to the zero bend resistance characteristics of the ZLMs, when two zero-lines become crossed to form a topological intersection (see figure 20(a)), the chiral propagating modes obey an interesting and counterintuitive current partition law at the intersection, which depends only on the angle of incidence [367]. For example, when the incoming current from one terminal flows towards the intersection, the direct forward current cross the crossing point is forbidden due to the requirement of the chiral propagation, and the outgoing currents have only two possible directions, as illustrated in figure 20(a). Moreover, a counterintuitive current partition is formed because the incoming current prefers to turn a larger angle, as shown in figure 20(b) [367]. For the Fermi level close to the charge neutrality point (i.e. $E_F = 0.0$), the splitting of the current from any lead (e.g. the right lead) at the topological intersection simply depends on the combination of $\alpha + \beta$ (figure 20(c)) with α (β) being the angle between the left (right) and up (down) leads, as shown in figure 20(a). Such a counterintuitive current partition can be understood from the coupling between the wavefunctions at different paths forming the topological intersection [367].

However, although these ZLMs were theoretically predicted several years ago and were shown to have great application potential, experimental progress has been rather limited. The main difficulty is the design and fabrication of the devices, which for multilayer graphene require high precision alignment of the top and bottom gates, not to mention the control of eight gates in topological current splitter devices. With the development of state-of-the-art techniques for fine-tuning of the gates, it should be possible for such zero-lines to be engineered in the future. For current splitters made of multilayer graphene, at the topological intersection the top and bottom electric gates are in principle fixed, so the angles can no longer be tuned to realize different current partitions. For fixed multilayer graphene systems we must therefore explore other approaches to achieve tunability, e.g. by tuning Fermi levels, applying some appropriate electric fields, or weak magnetic fields.

5. Summary

In summary, we have provided an overview of the most recent research on the topologically nontrivial phases in 2D systems, such as \mathbb{Z}_2 TI, QAHE, and QVHE. A typical 2D material is graphene, a Dirac semi-metal with a half-filled valence band. The Dirac dispersion around the K and K' points are guaranteed by the sublattice symmetry and can be gapped by breaking this symmetry. Without spin-orbit coupling, a staggered sublattice potential can break the inversion symmetry to open up a band gap and form a QVHE with each valley spin carrying half a unit Chern number. In this effect, although there are no corresponding gapless edge state in monolayer graphene, midgap topological confinement states, i.e. ZLMs, can occur at the interface, across which the staggered potential changes sign. These ZLMs are protected from backscattering by the large momentum separation, but become gapped at the specific armchair zero lines. Moreover, it was shown that the ZLMs exhibit striking transport properties, e.g. zero bend resistance and counterintuitive current partition laws. Similar results can be applied to other honeycomb lattices and chirally stacked multilayer graphene. Recently, the ZLMs have already been experimentally observed in bilayer graphene through the application of a tunable electric field. These electric-field-tunable ZLMs provide the potential building blocks for constructing the next-generation electronics and valleytronics.

The Haldane model provides another scheme to break the chiral symmetry, i.e. by applying an alternating magnetic fluxes in a honeycomb lattice. The orbital effect of the magnetic field leads to the QAHE with a Chern number of $C = 1$. Although the time-reversal symmetry is broken, Landau levels are not formed due to the vanishing total magnetic flux. The orbital effect of the magnetic field induced QAHE may be seen in a buckled honeycomb lattice with an in-plane magnetic field. In addition, to form QAHE, there is another scheme that relies on spin-orbit coupling and out-of-plane ferromagnetism. In both semi-metals (e.g. graphene) and semiconductors (e.g. 3D-TI thin films), a ferromagnetic order Zeeman

Table 2. Possible materials for realizing the QAHE. 1st column: possible materials for realizing the QAHE. 2nd column: the corresponding Chern numbers. 3rd column: some remarks. 4th column: band gaps calculated from *ab initio*. Last column: relative references.

Material	\mathcal{C}	Remark	Gap	Reference
HgTe QWs	1			[238]
InAs/GaSb QWs	1	Magnetic doping		[239]
Junction QWs	1			[123]
3D TI thin film	1	2D limit, magnetic doping		[40]
3D TI thin film	Thickness dependent	Beyond 2D limit, magnetic doping		[298, 299]
3D TI thin film/FM	1		~ 10 meV	[291]
<i>n-p codoped 3D TI thin film</i>	1		> 50 meV	[251]
G	2	Theory		[46]
3d atom/G	2		$\sim 1\text{--}10$ meV	[300]
5d atom/G	2	Electric field tunable	$\sim 10\text{--}100$ meV	[48]
Ru atom/G	-2	4d atom	~ 10 meV	[137]
Co/Rh atom/G	1	Impurity-band contribution	$\sim 50/100$ meV	[259]
G/BiFeO ₃ (1 1 1)	2		~ 1 meV	[49]
G/RbMnCl ₃ (001)	2		$\sim 1\text{--}10$ meV	[262]
G/Skyrmion	2		~ 30 meV	[309]
Skyrmion lattices	1		~ 100 meV	[307, 308]
MLG	4 or 2	Theory		[300]
Silicene	2	Theory		[265]
Silicene	1	Theory, competition between λ_R^{int} and λ_R^{ext}		[266]
3d atom/silicene	2		~ 1 meV	[268–270]
4d atom/silicene	-2 or 1	Depend on atom type	~ 10 meV	[271]
Bi (1 1 1) BL	-2	Theory		[272]
I-stanene	1	Half functionalization	~ 340 meV	[275]
I-germanene	1	Half functionalization	~ 60 meV	[275]
Fun. silicene/germanene	2 or -1	Fractional one-side saturation		[274]
Fun. Bi (1 1 1)	1	-H, half functionalization	~ 200 meV	[206, 276]
Bi(BN)	1		~ 100 meV	[209]
W atoms on halogen-Si(1 1 1)	1	Artificial honeycomb lattice	~ 100 meV	[286]
2D triphenyl-Mn	1	Organic material	~ 9.5 meV	[287]
2D triphenyl-In	1	Flat Chern band insulator		[368]
Heterostructure QWs	-3, -2, -1, 1	Material dependent	1–700 meV	[288]
CdO/EuO or GdN/EuO	1	Intrinsic QAHE		[289, 290]
HgCr ₂ Se ₄ thin film	Thickness dependent	Intrinsic QAHE		[292]
(SrIr/TiO ₃) _n ($n = 1, 2$)	n			[295]
Monolayer La ₂ MnIrO ₆	1		~ 26 meV	[295]

Note: In this table, λ_R^{int} and λ_R^{ext} indicate the strength of intrinsic and extrinsic Rashba spin-orbit couplings, respectively; Bi(BN) represents the functionalized Bi (1 1 1) bilayer where one side is saturated by B atoms while the other side is saturated by N atoms. Abbreviations used, G: graphene; BL: bilayer; MLG: multilayer graphene; BLG: bilayer graphene; Fun.: functionalized; QWs: quantum wells.

field can invert the conduction and valence bands and induce crossing points. The spin-orbit coupling can lift the accidental degeneracies at the crossing points, open up a bulk band gap, and thus give rise to the QAHE. Various semi-metals and semiconductors have been proposed as host materials, as listed in table 2, where the ferromagnetic order can be established by magnetic doping, considering magnetic insulating substrates, or functionalizing. Alternatively, the QAHE can also be realized in materials with spontaneous ferromagnetism, like transition metal oxides and heterostructures composed of magnetic thin films. However, since the basic requisite is just the breaking of time-reversal symmetry, ferromagnetic metal with Anderson disorders, and systems with in-plane magnetization or anti-ferromagnetism may also be possible. Although the QAHE has been extensively studied on elements with an

outer p -shell, the explorations for transition metal compounds have been rather limited. The influence of the strong electron-electron correlations of these transition metals on the QAHE is also unclear. So far, the QAHE has only been observed in experiment under extremely low temperatures in magnetically doped 3D-TI thin films with the Chern number of $\mathcal{C} = 1$. The recent progress has shown the potential of realizing QAHE in graphene on insulating ferromagnetic substrate. For future applications, a large band gap (or high temperature) and simple experimental design are the motivations behind current research. Moreover, a large Chern number also benefits practical applications due to the strong quantized Hall-current density. In addition, artificial lattices with high tunability, like cold atoms in optical lattices, provide alternative platforms for simulation of the QAHE.

Another approach to break the chiral symmetry of graphene is to introduce the next-nearest-neighbour hopping related intrinsic spin-orbit coupling. The resulting QSHE can be regarded as a combination of two copies of the Haldane model with opposite spins and Chern numbers, which gives rise to spin-helical edge modes. These states are stable even when s_z is not a good quantum number, reflecting the topological nature that is characterized by a binary-valued \mathbb{Z}_2 topological index. This is a brand-new classification of insulators with time-reversal invariance. Though the intrinsic spin-orbit coupling of graphene is extremely weak, it can be externally engineered via various methods, like adsorbing heavy atoms. The \mathbb{Z}_2 TI also exists in other Dirac materials, e.g. honeycomb lattices of group-IV elements, organic materials, etc as listed in table 1. Except for these intrinsic Dirac materials with two inequivalent Dirac cones, strain and electric fields can also induce Dirac dispersions that can be gapped by the spin-orbit coupling to form a \mathbb{Z}_2 TI.

Apart from the Dirac materials, semiconductors with a small band gap can also generate a \mathbb{Z}_2 TI when spin-orbit coupling is strong enough to close the band gap, and hence heavy atoms such as Bi, Tl, Te, and Hg may play an important role. The Bi (1 1 1) bilayer is a good example of a group-V element. Although the Bi bilayer has a honeycomb-lattice structure, the full-filled valence bands make it an insulator rather than semimetal with a bulk gap opened at the Γ point. The strong spin-orbit coupling from Bi induces a band inversion to form a TI. Similar band inversion induced TIs can also be found in other atomic crystal layers, e.g. Bi or Tl based III-V compounds and Bi based V-VII compounds. Superior to the TI with light atoms, the heavy atom based TIs usually have large nontrivial band gaps, which offers the possibility for room-temperature applications. Additionally, functionalization is another useful approach to obtain TIs with a large band gap. So far, the \mathbb{Z}_2 TI has already been experimentally observed in CdTe/HgTe/CdTe and InAs/GaSb semiconductor quantum wells, based on band inversion. Such kind of band inversion is also expected to occur by disorders, leading to the ‘topological Anderson insulator’.

On one hand, these topological phases possess topologically protected edge modes that perform as perfectly conducting 1D wires. This holds great potential as building blocks in dissipationless quantum electronic devices, like interconnects between chips. The helical edge states of opposite spin (valley) in QSHE (QVHE) may also have potential applications in spin/valley-related electronics, for example, spin (valley) filter. Moreover, the proximity effect of \mathbb{Z}_2 TI on superconductors leads to the formation of an exotic quasi-particle of Majorana fermion [369, 370], which may have promising applications in fault-tolerant quantum computation [371, 372]; the resulting Andreev reflection and crossed Andreev reflection also possess promising applications in quantum teleportation and quantum computation by making use of the spatially-separated electrons with entangled spin and momentum [373–376]. Similar proximity effects of the QAHE/QVHE proximity-coupled to superconductors are still open issues for future study.

On the other hand, although many experimental progresses have been made towards the realization of these 2D topological phases, the low observation temperature still limits the potential applications. Thus, searching for topological phases that may preserve at room temperature is crucial. Moreover, high Chern number QAHE or high valley Chern number QVHE/ZLMs that can give stronger electrical signal are also highly desired. Furthermore, from the theoretical point of view, searching for new mechanisms to give rise to QAHE, e.g. using in-plane magnetization, or other topologically protected phases may also be interesting topics for the further investigation.

Note added: During the preparation of the present review, we become aware of several interesting review articles about the QAHEs [377–380].

Acknowledgments

YR appreciates the valuable discussions with F Zhang and Y Zhang as well as the help from Xinzhou Deng and Ke Wang on plotting figures. ZQ and YR are financially supported by the 100-Talent Program of Chinese Academy of Sciences, China Government Youth 1000-Plan Talent Program, National Natural Science Foundation of China (NNSFC, Grant No. 11474265), Fundamental Research Funds for the Central Universities (Grant Nos.: WK3510000001, WK2030020027), and Anhui Provincial Natural Science Foundation. QN is financially supported by the Welch Foundation (Grant No. F-1255), DOE (Grant No. DE-FG03-02ER45958, Division of Materials Science and Engineering), the MOST Project of China (Grant No. 2012CB921300, 2013CB921900), and NNSFC (Grant No. 91121004). The Supercomputing Center of the University of Science and Technology of China is gratefully acknowledged for high-performance computing assistance.

References

- [1] Thouless D J, Kohmoto M, Nightingale M P and den Nijs M 1982 Quantized Hall conductance in a two-dimensional periodic potential *Phys. Rev. Lett.* **48** 405
- [2] von Klitzing K, Dorda G and Pepper M 1980 New method for high-accuracy determination of the fine-structure constant based on quantized Hall resistance *Phys. Rev. Lett.* **45** 494
- [3] von Klitzing K 2004 25 Years of quantum Hall effect (QHE) a personal view on the discovery, physics and applications of this quantum effect *Séminaire Poincaré* **2** 1
- [4] Avron J E, Seiler R and Simon B 1983 Homotopy and quantization in condensed matter physics *Phys. Rev. Lett.* **51** 51
- [5] Simon B 1983 Holonomy, the quantum adiabatic theorem and Berry’s phase *Phys. Rev. Lett.* **51** 2167
- [6] Niu Q, Thouless D J and Wu Y S 1985 Quantized Hall conductance as a topological invariant *Phys. Rev. B* **31** 3372
- [7] Hatsugai Y 1993 Chern number and edge states in the integer quantum Hall effect *Phys. Rev. Lett.* **71** 3697
- [8] Nagaosa N, Sinova J, Onoda S, MacDonald A H and Ong N P 2010 Anomalous Hall effect *Rev. Mod. Phys.* **82** 1539
- [9] Haldane F D M 1988 Model for a Quantum Hall effect without Landau levels: condensed-matter realization of the ‘parity anomaly’ *Phys. Rev. Lett.* **61** 2015

- [10] Ohgushi K, Murakami S and Nagaosa N 2000 Spin anisotropy and quantum Hall effect in the kagomé lattice: chiral spin state based on a ferromagnet *Phys. Rev. B* **62** R6065
- [11] Onoda M and Nagaosa N 2003 Quantized anomalous Hall effect in two-dimensional ferromagnets: quantum Hall effect in metals *Phys. Rev. Lett.* **90** 206601
- [12] Chang M C and Niu Q 1995 Berry phase, hyperorbitals and the Hofstadter spectrum *Phys. Rev. Lett.* **75** 1348
- [13] Chang M C and Niu Q 1996 Berry phase, hyperorbitals and the Hofstadter spectrum: semiclassical dynamics in magnetic Bloch bands *Phys. Rev. B* **53** 7010
- [14] Sundaram G and Niu Q 1999 Wave-packet dynamics in slowly perturbed crystals: gradient corrections and Berry-phase effects *Phys. Rev. B* **59** 14915
- [15] Murakami S, Nagaosa N and Zhang S 2003 Dissipationless quantum spin current at room temperature *Science* **301** 1348
- [16] Sinova J, Culcer D, Niu Q, Sinitsyn N A, Jungwirth T and MacDonald A H 2004 Universal intrinsic spin Hall effect *Phys. Rev. Lett.* **92** 126603
- [17] Bernevig B A and Zhang S 2005 Intrinsic spin Hall effect in the two-dimensional hole gas *Phys. Rev. Lett.* **95** 016801
- [18] Kato Y K, Myers R C, Gossard A C and Awschalom D D 2004 Observation of the spin Hall effect in semiconductors *Science* **306** 1910
- [19] Wunderlich J, Kaestner B, Sinova J and Jungwirth T 2005 Experimental observation of the spin-Hall effect in a two-dimensional spin-orbit coupled semiconductor system *Phys. Rev. Lett.* **94** 047204
- [20] Murakami S, Nagaosa N and Zhang S 2004 Spin-Hall insulator *Phys. Rev. Lett.* **93** 156804
- [21] Novoselov K S, Geim A K, Morozov S V, Jiang D, Zhang Y, Dubonos S V, Grigorieva I V and Firsov A A 2004 Electric field effect in atomically thin carbon films *Science* **306** 666
- [22] Castro Neto A H, Guinea F, Peres N M R, Novoselov K S and Geim A K 2010 The electronic properties of graphene *Rev. Mod. Phys.* **81** 109
- [23] Kane C L and Mele E J 2005 Z_2 topological order and the quantum spin Hall effect *Phys. Rev. Lett.* **95** 146802
- [24] Kane C L and Mele E J 2005 Quantum spin Hall effect in graphene *Phys. Rev. Lett.* **95** 226801
- [25] Min H, Hill J E, Sinitsyn N A, Sahu B R, Kleinman L and MacDonald A H 2006 Intrinsic and Rashba spin-orbit interactions in graphene sheets *Phys. Rev. B* **74** 165310
- [26] Huertas-Hernando D, Guinea F and Brataas A 2006 Spin-orbit coupling in curved graphene, fullerenes, nanotubes and nanotube caps *Phys. Rev. B* **74** 155426
- [27] Yao Y, Ye F, Qi X L, Zhang S C and Fang Z 2007 Spin-orbit gap of graphene: first-principles calculations *Phys. Rev. B* **75** 041401
- [28] Boettger J C and Trickey S C 2007 First-principles calculation of the spin-orbit splitting in graphene *Phys. Rev. B* **75** 121402
- [29] Gmitra M, Konschuh S, Ertler C, Ambrosch-Draxl C and Fabian J 2009 Band-structure topologies of graphene: spin-orbit coupling effects from first principles *Phys. Rev. B* **80** 235431
- [30] Weeks C, Hu J, Alicea J, Franz M and Wu R 2011 Engineering a robust quantum spin Hall state in graphene via adatom deposition *Phys. Rev. X* **1** 021001
- [31] Liu C-C, Jiang H and Yao Y 2011 Low-energy effective Hamiltonian involving spin-orbit coupling in silicene and two-dimensional germanium and tin *Phys. Rev. B* **84** 195430
- [32] Xu Y, Yan B, Zhang H-J, Wang J, Xu G, Tang P, Duan W and Zhang S-C 2013 Large-gap quantum spin Hall insulators in tin films *Phys. Rev. Lett.* **111** 136804
- [33] Bernevig B A and Zhang S 2006 Quantum spin Hall effect *Phys. Rev. Lett.* **96** 106802
- [34] Bernevig B A, Hughes T L and Zhang S C 2006 Quantum spin Hall effect and topological phase transition in HgTe quantum wells *Science* **314** 1757
- [35] König M, Wiedmann S, Brüne C, Roth A, Buhmann H, Molenkamp L W, Qi X L and Zhang S C 2007 Quantum spin Hall insulator state in HgTe quantum wells *Science* **318** 766
- [36] Hasan M Z and Kane C L 2010 Colloquium: topological insulators *Rev. Mod. Phys.* **82** 3045
- [37] Shen S Q 2012 *Topological Insulators: Dirac Equation in Condensed Matters* (Berlin: Springer)
- [38] Bernevig B A and Hughes T L 2013 *Topological Insulators and Topological Superconductors* (Cambridge: Princeton University Press)
- [39] Qi X and Zhang S 2011 Topological insulators and superconductors *Rev. Mod. Phys.* **83** 1057
- [40] Yu R, Zhang W, Zhang H J, Zhang S C, Dai X and Fang Z 2010 Quantized anomalous Hall effect in magnetic topological insulators *Science* **329** 61
- [41] Chang C Z et al 2013 From magnetically doped topological insulator to the quantum anomalous Hall effect *Science* **340** 167
- [42] Checkelsky J G, Yoshimi R, Tsukazaki A, Takahashi K S, Kozuka Y, Falson J, Kawasaki M and Tokura Y 2014 Trajectory of the anomalous Hall effect towards the quantized state in a ferromagnetic topological insulator *Nat. Phys.* **10** 731
- [43] Kou X et al 2014 Scale-invariant quantum anomalous Hall effect in magnetic topological insulators *Phys. Rev. Lett.* **113** 137201
- [44] Chang C Z, Zhao W, Kim D Y, Zhang H, Assaf B A, Heiman D, Zhang S C, Liu C, Chan M H W and Moodera J S 2015 High-precision realization of robust quantum anomalous Hall state in a hard ferromagnetic topological insulator *Nat. Mater.* **14** 473
- [45] Winkler R 2003 *Spin-Orbit Coupling Effects in 2D Electron and Hole Systems* (Berlin: Springer)
- [46] Qiao Z, Yang S A, Feng W, Tse W K, Ding J, Yao Y, Wang J and Niu Q 2010 Quantum anomalous Hall effect in graphene from Rashba and exchange effects *Phys. Rev. B* **82** 161414
- [47] Ding J, Qiao Z, Feng W, Yao Y and Niu Q 2011 Engineering quantum anomalous/valley Hall states in graphene via metal-atom adsorption: an ab initio study *Phys. Rev. B* **84** 195444
- [48] Zhang H, Lazo C, Blügel S, Heinze S and Mokrousov Y 2012 Electrically tunable quantum anomalous Hall effect in graphene decorated by 5d transition-metal adatoms *Phys. Rev. Lett.* **108** 056802
- [49] Qiao Z, Ren W, Chen H, Bellaiche L, Zhang Z, MacDonald A H and Niu Q 2014 Quantum anomalous Hall effect in graphene proximity coupled to an antiferromagnetic insulator *Phys. Rev. Lett.* **112** 116404
- [50] Wang Z, Tang C, Sachs R, Barlas Y and Shi J 2015 Proximity-induced ferromagnetism in graphene revealed by the anomalous Hall effect *Phys. Rev. Lett.* **114** 016603
- [51] Rycerz A, Tworzydło J and Beenakker C W J 2007 Valley filter and valley valve in graphene *Nat. Phys.* **3** 172
- [52] Xiao D, Yao W and Qian Niu Q 2007 Valley-contrasting physics in graphene: magnetic moment and topological transport *Phys. Rev. Lett.* **99** 236809
- [53] Qiao Z, Tse W K, Jiang H, Yao Y and Niu Q 2011 Two-dimensional topological insulator state and topological phase transition in bilayer graphene *Phys. Rev. Lett.* **107** 256801
- [54] Li X, Qiao Z, Jung J and Niu Q 2012 Unbalanced edge modes and topological phase transition in gated trilayer graphene *Phys. Rev. B* **85** 201404
- [55] Pan H, Li X, Zhang F and Yang S A 2015 Perfect valley filter in topological domain wall *Phys. Rev. B* **92** 041404(R)

- [56] Lindner N H, Refael G and Galitski V 2011 Floquet topological insulator in semiconductor quantum wells *Nat. Phys.* **7** 490
- [57] Cayssol J, Dóra B, Simon F and Moessner R 2013 Floquet topological insulators *Phys. Status Solidi* **7** 101
- [58] Fu L 2011 Topological crystalline insulators *Phys. Rev. Lett.* **106** 106802
- [59] Liu J, Hsieh T H, Wei P, Duan W, Moodera J and Fu L 2014 Spin-filtered edge states with an electrically tunable gap in a two-dimensional topological crystalline insulator *Nat. Mater.* **13** 178
- [60] Ando Y and Fu L 2015 Topological crystalline insulators and topological superconductors: from concepts to materials *Annu. Rev. Condens. Matter Phys.* **6** 361
- [61] Raghu S, Qi X L, Honerkamp C and Zhang S C 2008 Topological Mott insulators *Phys. Rev. Lett.* **100** 156401
- [62] Hohenadler M, Toldin F P, Herbut I F and Assaad F F 2014 Phase diagram of the Kane–Mele–Coulomb model *Phys. Rev. B* **90** 085146
- [63] Scherer D D, Scherer M M and Honerkamp C 2015 Correlated spinless fermions on the honeycomb lattice revisited *Phys. Rev. B* **92** 155137
- [64] Dzero M, Sun K, Galitski V and Coleman P 2010 Topological Kondo insulators *Phys. Rev. Lett.* **104** 106408
- [65] Dzero M, Xia J, Galitski V and Coleman P 2015 Topological Kondo insulators (arXiv:1506.05635v1)
- [66] Nandkishore R and Levitov L 2010 Quantum anomalous Hall state in bilayer graphene *Phys. Rev. B* **82** 115124
- [67] Prada E, San-Jose P, Brey L and Fertig H A 2011 Band topology and the quantum spin Hall effect in bilayer graphene *Solid State Comm.* **151** 1705
- [68] Zhang F, Jung J, Fiete G A, Niu Q and MacDonald A H 2011 Spontaneous quantum Hall states in chirally stacked few-layer graphene systems *Phys. Rev. Lett.* **106** 156801
- [69] Zhang F, Jung J, MacDonald A H 2011 Spontaneous quantum Hall states and novel luttinger liquids in chiral graphene *J. Phys.: Conf. Ser.* **334** 012002
- [70] Neupert T, Santos L, Chamon C and Mudry C 2011 Fractional quantum Hall states at zero magnetic field *Phys. Rev. Lett.* **106** 236804
- [71] Sun K, Gu Z, Katsura H and Das Sarma S 2011 Nearly flatbands with nontrivial topology *Phys. Rev. Lett.* **106** 236803
- [72] Tang E, Mei J W and Wen X G 2011 High-temperature fractional quantum Hall states *Phys. Rev. Lett.* **106** 236802
- [73] Maciejko J and Fiete G A 2015 Fractionalized topological insulators *Nat. Phys.* **11** 385
- [74] Liu Z, Liu F and Wu Y S 2014 Exotic electronic states in the world of flat bands from theory to material *Chin. Phys. B* **23** 077308
- [75] Yakovenko V M 1991 Quantum Hall effect in quasi-one-dimensional conductors *Phys. Rev. B* **43** 11353
- [76] Kane C L, Mukhopadhyay R and Lubensky T C 2002 Fractional quantum Hall effect in an array of quantum wires *Phys. Rev. Lett.* **88** 036401
- [77] Klinovaja J and Loss D 2013 Topological edge states and fractional quantum Hall effect from Umklapp scattering *Phys. Rev. Lett.* **111** 196401
- [78] Teo J C Y and Kane C L 2014 From Luttinger liquid to non-Abelian quantum Hall states *Phys. Rev. B* **89** 085101
- [79] Klinovaja J and Loss D 2014 Integer and fractional quantum Hall effect in a strip of stripes *Eur. Phys. J. B* **87** 171
- [80] Klinovaja J, Tserkovnyak Y and Loss D 2015 Integer and fractional quantum anomalous Hall effect in a strip of stripes model *Phys. Rev. B* **91** 085426
- [81] Klinovaja J and Tserkovnyak Y 2014 Quantum spin Hall effect in strip of stripes model *Phys. Rev. B* **90** 115426
- [82] Santos R A, Huang C W, Gefen Y and Gutman D B 2015 Fractional topological insulators: from sliding Luttinger liquids to Chern–Simons theory *Phys. Rev. B* **91** 205141
- [83] Seroussi I, Berg E and Oreg Y 2014 Topological superconducting phases of weakly coupled quantum wires *Phys. Rev. B* **89** 104523
- [84] Nagaosa N 2006 Anomalous Hall effect: a new perspective *J. Phys. Soc. Japan* **75** 042001
- [85] Xiao D, Chang M C and Niu Q 2010 Berry phase effects on electronic properties *Rev. Mod. Phys.* **82** 1959
- [86] Qi X and Zhang S 2010 The quantum spin Hall effect and topological insulators *Phys. Today* **63** 33
- [87] Maciejko J, Hughes T L and Zhang S 2011 The quantum spin Hall effect *Annu. Rev. Condens. Matter Phys.* **2** 31
- [88] Ezawa M 2012 Topological phase transition and electrically tunable diamagnetism in silicene *Eur. Phys. J. B* **85** 363
- [89] Koshino M, Morimoto T and Sato M 2014 Topological zero modes and Dirac points protected by spatial symmetry and chiral symmetry *Phys. Rev. B* **90** 115207
- [90] Aoki H and Dresselhaus M S (ed) 2013 *Physics of Graphene* (London: Springer)
- [91] Ezawa M 2011 Compact merons and skyrmions in thin chiral magnetic films *Phys. Rev. B* **83** 100408
- [92] Moon K, Mori H, Yang K, Girvin S M, MacDonald A H, Zheng L, Yoshioka D and Zhang S C 1995 Spontaneous interlayer coherence in double-layer quantum Hall systems: charged vortices and Kosterlitz–Thouless phase transitions *Phys. Rev. B* **51** 5138
- [93] Petković A and Milovanović M V 2007 Fractionalization into merons in quantum dots *Phys. Rev. Lett.* **98** 066808
- [94] Krishnan A, Dujardin E, Treacy M M J, Hugdahl J, Lynum S and Ebbesen T W 1997 Graphitic cones and the nucleation of curved carbon surfaces *Nature* **338** 451
- [95] DiVincenzo D P and Mele E J 1984 Self-consistent effective-mass theory for intralayer screening in graphite intercalation compounds *Phys. Rev. B* **29** 1685
- [96] Sheng L, Sheng D N, Ting C S and Haldane F D M 2005 Nondissipative spin Hall effect via quantized edge transport *Phys. Rev. Lett.* **95** 136602
- [97] Sheng D N, Weng Z Y, Sheng L and Haldane F D M 2006 Quantum spin-Hall effect and topologically invariant chern numbers *Phys. Rev. Lett.* **97** 036808
- [98] Fu L and Kane C L 2007 Topological insulators with inversion symmetry *Phys. Rev. B* **76** 045302
- [99] Cahangirov S, Topsakal M, Aktürk E, Şahin H and Ciraci S 2009 Two- and one-dimensional honeycomb structures of silicon and germanium *Phys. Rev. Lett.* **102** 236804
- [100] Aufray B, Kara A, Vizzini S, Oughaddou H, Léandri C, Ealet B and Lay G L 2010 Graphene-like silicon nanoribbons on Ag(110): a possible formation of silicene *Appl. Phys. Lett.* **96** 183102
- [101] Padova P E *et al* 2010 Evidence of graphene-like electronic signature in silicene nanoribbons *Appl. Phys. Lett.* **96** 261905
- [102] Lalmi B, Oughaddou H, Enriquez H, Kara A, Vizzini S, Ealet B and Aufray B 2010 Epitaxial growth of a silicene sheet *Appl. Phys. Lett.* **97** 223109
- [103] Ma Y, Dai Y, Niu C and Huang B 2012 Halogenated two-dimensional germanium: candidate materials for being of quantum spin Hall state *J. Mater. Chem.* **22** 12587
- [104] Padilha J E, Seixas L, Pontes R B, da Silva A J R and Fazzio A 2013 Quantum spin Hall effect in a disordered hexagonal Si_xGe_{1-x} alloy *Phys. Rev. B* **88** 201106
- [105] Zhao M and Zhang R 2014 Two-dimensional topological insulators with binary honeycomb lattices: SiC₃ silicene and its analogs *Phys. Rev. B* **89** 195427
- [106] Liu C-C, Feng W and Yao Y 2011 Quantum spin Hall effect and enhanced magnetic response by spin-orbit coupling *Phys. Rev. Lett.* **107** 076802
- [107] An X-T, Zhang Y-Y, Liu J-J and Li S-S 2013 Quantum spin Hall effect induced by electric field in silicene *Appl. Phys. Lett.* **102** 043113

- [108] Ezawa M 2012 A topological insulator and helical zero mode in silicene under an inhomogeneous electric field *New J. Phys.* **14** 033003
- [109] Drummond N D, Zólyomi V and Fal'ko V I 2012 Electrically tunable band gap in silicene *Phys. Rev. B* **85** 075423
- [110] Tahir M, Manchon A, Sabeen K and Schwingenschlögl U 2013 Quantum spin/valley Hall effect and topological insulator phase transitions in silicene *Appl. Phys. Lett.* **102** 162412
- [111] Huang Z Q, Hsu C H, Chuang F C, Liu Y T, Lin H, Su W S, Ozolins V and Bansil A 2014 Strain driven topological phase transitions in atomically thin films of group IV and V elements in the honeycomb structures *New J. Phys.* **16** 105018
- [112] Ma Y, Dai Y, Wei W, Huang B and Whangbo M-H 2014 Strain-induced quantum spin Hall effect in methyl-substituted germanane GeCH₃ *Sci. Rep.* **4** 7297
- [113] McCann E and Koshino M 2013 The electronic properties of bilayer graphene *Rep. Prog. Phys.* **76** 056503
- [114] MacDonald A H, Jung J and Zhang F 2012 Pseudospin order in monolayer, bilayer and double-layer graphene *Phys. Scr.* **T146** 014012
- [115] Kou L, Hu F, Yan B, Frauenheim T and Chen C 2014 Opening a band gap without breaking lattice symmetry: a new route toward robust graphene-based nanoelectronics *Nanoscale* **6** 7474
- [116] Marchenko D, Varykhalov A, Scholz M R, Bihlmayer G, Rashba E I, Rybkin A, Shikin A M and Rader O 2012 Giant Rashba splitting in graphene due to hybridization with gold *Nat. Commun.* **3** 1232
- [117] Dedkov Y S, Fonin M, Rüdiger U and Laubschat C 2008 Rashba effect in the graphene/Ni(1 1 1) system *Phys. Rev. Lett.* **100** 107602
- [118] Varykhalov A, Saánchez-Barriga J, Shikin A M, Biswas C, Vescovo E, Rybkin A, Marchenko D and Rader O 2008 Electronic and magnetic properties of quasifree-standing graphene on Ni *Phys. Rev. Lett.* **101** 157601
- [119] Qiao Z, Li X, Tse W-K, Jiang H, Yao Y and Niu Q 2013 Topological phases in gated bilayer graphene: effects of Rashba spin-orbit coupling and exchange field *Phys. Rev. B* **87** 125405
- [120] Li J, Martin I, Büttiker M and Morpurgo A F 2012 Marginal topological properties of graphene—a comparison with topological insulators *Phys. Scr.* **T146** 014021
- [121] Knez I, Du R R and Sullivan G 2012 Andreev reflection of helical edge modes in InAs/GaSb quantum spin Hall insulator *Phys. Rev. Lett.* **109** 186603
- [122] Du L, Knez I, Sullivan G and Du R R 2015 Robust helical edge transport in gated InAs/GaSb bilayers *Phys. Rev. Lett.* **114** 096802
- [123] Zhang H, Xu Y, Wang J, Chang K and Zhang S C 2014 Quantum spin Hall and quantum anomalous Hall states realized in junction quantum wells *Phys. Rev. Lett.* **112** 216803
- [124] Liu C, Hughes T L, Qi X L, Wang K and Zhang S C 2008 Quantum spin Hall effect in inverted type-II semiconductors *Phys. Rev. Lett.* **100** 236601
- [125] Knez I, Du R R and Sullivan G 2011 Evidence for helical edge modes in inverted InAs/GaSb quantum wells *Phys. Rev. Lett.* **107** 136603
- [126] Nowack K C *et al* 2013 Imaging currents in HgTe quantum wells in the quantum spin Hall regime *Nat. Mater.* **12** 787
- [127] König M, Hartmut Buhmann H, Molenkamp L W, Hughes T, Liu C X, Qi X L and Zhang S C 2008 The quantum spin Hall effect: theory and experiment *J. Phys. Soc. Japan* **77** 031007
- [128] Novik E G, Pfeuffer-Jeschke A, Jungwirth T, Latussek V, Becker C R, Landwehr G, Buhmann H and Molenkamp L W 2005 Band structure of semimagnetic Hg_{1-y}Mn_yTe quantum wells *Phys. Rev. B* **72** 035321
- [129] Murakami S, Iso S, Avishai Y, Onoda M and Nagaosa N 2007 Tuning phase transition between quantum spin Hall and ordinary insulating phases *Phys. Rev. B* **76** 205304
- [130] Miao M S, Yan Q, Van de Walle C G, Lou W K, Li L L and Chang K 2012 Polarization-driven topological insulator transition in a GaN/InN/GaN quantum well *Phys. Rev. Lett.* **109** 186803
- [131] Zhang D, Lou W, Miao M, Zhang S C and Chang K 2013 Interface-induced topological insulator transition in GaAs/Ge/GaAs quantum wells *Phys. Rev. Lett.* **111** 156402
- [132] Jiang H, Qiao Z, Liu H, Shi J and Niu Q 2012 Stabilizing topological phases in graphene via random adsorption *Phys. Rev. Lett.* **109** 116803
- [133] Sutter E, Albrecht P, Wang B, Bocquet M L, Wu L, Zhu Y and Sutter P 2011 Arrays of Ru nanoclusters with narrow size distribution templated by monolayer graphene on Ru *Surf. Sci.* **605** 1676
- [134] Cresti A, Tuan D V, Soriano D, Cummings A W and Roche S 2014 Multiple quantum phases in graphene with enhanced spin-orbit coupling *Phys. Rev. Lett.* **113** 246603
- [135] Hu J, Alicea J, Wu R and Franz M 2012 Giant topological insulator gap in graphene with 5d adatoms *Phys. Rev. Lett.* **109** 266801
- [136] Li Y, Tang P, Chen P, Wu J, Gu B-L, Fang Y, Zhang S B and Duan W 2013 Topological insulators in transition-metal intercalated graphene: the role of d electrons in significantly increasing the spin-orbit gap *Phys. Rev. B* **87** 245127
- [137] Acosta C M, Lima M P, Miwa R H, da Silva A J R and Fazzio A 2014 *Phys. Rev. B* **89** 155438
- [138] Kou L, Hu F, Yan B, Wehling T, Felser C, Frauenheim T and Chen C 2015 Proximity enhanced quantum spin Hall state in graphene *Carbon* **87** 418
- [139] Kou L, Yan B, Hu F, Wu S-C, Wehling T O, Felser C, Chen C and Frauenheim T 2013 Graphene-based topological insulator with an intrinsic bulk band gap above room temperature *Nano Lett.* **13** 6251
- [140] Kou L, Wu S C, Felser C, Frauenheim T, Chen C and Yan B 2014 Robust 2D topological insulators in van der Waals heterostructures *ACS Nano* **10** 10448
- [141] Jin K-H and Jhi S-H 2013 Proximity-induced giant spin-orbit interaction in epitaxial graphene on a topological insulator *Phys. Rev. B* **87** 075442
- [142] Liu W, Peng X, Wei X, Yang H, Stocks G M and Zhong J 2013 Surface and substrate induced effects on thin films of the topological insulators Bi₂Se₃ and Bi₂Te₃ *Phys. Rev. B* **87** 205315
- [143] Zhang J, Triola C and Rossi E 2014 Proximity effect in graphene-topological-insulator heterostructures *Phys. Rev. Lett.* **112** 096802
- [144] Wang J, Deng S, Liu Z and Liu Z 2015 The rare two-dimensional materials with Dirac cones *Natl. Sci. Rev.* **2** 22–39
- [145] Wehling T O, Black-Schaffer A M and Balatsky A V 2014 Dirac materials *Adv. Phys.* **63** 1–76
- [146] Wang Z F, Liu Z and Liu F 2013 Organic topological insulators in organometallic lattices *Nat. Commun.* **4** 1471
- [147] Kambe T, Sakamoto R, Hoshiko K, Takada K, Miyachi M, Ryu J H, Sasaki S, Kim J, Nakazato K, Takata M and Nishihara H 2013 π-conjugated nickel bis(dithiolene) complex nanosheet *J. Am. Chem. Soc.* **135** 2462
- [148] Sheberla D, Sun L, Blood-Forsythe M A, Er S, Wade C R, Brozek C K, Aspuru-Guzik A and Dincă M 2014 High electrical conductivity in Ni₃(2,3,6,7,10,11-hexaminotriphenylene)₂, a semiconducting metal-organic graphene analogue *J. Am. Chem. Soc.* **136** 8859

- [149] Wang Z F, Su N and Liu F 2013 Prediction of a two-dimensional organic topological insulator *Nano Lett.* **13** 2842
- [150] Zhao B, Zhang J, Feng W, Yao Y and Yang Z 2014 Quantum spin Hall and Z_2 metallic states in an organic material *Phys. Rev. B* **90** 201403
- [151] Wang A, Zhang X and Zhao M 2014 Topological insulator states in a honeycomb lattice of s-triazines *Nanoscale* **6** 11157
- [152] Zhao M, Dong W and Wang A 2013 Two-dimensional carbon topological insulators superior to graphene *Sci. Rep.* **3** 3532
- [153] Polini M, Guinea F, Lewenstein M, Manoharan H C and Pellegrini V 2013 Artificial honeycomb lattices for electrons, atoms and photons *Nat. Nano.* **8** 625
- [154] Kalesaki E, Delerue C, Smith C M, Beugeling W, Allan G and Vanmaekelbergh D 2014 Dirac cones, topological edge states and nontrivial flat bands in two-dimensional semiconductors with a honeycomb nanogeometry *Phys. Rev. X* **4** 011010
- [155] Beugeling W, Kalesaki E, Delerue C, Niquet Y M, Vanmaekelbergh D and Smith C M 2015 Topological states in multi-orbital HgTe honeycomb lattices *Nat. Commun.* **6** 6316
- [156] Tarruell L, Greif D, Uehlinger T, Jotzu G and Esslinger T 2012 Creating, moving and merging Dirac points with a Fermi gas in a tunable honeycomb lattice *Nature* **483** 302
- [157] Jotzu G, Messer M, Desbuquois R, Lebrat M, Uehlinger T, Greif D and Esslinger T 2014 Experimental realization of the topological Haldane model with ultracold fermions *Nature* **515** 237
- [158] Hwang H Y, Iwasa Y, Kawasaki M, Keimer B, Nagaosa N and Tokura Y 2012 Emergent phenomena at oxide interfaces *Nat. Mater.* **11** 103
- [159] Xiao D, Zhu W, Ran Y, Nagaosa N and Okamoto S 2011 Interface engineering of quantum Hall effects in digital transition metal oxide heterostructures *Nat. Commun.* **2** 596
- [160] Okamoto S, Zhu W, Nomura Y, Arita R, Xiao D and Nagaosa N 2014 Correlation effects in (111) bilayers of perovskite transition-metal oxides *Phys. Rev. B* **89** 195121
- [161] Qian X, Liu J, Fu L and Li J 2014 Quantum spin Hall effect in two-dimensional transition metal dichalcogenides *Science* **346** 1344
- [162] Lu Y *et al* 2015 Topological properties determined by atomic buckling in self-assembled ultrathin Bi(110) *Nano Lett.* **15** 80
- [163] Weng H, Dai X and Fang Z 2014 Transition-metal pentatelluride ZrTe₅ and HfTe₅: a paradigm for large-gap quantum spin Hall insulators *Phys. Rev. X* **4** 011002
- [164] Liu Q, Zhang X, Abdalla L B, Fazzio A and Zunger A 2015 Switching a normal insulator into a topological insulator via electric field with application to phosphorene *Nano Lett.* **15** 1222
- [165] Zhu Z and Tománek D 2014 Semiconducting layered blue phosphorus—a computational study *Phys. Rev. Lett.* **112** 176802
- [166] Kamal C and Ezawa M 2015 Arsenene: 2D buckled and puckered honeycomb arsenic systems *Phys. Rev. B* **91** 085423
- [167] Hofmann Ph 2006 The surfaces of bismuth: structural and electronic properties *Prog. Surf. Sci.* **81** 191
- [168] Mönig H, Sun J, Koroteev Yu M, Bihlmayer G, Wells J, Chulkov E V, Pohl K and Hofmann Ph 2005 *Phys. Rev. B* **72** 085410
- [169] Bian G, Wang X, Liu Y, Miller T and Chiang T C 2012 Interfacial protection of topological surface states in ultrathin Sb films *Phys. Rev. Lett.* **108** 176401
- [170] Murakami S 2006 Quantum spin Hall effect and enhanced magnetic response by spin-orbit coupling *Phys. Rev. Lett.* **97** 236805
- [171] Koroteev Y M, Bihlmayer G, Chulkov E V and Blügel S 2008 First-principles investigation of structural and electronic properties of ultrathin Bi films *Phys. Rev. B* **77** 045428
- [172] Li X, Liu H, Jiang H, Wang F and Feng J 2014 Structure of the (111) surface of bismuth: LEED analysis and first-principles calculations *Phys. Rev. B* **90** 165412
- [173] Liu Z, Liu C-X, Wu Y-S, Duan W-H, Liu F and Wu J 2011 Stable nontrivial Z_2 topology in ultrathin Bi (111) films: a first-principles study *Phys. Rev. Lett.* **107** 136805
- [174] Wada M, Murakami S, Freimuth F and Bihlmayer G 2011 Localized edge states in 2D topological insulators localized edge states in 2D topological insulators: ultrathin Bi films *Phys. Rev. B* **83** 121310
- [175] Lima E N and Schmidt T M 2015 Topological phase driven by confinement effects in Bi bilayers *Phys. Rev. B* **91** 075432
- [176] Wang D, Chen L, Liu H and Wang X 2013 Electronic structures and topological properties of Bi(111) ultrathin films *J. Phys. Soc. Japan* **82** 094712
- [177] Wang Z F, Chen L and Liu F 2014 Tuning topological edge states of Bi(111) bilayer film by edge adsorption *Nano Lett.* **14** 2879
- [178] Chen L, Cui G, Zhang P, Wang X, Liu H and Wang D 2014 Edge state modulation of bilayer Bi nanoribbons by atom adsorption *Phys. Chem. Chem. Phys.* **16** 17206
- [179] Takayama A, Sato T, Souma S, Oguchi T and Takahashi T 2015 One-dimensional edge states with giant spin splitting in a Bismuth thin film *Phys. Rev. Lett.* **114** 066402
- [180] Zhou M, Ming W, Liu Z, Wang Z, Li P and Liu F 2014 Epitaxial growth of large-gap quantum spin Hall insulator on semiconductor surface *Proc. Natl Acad. Sci.* **111** 14378
- [181] Zhou M, Ming W, Liu Z, Wang Z, Yao Y and Liu F 2014 Formation of quantum spin Hall state on Si surface and energy gap scaling with strength of spin orbit coupling *Sci. Rep.* **4** 7102
- [182] Hsu C H, Huang Z Q, Chuang F C, Kuo C C, Liu Y T, Lin H and Bansil A 2015 The nontrivial electronic structure of Bi:Sb honeycombs on SiC(0001) *New J. Phys.* **17** 025005
- [183] Huang Z Q, Chou B H, Hsu C H, Chuang F C, Lin H and Bansil A 2014 Tunable topological electronic structure of silicene on a semiconducting Bi/Si(111)- $\sqrt{3} \times \sqrt{3}$ substrate *Phys. Rev. B* **90** 245433
- [184] Huang Z-Q, Chuang F-C, Hsu C-H, Liu Y-T, Chang H-R, Lin H and Bansil A 2013 Nontrivial topological electronic structures in a single Bi(111) bilayer on different substrates: a first-principles study *Phys. Rev. B* **88** 165301
- [185] Sabater C, Gosálbez-Martínez D, Fernández-Rossier J, Rodrigo J G, Untiedt C and Palacios J J 2013 Topologically protected quantum transport in locally exfoliated Bismuth at room temperature *Phys. Rev. Lett.* **110** 176802
- [186] Hirahara T, Bihlmayer G, Sakamoto Y, Yamada M, Miyazaki H, Kimura S, Blügel S and Hasegawa S 2011 Interfacing 2D and 3D topological insulators: Bi(111) bilayer on Bi₂Te₃ *Phys. Rev. Lett.* **107** 166801
- [187] Yang F *et al* 2012 Spatial and energy distribution of topological edge states in single Bi(111) bilayer *Phys. Rev. Lett.* **109** 016801
- [188] Kim S H, Jin K-H, Park J, Kim J S, Jhi S-H, Kim T-H and Yeom H W 2014 Edge and interfacial states in a two-dimensional topological insulator: Bi(111) bilayer on Bi₂Te₂Se *Phys. Rev. B* **89** 155436

- [189] Drozdov I K, Alexandradinata A, Jeon S, Nadj-Perge S, Ji H, Cava R J, Bernevig B A and Yazdani A 2014 One-dimensional topological edge states of Bismuth bilayers *Nat. Phys.* **10** 664
- [190] Zhang P, Liu Z, Duan W, Liu F and Wu J 2012 Topological and electronic transitions in a Sb(1 1 1) nanofilm: the interplay between quantum confinement and surface effect *Phys. Rev. B* **85** 201410
- [191] Wang D, Chen L, Liu H and Wang X 2013 Topological phase transitions in Sb(1 1 1) films driven by external strain and electric field *Europhys. Lett.* **104** 57011
- [192] Şahin H, Cahangirov S, Topsakal M, Bekaroglu E, Akturk E, Senger R T and Ciraci S 2009 Monolayer honeycomb structures of group-IV elements and III-V binary compounds *Phys. Rev. B* **80** 155453
- [193] Zhuang H L, Singh A K and Hennig R G 2013 Computational discovery of single-layer III-V materials *Phys. Rev. B* **87** 165415
- [194] Zhao M, Chen X, Li L and Zhang X 2015 Driving a GaAs film to a large-gap topological insulator by tensile strain *Sci. Rep.* **5** 8441
- [195] Chuang F C, Yao L Z, Huang Z Q, Liu Y T, Hsu C H, Das T, Lin H and Bansil A 2014 Prediction of large-gap two-dimensional topological insulators consisting of bilayers of group III elements with Bi *Nano Lett.* **14** 2505
- [196] Li L, Zhang X, Chen X and Zhao M 2015 Giant topologically nontrivial band gaps in chloridized gallium bismuthide *Nano Lett.* **15** 1296
- [197] Li X, Dai Y, Ma Y, Wei W, Yu L and Huang B 2015 Prediction of large-gap quantum spin hall insulator and Rashba-Dresselhaus effect in two-dimensional g-TIA ($A = N, P, As, and Sb$) monolayer films *Nano Res.* **9** 2954–62
- [198] Zhou J-J, Feng W, Liu C-C, Guan S and Yao Y 2014 Large-gap quantum Spin hall insulator in single layer Bismuth monobromide Bi_4Br_4 *Nano Lett.* **14** 4767
- [199] Zhou J-J, Feng W, Liu G-B and Yao Y 2015 Topological edge states in single- and multi-layer Bi_4Br_4 *New J. Phys.* **17** 015004
- [200] Luo W and Xiang H 2015 Room temperature QSHE with a buckled square lattice *Nano Lett.* **15** 3230
- [201] Bianco E, Butler S, Jiang S, Restrepo O D, Windl W and Goldberger J E 2013 Stability and exfoliation of germanane: a Germanium graphane analogue *ACS Nano* **7** 4414
- [202] Chou B-H, Huang Z-Q, Hsu C-H, Chuang F-C, Liu Y-T, Lin H and Bansil A 2014 Hydrogenated ultra-thin tin films predicted as 2D topological insulators *New J. Phys.* **16** 115008
- [203] Si C, Liu J, Xu Y, Wu J, Gu B-L and Duan W 2014 Functionalized germanene as a prototype of large-gap two-dimensional topological insulators *Phys. Rev. B* **89** 115429
- [204] Seixas L, Padilha J E and Fazzio A 2014 Quantum spin Hall effect on germanene nanorod embedded in completely hydrogenated germanene *Phys. Rev. B* **89** 195403
- [205] Tang P, Chen P, Cao W, Huang H, Cahangirov C, Xian L, Xu Y, Zhang S, Duan W and Rubio A 2014 Stable 2D dumbbell stanene: a quantum spin Hall insulator *Phys. Rev. B* **90** 121408
- [206] Niu C, Bihlmayer G, Zhang H, Wortmann D, Blügel S and Mokrousov Y 2015 Functionalized bismuth films: giant gap quantum spin Hall and valley-polarized quantum anomalous Hall states *Phys. Rev. B* **91** 041303
- [207] Liu C-C, Guan S, Song Z, Yang S A, Yang J and Yao Y 2014 Low-energy effective Hamiltonian for giant-gap quantum spin Hall insulators in honeycomb X -hydride/halide ($X = N, Bi$) monolayers *Phys. Rev. B* **90** 085431
- [208] Song Z, Liu C-C, Yang J, Han J, Ye M, Fu B, Yang Y, Niu Q, Lu J and Yao Y 2014 Quantum spin Hall insulators and quantum valley Hall insulators of BiX/SbX ($X \& equals;$; H, F, Cl and Br) monolayers with a record bulk band gap *NPG Asia Mater.* **6** e147
- [209] Jin K-H and Jhi S-H 2015 Quantum anomalous Hall and quantum spin-Hall phases in flattened Bi and Sb bilayers *Sci. Rep.* **5** 8426
- [210] Ma Y, Dai Y, Kou L, Frauenheim T and Heine T 2015 Robust 2D topological insulators in methyl-functionalized Bismuth, antimony and lead bilayer films *Nano Lett.* **15** 1083
- [211] Zhang G-F, Li Y and Wu C 2014 Honeycomb lattice with multiorbital structure: topological and quantum anomalous Hall insulators with large gaps *Phys. Rev. B* **90** 075114
- [212] Wang D, Chen L, Liu H, Wang X, Cui G, Zhang P, Zhao D and Ji S 2015 Topological states modulation of Bi and Sb thin films by atomic adsorption *Phys. Chem. Chem. Phys.* **17** 3577
- [213] Li J, Chu R L, Jain J K and Shen S Q 2009 Topological Anderson insulator *Phys. Rev. Lett.* **102** 136806
- [214] Jiang H, Wang L, Sun Q F and Xie X C 2009 Numerical study of the topological Anderson insulator in $HgTe/CdTe$ quantum wells *Phys. Rev. B* **80** 165316
- [215] Prodan E 2011 Three-dimensional phase diagram of disordered $HgTe/CdTe$ quantum spin-Hall wells *Phys. Rev. B* **83** 195119
- [216] Groth C W, Wimmer M, Akhmerov A R, Tworzydlo J and Beenakker C W J 2009 Theory of the topological Anderson insulator *Phys. Rev. Lett.* **103** 196805
- [217] Chen L, Liu Q, Lin X, Zhang X and Jiang X 2012 Disorder dependence of helical edge states in $HgTe/CdTe$ quantum wells *New J. Phys.* **14** 043028
- [218] Zhang Y Y, Chu R L, Zhang F C and Shen S Q 2012 Localization and mobility gap in the topological Anderson insulator *Phys. Rev. B* **85** 035107
- [219] Yamakage A, Nomura K, Imura K I, Kuramoto Y 2012 Z_2 topological Anderson insulator *J. Phys.: Conf. Ser.* **400** 042070
- [220] Zhang Y Y and Shen S Q 2013 Algebraic and geometric mean density of states in topological Anderson insulators *Phys. Rev. B* **88** 195145
- [221] Xu D, Qi J, Liu J, Sacksteder I V, Xie X C and Jiang H 2012 Phase structure of the topological Anderson insulator *Phys. Rev. B* **85** 195140
- [222] Zhang Y Y, Shen M, An X T, Sun Q F, Xie X C, Chang K and Li S S 2014 Coexistence and decoupling of bulk and edge states in disordered two-dimensional topological insulators *Phys. Rev. B* **90** 054205
- [223] Xing Y, Zhang L and Wang J 2011 Topological Anderson insulator phenomena *Phys. Rev. B* **84** 035110
- [224] Lv S H, Song J and Li Y X 2013 Topological Anderson insulator induced by inter-cell hopping disorder *J. Appl. Phys.* **114** 183710
- [225] Song J, Liu H, Hua Jiang H, Sun Q F and Xie X C 2012 Dependence of topological Anderson insulator on the type of disorder *Phys. Rev. B* **85** 195125
- [226] Yamakage A, Nomura K, Imura K I, Kuramoto Y 2011 Disorder-induced multiple transition involving Z_2 topological insulator *J. Phys. Soc. Japan* **80** 053703
- [227] Girschik A, Libisch F and Rotter S 2013 Topological insulator in the presence of spatially correlated disorder *Phys. Rev. B* **88** 014201
- [228] Li W, Zang J and Jiang Y 2011 Size effects on transport properties in topological Anderson insulators *Phys. Rev. B* **84** 033409
- [229] Yamakage A, Nomura K, Imura K I and Kuramoto Y 2013 Criticality of the metal-topological insulator transition driven by disorder *Phys. Rev. B* **87** 205141
- [230] Cao J and Xiong S J 2013 Topological phase transition in a graphene system with a coexistence of Coulomb interaction, staggered potential and intrinsic spin-orbit coupling *Phys. Rev. B* **88** 085409

- [231] Rachel S and Hur K L 2010 Topological insulators and Mott physics from the Hubbard interaction *Phys. Rev. B* **82** 075106
- [232] Yang Y, Xu Z, Sheng L, Wang B, Xin D Y and Sheng D N 2011 Time-reversal-symmetry-broken quantum spin Hall effect *Phys. Rev. Lett.* **107** 066602
- [233] Abanin D A, Lee P A and Levitov L S 2006 Spin-filtered edge states and quantum Hall effect in graphene *Phys. Rev. Lett.* **96** 176803
- [234] Abanin D A, Novoselov K S, Zeitler U, Lee P A, Geim A K and Levitov L S 2007 Dissipative quantum Hall effect in graphene near the Dirac point *Phys. Rev. Lett.* **98** 196806
- [235] Ezawa M 2013 High spin-Chern insulators with magnetic order *Sci. Rep.* **3** 3435
- [236] Ostahie B, Niță M and Aldea A 2014 Topological properties of the mesoscopic graphene plaquette: quantum spin Hall effect due to spin imbalance *Phys. Rev. B* **89** 165412
- [237] Beugeling W, Goldman N and Smith C M 2012 Topological phases in a two-dimensional lattice: magnetic field versus spin-orbit coupling *Phys. Rev. B* **86** 075118
- [238] Liu C X, Qi X L, Dai X, Fang Z and Zhang S C 2008 Quantum anomalous Hall effect in $Hg_{1-y}Mn_yTe$ quantum wells *Phys. Rev. Lett.* **101** 146802
- [239] Wang Q Z, Liu X, Zhang H J, Samarth N, Zhang S C and Liu C X 2014 Quantum anomalous Hall effect in magnetically doped InAs/GaSb quantum wells *Phys. Rev. Lett.* **113** 147201
- [240] Jin H, Im J and Freeman A J 2011 Topological and magnetic phase transitions in Bi_2Se_3 thin films with magnetic impurity *Phys. Rev. B* **84** 134408
- [241] Xia Y *et al* 2009 Observation of a large-gap topological-insulator class with a single Dirac cone on the surface *Nat. Phys.* **5** 389
- [242] Hsieh D *et al* 2009 A tunable topological insulator in the spin helical Dirac transport regime *Nature* **460** 1101
- [243] Biswas R R and Balatsky A V 2010 Impurity-induced states on the surface of three-dimensional topological insulators *Phys. Rev. B* **81** 233405
- [244] He K, Ma X C, Chen X, Lü L, Wang Y Y and Xue Q K 2013 From magnetically doped topological insulator to the quantum anomalous Hall effect *Chin. Phys. B* **22** 067305
- [245] Lu H Z, Zhao A and Shen S H 2013 Quantum transport in magnetic topological insulator thin films *Phys. Rev. Lett.* **111** 146802
- [246] Cheng S G 2014 The quantum anomalous Hall effect in a topological insulator thin film the role of magnetic disorder *Europhys. Lett.* **105** 57004
- [247] Niu C, Dai Y, Yu L, Guo M, Ma Y and Huang B 2011 Quantum anomalous Hall effect in doped ternary chalcogenide topological insulators $TlBiTe_2$ and $TlBiSe_2$ *Appl. Phys. Lett.* **99** 142502
- [248] Niu C, Buhl P M, Bihlmayer G, Wortmann D, Blügel S and Mokrousov Y 2015 Topological crystalline insulator and quantum anomalous Hall states in IV-VI-based monolayers and their quantum wells *Phys. Rev. B* **91** 201401
- [249] Zhang F, Li X, Feng J, Kane C L and Mele E J 2013 Zeeman field-tuned transitions for surface Chern insulators (arXiv:1309.7682v1)
- [250] Fang C, Gilbert M J and Bernevig B A 2014 Large-Chern-number quantum anomalous Hall effect in thin-film topological crystalline insulators *Phys. Rev. Lett.* **112** 046801
- [251] Qi S, Qiao Z, Deng X, Cubuk E D, Chen H, Zhu W, Kaxiras E, Zhang S B, Xu X and Zhang Z 2015 High-temperature quantum anomalous Hall effect in $n-p$ codoped topological insulators (arXiv:1507.03218v1)
- [252] Chen T W, Xiao Z R, Chiou D W and Guo G Y 2011 High Chern number quantum anomalous Hall phases in single-layer graphene with Haldane orbital coupling *Phys. Rev. B* **84** 165453
- [253] Qiao Z, Jiang H, Li X, Yao Y and Niu Q 2012 Microscopic theory of quantum anomalous Hall effect in graphene *Phys. Rev. B* **85** 115439
- [254] Zhang Z Y 2011 The quantum anomalous Hall effect in kagomé lattices *J. Phys.: Condens. Matter* **23** 365801
- [255] Venderbos J W F, Daghofer M, van den Brink J and Kumar S 2012 Switchable quantum anomalous Hall state in a strongly frustrated lattice magnet *Phys. Rev. Lett.* **109** 166405
- [256] Chen M and Wan S 2012 The quantum anomalous Hall effect on a star lattice with spin-orbit coupling and an exchange field *J. Phys.: Condens. Matter* **24** 325502
- [257] Guo X, Ren X, Guo G and Peng J 2014 Quantum anomalous Hall effect on a square lattice with spin-orbit couplings and an exchange field *Can. J. Phys.* **92** 420
- [258] Eelbo T, Waśniowska M, Thakur P, Gyamfi M, Sachs B, Wehling T O, Forti S, Starke U, Tieg C, Lichtenstein A I and Wiesendanger R 2013 Adatoms and clusters of $3d$ transition metals on graphene: electronic and magnetic configurations *Phys. Rev. Lett.* **110** 136804
- [259] Hu J, Zhu Z and Wu R 2015 Chern half metals: a new class of topological materials to realize the quantum anomalous Hall effect *Nano Lett.* **15** 2074
- [260] Ren Y, Deng X, Qiao Z, Li C, Jung J, Zeng C, Zhang Z and Niu Q 2015 Single-valley engineering in graphene superlattices *Phys. Rev. B* **91** 245415
- [261] Chen H, Niu Q, Zhang Z and MacDonald A H 2013 Gate-tunable exchange coupling between cobalt clusters on graphene *Phys. Rev. B* **87** 144410
- [262] Zhang J, Zhao B, Yao Y and Yang Z 2015 Quantum anomalous Hall effect in graphene-based heterostructure *Sci. Rep.* **5** 10629
- [263] Qi S, Chen H, Xu X and Zhang Z 2013 Diluted ferromagnetic graphene by compensated n-p codoping *Carbon* **61** 609
- [264] Zhang X and Zhao M 2015 Prediction of quantum anomalous Hall effect on graphene nanomesh *RSC Adv.* **5** 9875
- [265] Ezawa M 2012 Valley-polarized metals and quantum anomalous Hall effect in silicene *Phys. Rev. Lett.* **109** 055502
- [266] Pan H, Li Z, Liu C C, Zhu G, Qiao Z and Yao Y 2014 Valley-polarized quantum anomalous Hall effect in silicene *Phys. Rev. Lett.* **112** 106802
- [267] Pan H, Li X, Jiang H, Yao Y and Yang S A 2015 Valley-polarized quantum anomalous Hall phase and disorder-induced valley-filtered chiral edge channels *Phys. Rev. B* **91** 045404
- [268] Kaloni T P, Singh N and Schwingenschlögl U 2014 Prediction of a quantum anomalous Hall state in Co-decorated silicene *Phys. Rev. B* **89** 035409
- [269] Yang M, Zhang X L and Liu W M 2015 Tunable topological quantum states in three- and two-dimensional materials *Front. Phys.* **10** 108102
- [270] Zhang X L, Liu L F and Liu W M 2013 Quantum anomalous Hall effect and tunable topological states in $3d$ transition metals doped silicene *Sci. Rep.* **3** 2908
- [271] Zhang J, Zhao B and Yang Z 2013 Abundant topological states in silicene with transition metal adatoms *Phys. Rev. B* **88** 165422
- [272] Zhang H, Freimuth F, Bihlmayer G, Blügel S and Mokrousov Y 2012 Topological phases of $Bi(1\bar{1}\bar{1})$ bilayer in an external exchange field *Phys. Rev. B* **86** 035104
- [273] Zhang H, Freimuth F, Bihlmayer G, Ležaić M, Blügel S and Mokrousov Y 2013 Engineering quantum anomalous Hall phases with orbital and spin degrees of freedom *Phys. Rev. B* **87** 205132

- [274] Huang S M, Lee S T and Mou C Y 2014 Ferromagnetism and quantum anomalous Hall effect in one-side-saturated buckled honeycomb lattices *Phys. Rev. B* **89** 195444
- [275] Wu S C, Shan G and Yan B 2014 Prediction of Near-room-temperature quantum anomalous Hall effect on honeycomb materials *Phys. Rev. Lett.* **113** 256401
- [276] Liu C C, Zhou J J and Yao Y 2015 Valley-polarized quantum anomalous Hall phases and tunable topological phase transitions in half-hydrogenated Bi honeycomb monolayers *Phys. Rev. B* **91** 165430
- [277] Dudarev A M, Diener R B, Carusotto I and Niu Q 2004 Spin-orbit coupling and berry phase with ultracold atoms in 2D optical lattices *Phys. Rev. Lett.* **92** 153005
- [278] Shao L B, Zhu S L, Sheng L, Xing D Y and Wang Z D 2008 Realizing and detecting the quantum Hall effect without Landau levels by using ultracold atoms *Phys. Rev. Lett.* **101** 246810
- [279] Wu C 2008 Orbital analogue of the quantum anomalous Hall effect in *p*-band systems *Phys. Rev. Lett.* **101** 186807
- [280] Liu X J, Liu X, Wu C and Sinova J 2010 Quantum anomalous Hall effect with cold atoms trapped in a square lattice *Phys. Rev. A* **81** 033622
- [281] Uehlinger T, Jotzu G, Messer M, Greif D, Hofstetter W, Bissbort U and Esslinger T 2013 Artificial graphene with tunable interactions *Phys. Rev. Lett.* **111** 185307
- [282] Cocks D, Orth P P, Rachel S, Buchhold M, Hur K L and Hofstetter W 2012 Time-reversal-invariant Hofstadter-Hubbard Model with ultracold fermions *Phys. Rev. Lett.* **109** 205303
- [283] Wang L, Hung H H and Troyer M 2014 Topological phase transition in the Hofstadter-Hubbard model *Phys. Rev. B* **90** 205111
- [284] Goldman N, Satija I, Nikolic P, Bermudez A, Martin-Delgado M A, Lewenstein M and Spielman I B 2010 Realistic time-reversal invariant topological insulators with neutral atoms *Phys. Rev. Lett.* **105** 255302
- [285] Befi B and Cooper N R 2011 \mathbb{Z}_2 Topological insulators in ultracold atomic gases *Phys. Rev. Lett.* **107** 145301
- [286] Zhou M, Liu Z, Ming W, Wang Z and Liu F 2014 sd^2 graphene: kagome band in a hexagonal lattice *Phys. Rev. Lett.* **113** 236802
- [287] Wang Z F, Liu Z and Liu F 2013 Quantum anomalous Hall effect in 2D organic topological insulators *Phys. Rev. Lett.* **110** 196801
- [288] Garrity K F and Vanderbilt D 2013 Chern insulators from heavy atoms on magnetic substrates *Phys. Rev. Lett.* **110** 116802
- [289] Zhang H, Wang J, Xu G, Xu Y and Zhang S C 2014 Topological states in ferromagnetic Cd₂OEuO superlattices and quantum wells *Phys. Rev. Lett.* **112** 096804
- [290] Xu G, Wang J, Felser C, Qi X L and Zhang S C 2015 Quantum anomalous Hall effect in magnetic insulator heterostructure *Nano Lett.* **15** 2019
- [291] Duong L Q, Das T, Feng Y P and Lin H 2015 Quantum anomalous Hall effect and a nontrivial spin-texture in ultra-thin films of magnetic topological insulators *J. Appl. Phys.* **117** 17C741
- [292] Xu G, Weng H, Wang Z, Dai X and Fang Z 2011 Chern semimetal and the quantized anomalous Hall effect in HgCr₂Se₄ *Phys. Rev. Lett.* **107** 186806
- [293] Matsuno J, Ihara K, Yamamura S, Wadati H, Ishii K, Shankar V V, Kee H Y and Takagi H 2015 Engineering spin-orbital magnetic insulator by tailoring superlattices *Phys. Rev. Lett.* **114** 247209
- [294] Yang K Y, Zhu W, Xiao D, Okamoto S, Wang Z and Ran Y 2011 Possible interaction-driven topological phases in (1 1 1) bilayers of LaNiO₃ *Phys. Rev. B* **84** 201104
- [295] Chen Y and Kee H Y 2014 Topological phases in iridium oxide superlattices: quantized anomalous charge or valley Hall insulator *Phys. Rev. B* **90** 195145
- [296] Zhang H, Huang H, Haule K and Vanderbilt D 2014 Quantum anomalous Hall phase in (001) double-perovskite monolayers via intersite spin-orbit coupling *Phys. Rev. B* **90** 165143
- [297] Cai T Y, Li X, Wang F, Sheng J, Feng J, Gong C D 2015 Emergent topological and half semimetallic Dirac fermions at oxide interfaces *Nano Lett.* **15** 6434–9
- [298] Jiang H, Qiao Z, Liu H and Niu Q 2012 Quantum anomalous Hall effect with tunable Chern number in magnetic topological insulator film *Phys. Rev. B* **85** 045445
- [299] Wang J, Lian B, Zhang H, Xu Y and Zhang S C 2013 Quantum anomalous Hall effect with higher plateaus *Phys. Rev. Lett.* **111** 136801
- [300] Tse W K, Qiao Z, Yao Y, MacDonald A H and Niu Q 2011 Quantum anomalous Hall effect in single-layer and bilayer graphene *Phys. Rev. B* **83** 155447
- [301] van Miert G, Smith C M and Jurić V 2014 High-Chern-number bands and tunable Dirac cones in β -graphyne *Phys. Rev. B* **90** 081406
- [302] Zhang Y and Zhang C 2011 Quantized anomalous Hall insulator in a nanopatterned two-dimensional electron gas *Phys. Rev. B* **84** 085123
- [303] Hsu H C, Liu X and Liu C X 2013 Reentrant quantum anomalous Hall effect with in-plane magnetic fields in HgMnTe quantum wells *Phys. Rev. B* **88** 085315
- [304] Liu X, Hsu H C and Liu C X 2013 In-plane magnetization-induced quantum anomalous Hall effect *Phys. Rev. Lett.* **111** 086802
- [305] Pan H, Ren Y, Zeng J, Yang F and Qiao Z 2015 Quantum anomalous Hall effect in low-buckled honeycomb-lattice structures from in-plane magnetization arXiv:1512.05887
- [306] Wright A R 2013 Realising Haldane's vision for a Chern insulator in buckled lattices *Sci. Rep.* **3** 2736
- [307] Martin I and Batista C D 2008 Itinerant electron-driven chiral magnetic ordering and spontaneous quantum Hall effect in triangular lattice models *Phys. Rev. Lett.* **101** 156402
- [308] Hamamoto K, Ezawa M and Nagaosa N 2015 Quantized topological Hall effect in skyrmion crystal *Phys. Rev. B* **92** 115417
- [309] Lado J L and Fernández-Rossier J 2015 Quantum anomalous Hall effect in graphene coupled to skyrmions *Phys. Rev. B* **92** 115433
- [310] Liang Q F, Wu L H and Hu X 2013 Electrically tunable topological state in [1 1 1] perovskite materials with an antiferromagnetic exchange field *New J. Phys.* **15** 063031
- [311] Li H, Sheng L, Shen R, Shao L B, Wang B, Sheng D N and Xing D Y 2013 Stabilization of the quantum spin Hall effect by designed removal of time-reversal symmetry of edge states *Phys. Rev. Lett.* **110** 266802
- [312] Wu J, Liu J and Liu X J 2014 Topological spin texture in a quantum anomalous Hall insulator *Phys. Rev. Lett.* **113** 136403
- [313] Zhang G, Li X, Wu G, Wang J, Culcer D, Kaxiras E and Zhang Z 2014 Quantum phase transitions and topological proximity effects in graphene heterostructure *Nanoscale* **6** 3259
- [314] Morpurgo A F and Guinea F 2006 Inter-valley scattering, long-range disorder and effective time-reversal symmetry breaking in graphene *Phys. Rev. Lett.* **97** 196804
- [315] Xiao D, Liu G B, Feng W, Xu X and Yao W 2012 Coupled spin and valley physics in monolayers of MoS₂ and other group-VI dichalcogenides *Phys. Rev. Lett.* **108** 196802

- [316] Mak K F, McGill K L, Park J and McEuen P L 2014 The valley Hall effect in MoS₂ transistors *Science* **344** 1489
- [317] Ezawa M 2012 Spin-valley optical selection rule and strong circular dichroism in silicene *Phys. Rev. B* **86** 161407
- [318] Rachel S and Ezawa M 2014 Giant magnetoresistance and perfect spin filter in silicene, germanene and stanene *Phys. Rev. B* **89** 195303
- [319] Yao W, Xiao D and Niu Q 2008 Valley-dependent optoelectronics from inversion symmetry breaking *Phys. Rev. B* **77** 235406
- [320] Pesin D and MacDonald A H 2012 Spintronics and pseudospintronic in graphene and topological insulators *Nat. Mater.* **11** 409
- [321] Yazyev O V and Kis A 2015 MoS₂ and semiconductors in the flatland *Mater. Today* **18** 20
- [322] Kuc A and Heine T 2015 The electronic structure calculations of 2D transition-metal dichalcogenides in the presence of external electric and magnetic fields *Chem. Soc. Rev.* **44** 2603
- [323] Liu G B, Xiao D, Yao Y, Xu X and Yao W 2015 Electronic structures and theoretical modelling of two-dimensional group-VIB transition metal dichalcogenides *Chem. Soc. Rev.* **44** 2643
- [324] Butler S Z *et al* 2013 Progress, challenges and opportunities in two-dimensional materials beyond graphene *ACS Nano.* **7** 2898
- [325] Gunlycke D and White C T 2011 Graphene valley filter using a line defect *Phys. Rev. Lett.* **106** 136806
- [326] Gorbatchev R V *et al* 2014 Detecting topological currents in graphene superlattices *Science* **346** 448
- [327] San-Jose P, Prada E, McCann E and Schomerus H 2009 Pseudospin valve in bilayer graphene: towards graphene-based pseudospintronic *Phys. Rev. Lett.* **102** 247204
- [328] Zhu Z, Collaudin A, Fauqué B, Kang W and Behnia K 2011 Field-induced polarization of Dirac valleys in Bismuth *Nat. Phys.* **8** 89
- [329] Isberg J, Gabrysch M, Hammersberg J, Majdi S, Kovi K K and Twitchen D J 2013 Generation, transport and detection of valley-polarized electrons in diamond *Nat. Mater.* **12** 760
- [330] Ezawa M 2014 Valleytronics on the surface of a topological crystalline insulator: elliptic dichroism and valley-selective optical pumping *Phys. Rev. B* **89** 195413
- [331] Giovannetti G, Khomyakov P A, Brocks G, Kelly P J and van den Brink J 2007 Substrate-induced band gap in graphene on hexagonal boron nitride: ab initio density functional calculations *Phys. Rev. B* **76** 073103
- [332] Jung J, DaSilva A M, MacDonald A H and Adam S 2015 Origin of band gaps in graphene on hexagonal boron nitride *Nat. Commun.* **6** 6308
- [333] Zarenia M, Leenaerts O, Partoens B and Peeters F M 2012 Substrate-induced chiral states in graphene *Phys. Rev. B* **86** 085451
- [334] Son Y W, Cohen M L and Louie S G 2006 Half-metallic graphene nanoribbons *Nature* **444** 347
- [335] Qiao Z, Yang S A, Wang B, Yao Y and Niu Q 2011 Spin-polarized and valley helical edge modes in graphene nanoribbons *Phys. Rev. B* **84** 035431
- [336] Zhao B, Zhang J, Wang Y and Yang Z 2014 Quantum valley Hall states and topological transitions in Pt(Ni, Pd)-decorated silicene: a first-principles study *J. Chem. Phys.* **141** 244701
- [337] Zhang D W, Shan C J, Mei F, Yang M, Wang R Q and Zhu S L 2014 Valley-dependent gauge fields for ultracold atoms in square optical superlattices *Phys. Rev. A* **89** 015601
- [338] Guinea F, Katsnelson M I and Geim A K 2010 Energy gaps and a zero-field quantum Hall effect in graphene by strain engineering *Nat. Phys.* **6** 30
- [339] Levy N, Burke S A, Meaker K L, Panlasigui M, Zettl A, Guinea F, Neto A H C and Crommie M F 2010 Strain-induced pseudo-magnetic fields greater than 300 Tesla in graphene nanobubbles *Science* **329** 544
- [340] Gomes K K, Mar W, Ko W, Guinea F and Manoharan H C 2012 Designer Dirac fermions and topological phases in molecular graphene *Nature* **483** 306
- [341] Kruczyński M M, Aleiner I L and Fal'ko V I 2011 Strained bilayer graphene: band structure topology and Landau level spectrum *Phys. Rev. B* **84** 041404
- [342] Yan W, He W Y, Chu Z D, Liu M, Meng L, Dou R F, Zhang Y, Liu Z, Nie J C and He L 2013 Strain and curvature induced evolution of electronic band structures in twisted graphene bilayer *Nat. Commun.* **4** 2159
- [343] Zhang D B, Seifert G and Chang K 2014 Strain-induced pseudomagnetic fields in twisted graphene nanoribbons *Phys. Rev. Lett.* **112** 096805
- [344] Rechtsman M C, Zeuner J M, Tünnermann A, Nolte S, Segev M and Szameit A 2013 Strain-induced pseudomagnetic field and photonic Landau levels in dielectric structures *Nat. Photonics* **7** 153
- [345] Schomerus H and Halpern N Y 2013 Parity anomaly and Landau-level lasing in strained photonic honeycomb lattices *Phys. Rev. Lett.* **110** 013903
- [346] Tian B, Endres M and Pekker D 2015 Landau levels in strained optical lattices *PRL* **115** 236803
- [347] Li S Y, Bai K K, Yin L J, Qiao J B, Wang W X and He L 2015 Observation of Valley-polarized Landau levels in strained graphene *Phys. Rev. B* **92** 245302
- [348] Ezawa M 2013 Spin valleytronics in silicene: quantum spin Hall-quantum anomalous Hall insulators and single-valley semimetals *Phys. Rev. B* **87** 155415
- [349] Martin I, Blanter Y M and Morpurgo A F 2008 Topological confinement in bilayer graphene *Phys. Rev. Lett.* **100** 036804
- [350] Li J, Morpurgo A F, Büttiker M and Martin I 2010 Marginality of bulk-edge correspondence for single-valley Hamiltonians *Phys. Rev. B* **82** 245404
- [351] Li J, Wang K, McFaul K J, Zern Z, Ren Y F, Watanabe K, Taniguchi T, Qiao Z H and Zhu J 2015 Experimental observation of edge states at the line junction of two oppositely biased bilayer graphene (arXiv:1509.03912)
- [352] Ju L *et al* 2014 Topological valley transport at bilayer graphene domain walls *Nature* **520** 650
- [353] Jung J, Zhang F, Qiao Z and MacDonald A H 2011 Valley-Hall kink and edge states in multilayer graphene *Phys. Rev. B* **84** 075418
- [354] Semenoff G W, Semenoff V and Zhou F 2008 Domain walls in gapped graphene *Phys. Rev. Lett.* **101** 087204
- [355] Yao W, Yang S A and Niu Q 2009 Edge states in graphene from gapped flat-band to gapless chiral modes *Phys. Rev. Lett.* **102** 096801
- [356] Wang S K, Wang J and Chan K S 2014 Multiple topological interface states in silicene *New J. Phys.* **16** 045015
- [357] Vaezi A, Liang Y, Ngai D H, Yang L and Kim E A 2013 Topological edge states at a tilt boundary in gated multilayer graphene *Phys. Rev. X* **3** 021018
- [358] Zhang F, MacDonald A H and Mele E J 2013 Valley Chern numbers and boundary modes in gapped bilayer graphene *Proc. Natl Acad. Sci.* **110** 10546
- [359] Kim Y, Choi K, Ihm J and Jin H 2014 Topological domain walls and quantum valley Hall effects in silicene *Phys. Rev. B* **89** 085429
- [360] Alden J S, Tsen A W, Huang P Y, Hovden R, Brown L, Park J, Muller D A and McEuen P L 2013 Strain solitons and topological defects in bilayer graphene *Proc. Natl Acad. Sci.* **110** 11256

- [361] Kindermann M, Uchoa B and Miller D L 2012 Zero-energy modes and gate-tunable gap in graphene on hexagonal boron nitride *Phys. Rev. B* **86** 115415
- [362] Song J, Liu H, Jiang H, Sun Q F and Xie X C 2012 One-dimensional quantum channel in a graphene line defect *Phys. Rev. B* **86** 085437
- [363] Jung J, Qiao Z, Niu Q and MacDonald A H 2012 Transport properties of graphene nanoroads in boron nitride sheets *Nano Lett.* **12** 2936
- [364] Killi M, Wei T C, Affleck I and Paramekanti A 2010 Tunable Luttinger liquid physics in biased bilayer graphene *Phys. Rev. Lett.* **104** 216406
- [365] Li J, Martin I, Büttiker M and Morpurgo A F 2011 Topological origin of subgap conductance in insulating bilayer graphene *Nat. Phys.* **7** 38
- [366] Qiao Z, Jung J, Niu Q and MacDonald A H 2011 Electronic highways in bilayer graphene *Nano Lett.* **11** 3453
- [367] Qiao Z, Jung J, Lin C, Ren Y, MacDonald A H and Niu Q 2014 Current partition at topological channel intersections *Phys. Rev. Lett.* **112** 206601
- [368] Liu Z, Wang Z F, Mei J W, Wu Y S and Liu F 2013 Flat Chern band in a two-dimensional organometallic framework *Phys. Rev. Lett.* **110** 106804
- [369] Fu L and Kane C L 2009 Josephson current and noise at a superconductor/quantum-spin-Hall-insulator/superconductor junction *Phys. Rev. B* **79** 161408
- [370] Alicea J 2012 New directions in the pursuit of Majorana fermions in solid state systems *Rep. Prog. Phys.* **75** 076501
- [371] Kitaev A Y 2003 Fault-tolerant quantum computation by anyons *Ann. Phys.* **303** 2
- [372] Nayak C, Simon S H, Stern A, Freedman M and Das Sarma S 2008 Non-abelian anyons and topological quantum computation *Rev. Mod. Phys.* **80** 1083
- [373] Beckmann D, Weber H B and Löhneysen H V 2004 Evidence for crossed Andreev reflection in superconductor-ferromagnet hybrid structures *Phys. Rev. Lett.* **93** 197003
- [374] Russo S, Kroug M, Klapwijk T M and Morpurgo A F 2005 Experimental observation of bias-dependent nonlocal Andreev reflection *Phys. Rev. Lett.* **95** 027002
- [375] Nielsen M A and Chuang I L 2000 *Quantum Computation and Quantum Information* (Cambridge: Cambridge University Press)
- [376] Chtchelkatchev N M, Blatter G, Lesovik G B and Martin T 2002 Bell inequalities and entanglement in solid-state devices *Phys. Rev. B* **66** 161320
- [377] Kou X, Fan Y, Lang M, Upadhyaya P and Wang K L 2015 Magnetic topological insulators and quantum anomalous Hall effect *Solid State Commun.* **215–6** 34
- [378] Wang J, Lian B and Zhang S C 2015 Quantum anomalous Hall effect in magnetic topological insulators *Phys. Scr.* **2015** 014003
- [379] Liu C-X, Zhang S-C and Qi X-L 2015 The quantum anomalous Hall effect (arXiv:[1508.07106v1](https://arxiv.org/abs/1508.07106v1))
- [380] Weng H, Yu R, Hu X, Dai X and Fang Z 2015 Quantum anomalous Hall effect and related topological electronic states *Adv. Phys.* **64** 227–82